Diss. ETH No. 25979

Full Waveform Ambient Noise Inversion

A thesis submitted to attain the degree of

Doctor of Sciences of ETH Zurich
[Dr. sc. ETH Zurich]

presented by

Korbinian Sager

MSc. ETH Zurich
born on 22.07.1988
citizen of Germany

accepted on the recommendation of

Prof. Dr. Andreas Fichtner
Dr. Christian Boehm
Prof. Dr. Victor Tsai

2019

Make some noise!
– H.P. Baxxter

Abstract

This thesis deals with the development and application of a novel method for seismic interferometry, referred to as full waveform ambient noise inversion. It incorporates the heterogeneous nature of ambient noise sources in space and frequency, and models the full wave propagation physics. By dropping the principle of Green's function retrieval, the basis of traditional ambient noise tomography, we establish correlation functions as self-consistent observables. A more accurate description of the physics of the problem allows us to extract additional information, to advance our understanding of correlation wavefields and to quantify inherent source-structure trade-offs.

We generalize the theoretical formulation, thus facilitating the application of adjoint techniques, and investigate the prerequisites for its application to real data in a synthetic 2-D study. We then follow with a framework for modeling correlations in 3-D attenuating media with arbitrary noise source distributions and for the computation of sensitivity kernels for changes in source and structure. In a pilot use case, we look into a commonly encountered difference between the observation of body waves and surface waves, and reveal fundamentally different conditions for their reconstruction. For a final synthesis of all results and a proof of concept we invert a global dataset focusing on the long-period ambient noise field, called the Earth's Hum, for the distribution of ambient noise sources, and for Earth structure. We confirm existing models for the source power-spectral density and recover tomographic features well known from global Earth models.

Zusammenfassung

Diese Arbeit befasst sich mit der Entwicklung und Anwendung einer neuartigen Methode für seismische Interferometrie, die als *full waveform ambient noise inversion* bezeichnet wird. Der Ansatz berücksichtig die Raum- und Frequenzabhängigkeit der Quellverteilungen des seismischen Rauschens und durch numerische Simulationen auch die Physik der Wellenausbreitung. Indem wir mit dem Prinzip für die Ermittlung einer Greenschen Funktion die Grundlage bisheriger Tomographien, die auf seismischem Rauschen basieren, fallen lassen, etablieren wir Kreuzkorrelationen als selbstkonsistente Observablen. Mit einer präziseren Beschreibung der Physik des Problems können wir zusätzliche Informationen extrahieren, Korrelationswellenfelder besser verstehen und das unvermeidbare Wechselspiel zwischen Quelle und Struktur quantifizieren.

Zu Beginn stellen wir eine Verallgemeinerung der zugrundeliegenden Theorie vor, wodurch der Einsatz von adjungierten Methoden vereinfacht wird. Darauf aufbauend untersuchen wir in einer synthetischen Studie in 2-D die Voraussetzungen für die Anwendung mit echten Daten. Das Konzept für die Modellierung von Kreuzkorrelationen in 3-D unter Berücksichtigung von Dämpfung, sowie für die Berechnung von Sensitivitäten bezüglich Änderungen von Quelle und Struktur wird im Anschluss präsentiert und umgesetzt. In einem ersten Anwendungsfall untersuchen wir Unterschiede, die typischerweise in der Beobachtung von Raum- und Oberflächenwellen auftreten, und legen fundamental unterschiedliche Bedingungen für deren Rekonstruktion offen. Für eine abschliessende Synthese aller Ergebnisse führen wir eine Machtbarkeitsstudie durch und invertieren einen globalen Datensatz, der sich auf das langperiodische seismische Rauschen, auch als *Earth's Hum* bekannt, bezieht, nach der räumlichen Verteilung der Quellstärke und nach Erdstruktur. Damit bestätigen wir existierende Modelle für die Quellverteilung und tomographische Strukturen treten hervor, die von globalen Geschwindigkeitsmodellen bekannt sind.

Contents

List of Figures

Introduction 1

The ambient noise field was long regarded as "not of great seismological interest in itself" (*Agnew and Berger*, 1978), but has in recent years attracted considerable attention as a valuable source of information on 3-D Earth structure. This paradigm shift was possible due to the rising awareness in seismology that the system response can be extracted from noise recordings. As pointed out by *Snieder and Larose* (2013), the underlying principle actually dates back more than a century to the paper by *Einstein* (1906) on Brownian motion. Although *Aki* (1957) and *Claerbout* (1968) used similar approaches to study surface waves propagating in the near surface or to relate the reflection response to the transmission response, this field of research only gained momentum after the work by *Lobkis and Weaver* (2001), who derived and demonstrated in a laboratory experiment that the inter-station correlation of recordings of a diffuse field with random and uncorrelated modes is proportional to the Green's function[1] between the respective receivers.

Campillo and Paul (2003) applied the principle of Green's function retrieval first to earthquake coda and extracted the Green's tensor for surface waves. Follow-up studies then confirmed the emergence of surface waveforms from correlations of microseismic noise (*Shapiro and Campillo*, 2004; *Sabra et al.*, 2005a) and prompted a large number of regional and also global tomographic studies (*Shapiro et al.*, 2005; *Sabra et al.*, 2005b; *Nishida et al.*, 2009). While seismic tomography based on ambient noise flourished, theoretical derivations established that the equality of the inter-station correlation and the Green's function only holds under specific conditions, including wavefield diffusivity and equipartitioning (*Lobkis and Weaver*, 2001; *Sánchez-Sesma and Campillo*, 2006; *Weaver and Lobkis*, 2004; *Snieder et al.*, 2007; *Tsai*, 2009) or, equivalently, the isotropic distribution of both mono- and dipolar uncorrelated noise sources (*Wapenaar*, 2004; *Wapenaar and Fokkema*, 2006; *Snieder*, 2007). Despite the strong empirical evidence that at least fundamental-mode surface waves can be extracted and although tomographic images are broadly consistent with models based on earthquake data (*Stehly et al.*, 2009; *Nishida et al.*, 2009; *Haned et al.*, 2016; *Castellanos et al.*, 2018), the specific nature of the assumptions necessary for Green's function retrieval required research on the characteristics of the ambient noise field and on potential consequences and limitations for ambient noise tomography.

[1] Deciding between "Green function" and "Green's function" we follow the recommendation by *Wright* (2006). Although the use of "Green's function" together with a definite article is slightly inconsistent, it does not suggest the existence of one universal entity in the following.

1. Introduction

The ambient seismic noise field is excited by a heterogeneous and non-stationary distribution of noise sources. Commonly, three peaks are observed in the power spectrum at most seismic stations (*Pederson*, 1993). They are referred to as the Earth's Hum (∼2 to 15 mHz), the primary microseism (∼0.05 to 0.1 Hz) and the secondary microseism (∼0.1 to 1 Hz). The primary and secondary microseisms likely originate from the interaction of ocean waves with the bathymetry and from the non-linear interaction of ocean waves traveling in opposite directions, respectively (*Longuet-Higgins*, 1950; *Hasselmann*, 1963; *Ardhuin et al.*, 2015). The excitation mechanism of the Earth's Hum has been the subject of considerable debate. While some authors argue for atmospheric pressure fluctuations (*Nishida and Kobayashi*, 1999; *Tanimoto and Um*, 1999; *Nishida*, 2014), other studies indicate interactions between the atmosphere, the oceans and the solid Earth (*Rhie and Romanowicz*, 2004; *Webb*, 2007; *Bromirski and Gerstoft*, 2009). Latest research favors its generation in the ocean by infragravity waves propagating over a sloping ocean floor close to the coast (*Ardhuin et al.*, 2015; *Deen et al.*, 2018). Noise above 1 Hz is considered to be dominated by anthropogenic activities and local meteorological conditions (e.g. *Díaz*, 2016). Irrespective of the excitation type, the magnitude of ambient noise sources varies considerably in space and depends on the ocean state, atmospheric conditions, etc. which may vary over short timescales.

The discrepancy between the assumptions invoked for the principle of Green's function retrieval and the nature of the ambient noise sources has various consequences. Amplitudes of noise correlation functions are difficult to interpret and complicate attenuation studies (*Prieto et al.*, 2011; *Tsai*, 2011; *Harmon et al.*, 2010; *Stehly and Boué*, 2017). Heterogeneous noise source distributions affect traveltime measurements (*Tsai*, 2009; *Weaver et al.*, 2009; *Yao and van der Hilst*, 2009; *Harmon et al.*, 2010; *Froment et al.*, 2010; *Delaney et al.*, 2017; *Sadeghisorkhani et al.*, 2017) and introduce spurious arrivals, which can be mistaken as reliable information (*Snieder et al.*, 2006). In addition, certain seismic phases such as body waves and higher-mode surfaces waves are not excited correctly in correlation functions (*Halliday and Curtis*, 2008; *Kimman and Trampert*, 2010), which leads to a poor depth resolution in tomographic images.

Besides correction factors presented in some of the studies above, numerous processing and stacking schemes have been proposed to mitigate the difference between reality and the assumptions necessary for Green's function retrieval (*Bensen et al.*, 2007; *Groos et al.*, 2012). A common approach is to select correlation functions that resemble plausible Green's functions and to discard the rest, which may affect up to 70 percent of a data set (*Stehly et al.*, 2009). Correlation functions that are strongly altered by heterogeneous noise source distributions may therefore be excluded although they contain valuable information on 3-D Earth structure (*Landès et al.*, 2010). For example, strong noise sources perpendicular to

the line connecting two stations manifest themselves in wave packets around zero lag, which cannot be interpreted reasonably as a feature of a Green's function. Other processing steps vary for each data set and are usually guided by the objective of the respective study. The specific choices change the actual waveforms in correlation functions, which unavoidably changes the sensitivity to noise sources and Earth structure, and processed correlation functions do not necessarily fulfill the wave equation (*Fichtner*, 2014; *Fichtner et al.*, 2017). Further approaches trying to reduce the imprint of the ambient noise field include deconvolution (*Snieder and Şafak*, 2006; *Vasconcelos and Snieder*, 2008a,b), multi-dimensional deconvolution (*Wapenaar et al.*, 2008; *Wapenaar and van der Neut*, 2010; *van der Neut et al.*, 2011; *Wapenaar et al.*, 2011a,b), higher-order correlations (*Stehly et al.*, 2008; *Spica et al.*, 2016; *Sheng et al.*, 2018) and wavefront tracking (*Lin et al.*, 2012; *Bowden et al.*, 2015, 2017). For large and dense networks *de Ridder and Maddison* (2018) even skip the extraction of response functions and extract medium parameters by reconstructing the actual ambient noise field. They all, however, only work under specific circumstances and require a certain receiver geometry or density.

During the last decade, great progress has been made in ambient noise tomography based on the principle of Green's function retrieval. The discussed shortcomings and the multitude of ways to circumvent them, however, reflect that this principle cannot usually be readily invoked and ambient noise tomography reaches a limit. Modern tomographic methods exploiting details in waveforms for the benefit of improved resolution (*Pratt*, 1999; *Chen et al.*, 2007a; *Tape et al.*, 2009; *Fichtner et al.*, 2009) cannot be applied directly, since Green's function retrieval does not account for the influence of the distribution of noise sources on the actual waveforms in correlation functions.

In order to address these limitations, we develop and apply a method - in the following referred to as full waveform ambient noise inversion - that is capable of accounting for the distribution of noise sources in space and frequency, 3-D heterogeneous Earth structure and the full seismic wave propagation physics. The fundamental idea is to drop the principle of Green's function retrieval, to extract information directly from correlation functions and to establish them as self-consistent observables in seismology.
A similar approach is used in helioseismology to study solar structure and dynamics (*Woodard*, 1997; *Gizon and Birch*, 2002; *Hanasoge et al.*, 2011) and has recently been applied to terrestrial seismology (*Tromp et al.*, 2010; *Hanasoge*, 2013; *Basini et al.*, 2013; *Hanasoge*, 2014; *Fichtner*, 2014; *Ermert et al.*, 2017). In contrast to the previous studies, we generalize and extend the underlying theory, and the forward modeling study, as well as the synthetic inversion in 2-D are more comprehensive. In addition, the developed framework for 3-D media with arbitrary distributions of the ambient noise sources allows us to perform an inversion of observed data for the first time for both sources and structure.

Outline

In chapters 2 and 3 we lay the foundation of full waveform ambient noise inversion. We introduce the theory and generalize its formulation, which facilitates the application of adjoint techniques. We derive expressions for the efficient evaluation of first and second derivatives. In a synthetic study in 2-D we train our physical intuition, explore the potential of our approach and investigate the requirements necessary for the application to observed data. Both chapters as well as the introduction are adapted[2] from:

> *Sager, K., L. Ermert, C. Boehm, and A. Fichtner* (**2018**a),
> **Towards full waveform ambient noise inversion,**
> Geophysical Journal International, *212*(1), 566–590,
> doi: 10.1093/gji/ggx429.

In chapter 4 we implement a framework for the computation of correlations in 3-D media with arbitrary distributions of the source power-spectral density. It was written in collaboration with *Christian Boehm, Lion Krischer, Michael Afanasiev and Andreas Fichtner*. The new implementation opens the door for many studies that were previously impossible or tedious to conduct. By studying the sensitivity of correlations to local and global noise source in chapter 5, we advance our understanding of the generation of signals in correlation functions. We do not only confirm the robustness of ambient noise tomography based on surface waves, but provide insight into the commonly experienced difficulty to observe body waves. Except for section 5.6, this chapter is published in:[2]

> *Sager, K., C. Boehm, L. Ermert, L. Krischer, and A. Fichtner* (**2018**b),
> **Sensitivity of seismic noise correlation functions to global noise sources,**
> Journal of Geophysical Research: Solid Earth, *123*(8), 6911–6921,
> doi: 10.1029/2018JB016042.

In chapter 6 we provide a proof of concept for the developments presented above and invert a global dataset focusing on the Earth's Hum for the distribution of the ambient noise sources and for Earth structure. It was written in collaboration with *Christian Boehm, Laura Ermert, Lion Krischer and Andreas Fichtner*. A corresponding publication is currently in preparation.

A summary of ideas for future research is given in chapter 7. Section 7.7 on monitoring with full waveform ambient noise inversion is part of a proposal funded by the Swiss National Science Foundation in the framework of an Early PostDoc.Mobility fellowship.

[2] Major changes compared to the original publication are indicated with footnotes.

This research was supported by the Swiss National Science Foundation (SNSF) under grant 200021_149143 and by the Swiss National Supercomputing Center (CSCS) in the form of the GeoScale and ch1/s741/s868 projects. We acknowledge support from and discussions within TIDES COST Action ES1401.

Forward and Inverse Theory 2

2.1 Forward theory

To forward model inter-station correlations of ambient noise, we adopt the method developed by *Woodard* (1997) in helioseismology and recently transported to terrestrial seismology by *Tromp et al.* (2010).
We start with the definition of the frequency-domain Green's function $G_{i,n}(\mathbf{x}, \boldsymbol{\xi})$ as the solution of the governing equations when the right-hand side equals a point-localized force at position $\boldsymbol{\xi}$ in n-direction, i.e.

$$\mathcal{L}[\, G_{i,n}(\mathbf{x}, \boldsymbol{\xi})\,] = \delta_{in}\delta(\mathbf{x} - \boldsymbol{\xi}), \tag{2.1}$$

with the Kronecker delta δ_{in} and the forward modeling operator $\mathcal{L}$. In the interest of a condensed notation, dependencies are omitted wherever possible, i.e. here on the angular frequency ω. The operator notation allows us to develop a general theory independent of the specific choice of the forward problem. In seismology, for example, it could stand for any type of wave equation. We limit ourselves, however, to operators that are linear in their argument. The operator contains all model parameters $\mathbf{m}$, in our case the material parameters, that determine the response of the physical system to an external force given by the right-hand side in equation (2.1).
The i-component of the seismic displacement field $u_i(\mathbf{x})$ is connected with the Green's function $G_{i,n}(\mathbf{x}, \boldsymbol{\xi})$ and the forcing term $N_n(\boldsymbol{\xi})$, in our case the source field of ambient noise, via an integral over the volume $\oplus$ of the Earth, i.e.

$$u_i(\mathbf{x}) = \int\limits_{\oplus} G_{i,n}(\mathbf{x}, \boldsymbol{\xi}) N_n(\boldsymbol{\xi})\, d\boldsymbol{\xi}, \tag{2.2}$$

which is also known as representation theorem (*Aki and Richards*, 2002). Einstein's summation convention applies to repeated lower-case subscripts. The cross-correlation of the noise fields $u_i(\mathbf{x}_1)$ and $u_j(\mathbf{x}_0)$ is in the frequency domain given by

$$\begin{aligned} \mathcal{C}_{ij}(\mathbf{x}_1, \mathbf{x}_0) &= u_i(\mathbf{x}_1) u_j^*(\mathbf{x}_0) \\ &= \iint\limits_{\oplus\,\oplus} G_{i,n}(\mathbf{x}_1, \boldsymbol{\xi}_1) N_n(\boldsymbol{\xi}_1) G^*_{j,m}(\mathbf{x}_0, \boldsymbol{\xi}_2) N^*_m(\boldsymbol{\xi}_2)\, d\boldsymbol{\xi}_1\, d\boldsymbol{\xi}_2. \end{aligned} \tag{2.3}$$

We then consider the average $\overline{\mathcal{C}_{ij}(\mathbf{x}_1, \mathbf{x}_0)}$ over many realizations

$$\begin{aligned} C_{ij}(\mathbf{x}_1, \mathbf{x}_0) &= \overline{\mathcal{C}_{ij}(\mathbf{x}_1, \mathbf{x}_0)} \\ &= \iint\limits_{\oplus\oplus} G_{i,n}(\mathbf{x}_1, \boldsymbol{\xi}_1) G^*_{j,m}(\mathbf{x}_0, \boldsymbol{\xi}_2)\ \overline{N_n(\boldsymbol{\xi}_1) N^*_m(\boldsymbol{\xi}_2)}\ d\boldsymbol{\xi}_1\, d\boldsymbol{\xi}_2, \end{aligned} \tag{2.4}$$

which is estimated in standard processing of inter-station correlation functions by stacking over many time intervals (*Bensen et al.*, 2007). As pointed out by *Snieder et al.* (2010) dissipation effectively resets the clock after a characteristic decay time so that consecutive wavefield samples are practically independent. The evaluation of equation (2.4) is prohibitively expensive, not only because of the double integral, but also since many realizations of the noise sources are required. This has only been done for simplified wave propagation scenarios (*Cupillard and Capdeville*, 2010; *van Driel et al.*, 2015; *Fichtner et al.*, 2017). To reduce computational costs, we assume that the correlation between different noise sources decays relatively quickly with distance compared to the seismic wavelength and that the contribution from collocated noise sources to the correlation function is dominant. We therefore approximate $\overline{N_n(\boldsymbol{\xi}_1) N^*_m(\boldsymbol{\xi}_2)}$ with a delta function in space, i.e.

$$\overline{N_n(\boldsymbol{\xi}_1) N^*_m(\boldsymbol{\xi}_2)} = S_{nm}(\boldsymbol{\xi}_1) \delta(\boldsymbol{\xi}_1 - \boldsymbol{\xi}_2), \tag{2.5}$$

with the power-spectral density $S_{nm}(\boldsymbol{\xi})$. This assumption is frequently made (*Woodard*, 1997; *Tromp et al.*, 2010; *Hanasoge*, 2013, 2014; *Nishida*, 2014; *Fichtner*, 2014) and its quality has to be assessed for each data set. With a finite correlation length in space, the forward theory will remain computable, since the double integral has to be evaluated only for a small region in space. A detailed discussion can be found in section 2.3. For uncorrelated noise sources equation (2.3) condenses to

$$C_{ij}(\mathbf{x}_1, \mathbf{x}_0) = \int\limits_{\oplus} G_{i,n}(\mathbf{x}_1, \boldsymbol{\xi}) G^*_{j,m}(\mathbf{x}_0, \boldsymbol{\xi}) S_{nm}(\boldsymbol{\xi})\, d\boldsymbol{\xi}. \tag{2.6}$$

Comparing (2.6) to the representation theorem (2.2) we see that $C_{ij}(\mathbf{x}_1, \mathbf{x}_0)$ can be interpreted as the i-component of a correlation wavefield $\mathbf{C}_j(\mathbf{x}, \mathbf{x}_0)$

$$C_{ij}(\mathbf{x}, \mathbf{x}_0) = \int\limits_{\oplus} G_{i,n}(\mathbf{x}, \boldsymbol{\xi}) \left[G^*_{j,m}(\mathbf{x}_0, \boldsymbol{\xi}) S_{nm}(\boldsymbol{\xi}) \right] d\boldsymbol{\xi}, \tag{2.7}$$

evaluated at position $\mathbf{x} = \mathbf{x}_1$. Its numerical computation can be described with the following recipe:

step 1: Using source-receiver reciprocity, compute the Green's function $G_{m,j}(\boldsymbol{\xi}, \mathbf{x}_0)$ with source at $\mathbf{x}_0$.

step 2: Multiply its complex conjugate with the noise source power-spectral density $S_{nm}(\boldsymbol{\xi})$.

step 3: Model the correlation wavefield as a solution of the wave equation with $G^*_{m,j}(\boldsymbol{\xi}, \mathbf{x}_0) S_{nm}(\boldsymbol{\xi})$ as a distributed source and sample the correlation wavefield at any position where another receiver is located.

We now have a forward model for the computation of inter-station correlation functions for arbitrary distributions of the power-spectral density in frequency and space. It is important to note that this approach does not require any assumptions on wavefield diffusivity and equipartitioning (*Lobkis and Weaver*, 2001; *Weaver and Lobkis*, 2004; *Sánchez-Sesma and Campillo*, 2006) or the isotropic distribution of both mono- and dipolar uncorrelated noise sources (*Wapenaar*, 2004; *Wapenaar and Fokkema*, 2006; *Snieder*, 2007) that would be necessary to equate correlations with Green's functions.

2.1.1 General formulation of the forward theory

To facilitate further developments regarding sensitivity kernels and Hessian-vector products and, in addition, to be independent of the choice of time or frequency domain, we propose the following two PDEs for a general formulation describing the modeling of inter-station correlation functions according to the recipe above:

$$\underbrace{\mathcal{L}[\, G_{m,j}(\mathbf{x}, \mathbf{x}_0)\,] = \delta_{mj}\, D(\, 0, \mathbf{x}_0\,)}_{\textbf{step 1}} \tag{2.8}$$

$$\underbrace{\mathcal{L}[\, C_{ij}(\mathbf{x}, \mathbf{x}_0)\,] = \underbrace{\delta_{in}\, P[\, S_{nm}(\mathbf{x}), G_{m,j}(\mathbf{x}, \mathbf{x}_0)\,]}_{\textbf{step 2}},}_{\textbf{step 3}} \tag{2.9}$$

where $D(\, t_s, \mathbf{x}_s)$ represents two delta functions, one at time t_s or the respective frequency domain equivalent and the other in space at $\mathbf{x}_s$. The term P denotes a bilinear function acting on $S_{nm}(\mathbf{x})$ and $G_{m,j}(\mathbf{x}, \mathbf{x}_0)$. In the frequency domain P can simply be a multiplication of $S_{nm}(\mathbf{x}, \omega)$ and $G^*_{m,j}(\mathbf{x}, \mathbf{x}_0, \omega)$, thereby again invoking Einstein's summation convention. This would translate to a correlation between $G_{m,j}(\mathbf{x}, \mathbf{x}_0, t)$ and the time domain equivalent $S_{nm}(\mathbf{x}, t)$ of the power-spectral density, and summing over m. These are only examples and other definitions are possible (see next subsection).

2.1.2 Example for membrane waves

After each paragraph covering theoretical developments, we apply the main findings to membrane waves (*Tanimoto*, 1990; *Peter et al.*, 2007; *Tape et al.*, 2007) to give a better understanding of the concepts. Since they can be interpreted as an analogue to fundamental mode surface waves, we also refer to them as surface waves in the following. The operator $\mathcal{L}$ describing membrane waves traveling in the $x-y$ plane with vertical displacement u is in the time domain given by

$$\mathcal{L}(\circ) = \rho\,\partial_{tt}\circ - \partial_{\mathbf{x}}\big[\mu\,\partial_{\mathbf{x}}\circ\big], \tag{2.10}$$

with density ρ, shear modulus μ and the (second) partial derivatives with respective to space $\partial_{\mathbf{x}}$ and time ∂_{tt}. The symbol $\circ$ represents a place holder, in this case for a scalar wavefield. Equations (2.8) and (2.9) take the specific form

$$\rho\,\partial_{tt}G(\mathbf{x},\mathbf{x}_0,t) - \partial_{\mathbf{x}}\big[\mu\,\partial_{\mathbf{x}}G(\mathbf{x},\mathbf{x}_0,t)\big] = \delta(t)\delta(\mathbf{x}-\mathbf{x}_0), \tag{2.11}$$

$$\begin{aligned}\rho\,\partial_{tt}C(\mathbf{x},\mathbf{x}_0,t) &- \partial_{\mathbf{x}}\big[\mu\,\partial_{\mathbf{x}}C(\mathbf{x},\mathbf{x}_0,t)\big] \\ &= \underbrace{\frac{1}{2\pi}\,\mathrm{Re}\int_{-\infty}^{\infty} S(\mathbf{x},\omega)\Big[\int_{\tau} G(\mathbf{x},\mathbf{x}_0,t)\,e^{-i\omega t}\,dt\Big]^{*} e^{i\omega t}\,d\omega}_{=:\,P[\,S(\mathbf{x}),\,G(\mathbf{x},\mathbf{x}_0)\,]}\,.\end{aligned} \tag{2.12}$$

The innermost integral on the right-hand side of equation (2.12), bracketed with [.], is an approximation of the Fourier transform of the Green's function for a finite time interval $\tau = [t_1, t_2]$. The interval is chosen such that $(t_2 - t_1)^{-1}$ is much smaller than the minimum frequency of interest in order to avoid contamination of the Fourier spectrum. The complex conjugate of the Fourier transformed Green's function, equivalent to its time reversed version, is multiplied with the power-spectral density $S(\mathbf{x},\omega)$ and the product is transformed back to the time domain. The final forcing term of the correlation wavefield is a time-dependent quantity that is distributed in space.
In a realistic inverse problem, however, a continuous and infinite-dimensional frequency dependence cannot be resolved. We therefore choose a parametrization of the power-spectral density in terms of L basis functions $S_l(\mathbf{x})$ that are constant within a period band given by ω_l and ω_{l+1} and zero outside. The integral over frequency is thus split up in a sum of L integrals, each covering the frequency band of the respective basis function. Equation

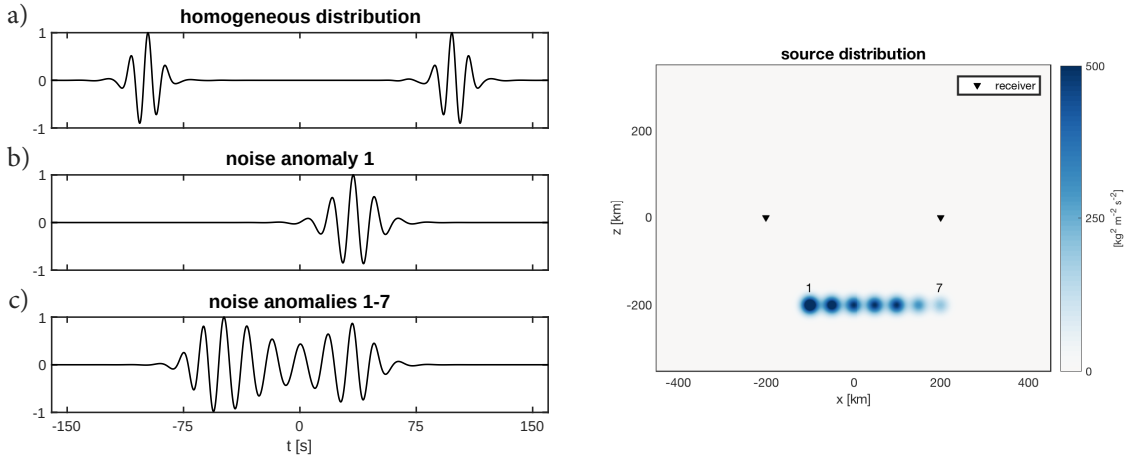

Figure 2.1: Correlation functions for different noise source distributions computed for a frequency band of $0.05 - 0.18$ Hz and a homogeneous velocity model with $v = 4000$ km/s. The noise source distributions for b) and c) are shown on the right. Each correlation function is normalized.

(2.12) changes accordingly to

$$\rho\,\partial_{tt}C(\mathbf{x},\mathbf{x}_0,t) - \partial_{\mathbf{x}}\left[\mu\,\partial_{\mathbf{x}}C(\mathbf{x},\mathbf{x}_0,t)\right] = \underbrace{\frac{1}{2\pi}\,\mathrm{Re}\sum_l S_l(\mathbf{x}) \int_{w_l}^{w_{l+1}} \Big[\int_\tau G(\mathbf{x},\mathbf{x}_0,t)\,e^{-i\omega t}\,dt\Big]^* e^{i\omega t}\,d\omega}_{=:\,P[\,S(\mathbf{x}),G(\mathbf{x},\mathbf{x}_0)\,]}\,. \tag{2.13}$$

This represents only one possibility to adapt $P[\,S(\mathbf{x}),\,G(\mathbf{x},\mathbf{x}_0)\,]$ for inversions and other definitions might be more feasible, but for clarity we base the following examples on equation (2.13). Correlation functions for one frequency band are shown in figure 2.1 for different distributions in space. The two heterogeneous noise source distributions lead to asymmetric correlation functions with waves arriving earlier than the surface wave, which cannot be interpreted reasonably by Green's function retrieval.

2.2 The continuous adjoint method for first and second derivatives

2.2.1 First derivatives

The objective of full waveform ambient noise inversion is to find material parameters $\mathbf{m}$ and a power-spectral density distribution S_{nm}, which minimizes a misfit $\mathcal{X}$ used to quantify the deviation of synthetic correlation functions and their corresponding observations. Since $\mathcal{X}$ is generally a non-linear function of $\mathbf{m}$ and S_{nm}, we approximate the optimum with the help of iterative minimization algorithms. In order to obtain an efficient formulation to compute directional derivatives of $\mathcal{X}$ with respect to the power-spectral density and Earth structure, we apply the continuous adjoint method in the following (*Tarantola*, 1988; *Tromp et al.*, 2005; *Fichtner et al.*, 2006) to the PDEs (2.8) and (2.9) describing the modeling of correlation functions. For the sake of a clean notation we present the derivation only for scalar wavefields. The extension to elastic media follows the same steps.

2.2.1.1 Source kernel

The choice of the misfit functional depends on the specific problem and influences to a large extent the results of an inversion. Since the formalism described in the following, however, can be applied to any differentiable misfit functional, we write the misfit in a generic form by two integrals, which we denote by $\langle . \rangle$. One integral is over space $\mathbf{x} \in \oplus \subset \mathbb{R}^3$ and the other over time $t \in \tau = [t_1, t_2]$ or equivalently over angular frequency $\omega \in W = [\omega_1, \omega_2]$ (*Fichtner*, 2010). We therefore write

$$\mathcal{X}(\mathbf{m}, S) = \Big\langle \chi(C(\mathbf{m}, S)) \Big\rangle, \tag{2.14}$$

where χ is a space and time dependent evaluation of the discrepancy between synthetics and observations. For observations at specific locations, e.g. at seismic stations, χ can be defined by introducing δ functions in space. Without loss of generality, we consider a time interval τ well suited for correlation functions, which is centered around time zero, i.e. $\tau = [-t_c, t_c]$, where t_c is the maximum lag of the correlation function. An improvement of the fit translates to a decrease of the misfit functional $\mathcal{X}$. In order to invert for the distribution of noise sources in space, we are therefore interested in the directional derivative of $\mathcal{X}$ with respect to S. Applying the chain rule we get

$$\nabla_S \mathcal{X}\, \delta S = \nabla_C \mathcal{X}\, \delta_S C = \Big\langle \nabla_C \chi\, \delta_S C \Big\rangle, \tag{2.15}$$

where

$$\delta_S C = \nabla_S C\, \delta S \tag{2.16}$$

represents the first-order change of the correlation C for a variation in the source distribution δS. The difficulty of equation (2.15) lies in the appearance of $\delta_S C$ that is computationally expensive to evaluate for all possible directions δS necessary for a complete evaluation of the directional derivative. A first-order finite-difference approximation of $\nabla_S \mathcal{X}$ would mean to evaluate $C(\mathbf{m}, S + \delta S)$ for all possible directions δS, which becomes infeasible for expensive forward calculations or large model domains. Thus, the following considerations are directed to eliminate $\delta_S C$ in equation (2.15). To achieve this, we differentiate equation (2.9) with respect to S, which gives

$$\mathcal{L}(\delta_S C) - P(\,\delta S, G\,) = 0, \tag{2.17}$$

where we use that $\mathcal{L}$ is linear in C and P linear in S, i.e.

$$\nabla_C \mathcal{L}(C)\,\delta_S C = \mathcal{L}(\delta_S C), \tag{2.18}$$

$$\nabla_S\, P(\,S, G\,)\,\delta S = P(\,\delta S, G\,). \tag{2.19}$$

Multiplying equation (2.17) by an arbitrary test function $u^\dagger$, applying the integrals $\langle . \rangle$ and adding it to equation (2.15) yields

$$\nabla_S \mathcal{X}\,\delta S = \Big\langle \nabla_C \chi\,\delta_S C + u^\dagger\,\mathcal{L}(\delta_S C) - u^\dagger\,P(\,\delta S, G\,) \Big\rangle. \tag{2.20}$$

Invoking the adjoint variable defined by

$$\Big\langle \nabla_C \chi\,\delta_S C \Big\rangle = \Big\langle \delta_S C\,\nabla_C \chi^\dagger \Big\rangle, \tag{2.21}$$

as well as the adjoint operator

$$\Big\langle u^\dagger\,\mathcal{L}(\delta_S C) \Big\rangle = \Big\langle \delta_S C\,\mathcal{L}^\dagger(u^\dagger) \Big\rangle \tag{2.22}$$

for any $u^\dagger$ and $\delta_S C$, we obtain

$$\begin{aligned} \nabla_S \mathcal{X}\,\delta S &= \Big\langle \delta_S C\,\nabla_C \chi^\dagger + \delta_S C\,\mathcal{L}^\dagger(u^\dagger) - u^\dagger\,P(\,\delta S, G\,) \Big\rangle \\ &= \Big\langle \delta_S C\,[\,\nabla_C \chi^\dagger + \mathcal{L}^\dagger(u^\dagger)\,] - u^\dagger\,P(\,\delta S, G\,) \Big\rangle. \end{aligned} \tag{2.23}$$

We can now eliminate $\delta_S C$ when a field $u^\dagger$ can be found such that the adjoint equation

$$\mathcal{L}^\dagger(u^\dagger) = -\nabla_C \chi^\dagger \tag{2.24}$$

is satisfied. The right-hand side of equation (2.24) is usually referred to as adjoint source time function and we denote it by f in the example sections below. The directional

derivative of $\mathcal{X}$ in equation (2.15) then simplifies to

$$\nabla_S \mathcal{X}\, \delta S = -\Big\langle u^\dagger\, P(\, \delta S, G\,) \Big\rangle. \tag{2.25}$$

Choosing the frequency domain for illustration, equation (2.25) can be written as

$$\begin{aligned} \nabla_S \mathcal{X}\, \delta S(\mathbf{x},\omega) &= -\int\limits_{\oplus}\int\limits_{W} u^\dagger(\mathbf{x},\omega)\, P\big[\, \delta S(\mathbf{x},\omega), G(\mathbf{x},\mathbf{x}_0,\omega)\,\big]\, d\mathbf{x}\, d\omega \\ &= \int\limits_{\oplus}\int\limits_{W} K(x,\omega)\, \delta S(\mathbf{x},\omega)\, d\mathbf{x}\, d\omega, \end{aligned} \tag{2.26}$$

where we define the frequency dependent noise source kernel as

$$K(x,\omega) = -u^\dagger(\mathbf{x},\omega)\, P\big[\, \circ, G(\mathbf{x},\mathbf{x}_0,\omega)\,\big]. \tag{2.27}$$

In the time domain, any definition of P includes an integral over angular frequency ω. Consequently, a noise source kernel can be defined in a similar way in the time domain. A kernel represents the first-order change of the measured misfit and tells us in our case where changes in the source distribution have an influence on the misfit. By construction, we can now compute $\nabla_S \mathcal{X}\, \delta S$ for any direction δS without the explicit knowledge of $\delta_S C$. The price we have to pay is to find the adjoint operator $\mathcal{L}^\dagger$ and to solve the adjoint problem according to equation (2.24). In non-dissipative media, the wave equation operator is self-adjoint, meaning that $\mathcal{L} = \mathcal{L}^\dagger$. The derivation of $\mathcal{L}^\dagger$ can be found, for example, in *Fichtner* (2010). In the time domain, the adjoint equation (2.24) has to be solved subject to terminal conditions, requiring that the adjoint wavefield is zero at time t_c. In practice, it is solved backwards in time, such that the terminal conditions act as initial conditions for the numerical simulation (*Tarantola*, 1988; *Tromp et al.*, 2005; *Plessix*, 2006; *Fichtner et al.*, 2006).

Example for membrane waves

After the derivation of the source kernel, we come back to the example introduced in section 2.1.2. Suppose we have a perfect Earth model for a certain study area and we calculate synthetic correlation functions for a homogeneous distribution of noise sources. Since noise sources at any frequency are heterogeneously distributed and non-stationary (*Ardhuin et al.*, 2011; *Stutzmann et al.*, 2012; *Ardhuin et al.*, 2015), there is a discrepancy between synthetics and observations. We are therefore interested in how each basis function $S_l(\mathbf{x})$ has to be changed to improve the fit between synthetics and observations. According

to equation (2.25) this is given by

$$\begin{aligned}\nabla_{S_l}\chi\,\delta S_l &= -\Big\langle u^\dagger\, P(\,\delta S_l, G\,)\Big\rangle \\ &= -\frac{1}{2\pi}\,\mathrm{Re}\int\limits_{\oplus}\int\limits_{\tau} u^\dagger(\mathbf{x},t)\,\delta S_l(\mathbf{x}) \int\limits_{w_l}^{w_{l+1}}\Big[\int\limits_{\tau} G(\mathbf{x},\mathbf{x}_0,t')\,e^{-i\omega t'}\,dt'\Big]^*\,e^{i\omega t}\,d\omega\,dt\,d\mathbf{x}.\end{aligned} \tag{2.28}$$

Since S_l is constant in the corresponding frequency band, the kernel K_l can be defined as

$$K_l(\mathbf{x}) = -\frac{1}{2\pi}\,\mathrm{Re}\int\limits_{\tau} u^\dagger(\mathbf{x},t) \int\limits_{w_l}^{w_{l+1}}\Big[\int\limits_{\tau} G(\mathbf{x},\mathbf{x}_0,t')\,e^{-i\omega t'}\,dt'\Big]^*\,e^{i\omega t}\,d\omega\,dt, \tag{2.29}$$

such that

$$\nabla_{S_l}\chi\,\delta S_l = \int\limits_{\oplus} K_l(\mathbf{x})\delta S_l(\mathbf{x})\,d\mathbf{x}. \tag{2.30}$$

The frequency dependence of the noise source is in this example honored by L noise source kernels, one for each basis function. The adjoint wavefield $u^\dagger(\mathbf{x})$ can be interpreted as a time reversed Green's function $G(\mathbf{x},\mathbf{x}_1,-t)$, with its source at the receiver $\mathbf{x}_1$ where the measurement is taken, convolved $\star$ with the adjoint source time function $f(t)$. We rewrite equation (2.29) accordingly and obtain

$$K_l(\mathbf{x}) = -\int\limits_{\tau} f(t)\star G(\mathbf{x},\mathbf{x}_1,-t)\,G_l(\mathbf{x},\mathbf{x}_0,-t)\,dt, \tag{2.31}$$

where we abbreviate the complex conjugate of the finite Fourier transform and its band-limited inverse, covering the angular frequencies of the corresponding basis function, with $G_l(\mathbf{x},\mathbf{x}_0,-t)$. Since the time reversed Green's function is purely acausal, the kernel has to be evaluated only for times $t \leq 0$. Examples of source kernels are presented in figure 2.2. The general shape is governed by the interaction of two Green's functions, one at the reference station $\mathbf{x}_0$ and the other at the receiver $\mathbf{x}_1$, leading to a superposition of hyperbolas with varying eccentricity (*Hanasoge*, 2013; *Fichtner*, 2015; *Ermert et al.*, 2016). Geometrically, a hyperbola can be defined as a set of points, for which the difference between any point and two foci, in our case the two receivers, is constant. Therefore, any source along one hyperbola contributes to the correlation waveform at a specific traveltime. Taking a measurement in a specific time window thus selects a set of hyperbolas and the measurement type can be interpreted as a weighting factor. The alternating signs of the hyperbolas indicate different Fresnel zones. For infinite frequency, the kernels collapse into rays starting at one focal point, directed away from the second.

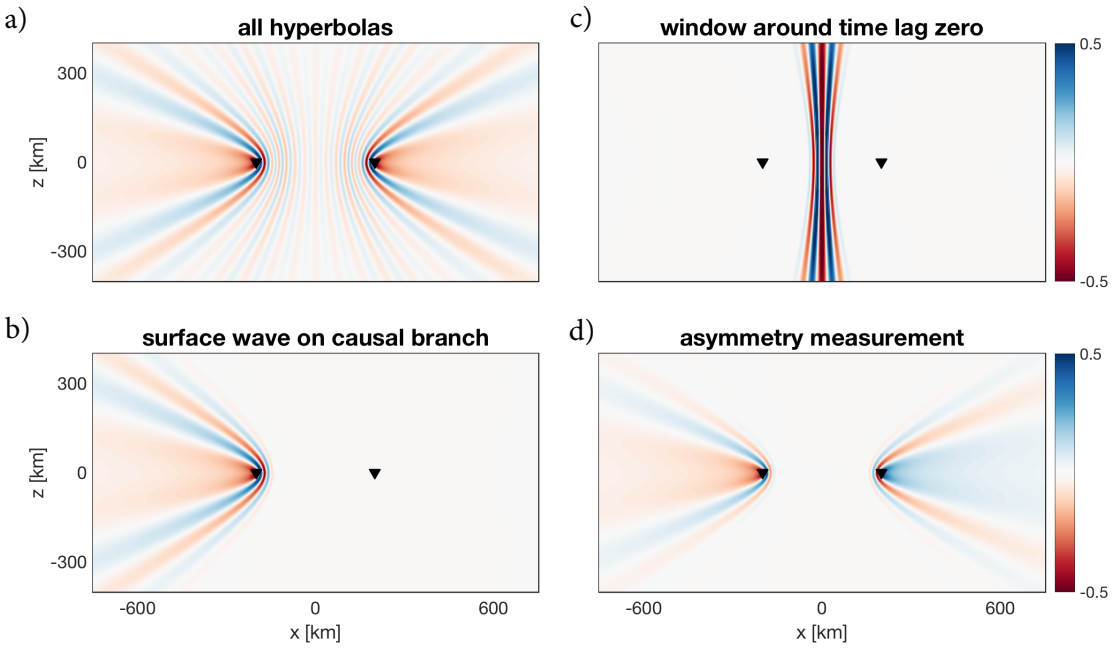

Figure 2.2: Effect of windowing and adjoint source time function on source kernels for a frequency band of $0.02 - 0.2$ Hz. a) The general shape of the source kernel, i.e. the hyperbolas are governed by two Green's functions. Windowing the correlation function, selects different parts of the sensitivity kernel, e.g. b) for the surface wave signal from 73 to 127 s or c) for times around zero lag from -10 to 10 s. Whereas the kernels in a) to c) are calculated for waveform differences, the kernel in d) corresponds to an asymmetry measurement, both computed without data. For details about the specific misfit functionals see section 3. Each source kernel is normalized and the color scale clipped at 0.5 to highlight more Fresnel zones.

2.2.1.2 Structure kernel

The assumption of having a perfect structure model as in the example above will, of course, never be fulfilled and missing Earth structure in the model $\mathbf{m}$ will contribute to discrepancies between synthetics and observations as well. Therefore, we follow the procedure described in section 2.2.1.1 in order to derive sensitivity kernels for material parameters $\mathbf{m}$. The directional derivative of the misfit functional $\mathcal{X}$ with respect to $\delta\mathbf{m}$ is given by

$$\nabla_{\mathbf{m}}\mathcal{X}\,\delta\mathbf{m} = \nabla_C\mathcal{X}\,\delta_{\mathbf{m}}C = \Big\langle \nabla_C\chi\,\delta_{\mathbf{m}}C \Big\rangle, \tag{2.32}$$

where

$$\delta_{\mathbf{m}}C = \nabla_{\mathbf{m}}C\,\delta\mathbf{m} \tag{2.33}$$

denotes the derivative of the correlation function C with respect to $\mathbf{m}$ in the direction of $\delta\mathbf{m}$. The problem in equation (2.32) is this time the appearance of $\delta_{\mathbf{m}}C$, which is computationally expensive to evaluate for all possible directions $\delta\mathbf{m}$. In order to again

eliminate the unpleasant term, we differentiate equation (2.9) with respect to $\mathbf{m}$

$$\nabla_{\mathbf{m}}\mathcal{L}(C)\,\delta\mathbf{m} + \mathcal{L}(\delta_{\mathbf{m}}C) - P(\,S, \delta_{\mathbf{m}}G\,) = 0, \tag{2.34}$$

where

$$\delta_{\mathbf{m}}G = \nabla_{\mathbf{m}}G\,\delta\mathbf{m} \tag{2.35}$$

represents the derivative of the Green's function G with respect to $\mathbf{m}$ in the direction of $\delta\mathbf{m}$. Please note that we obtain three terms in equation (2.34), because not only the correlation function C and the Green's function G depend on the material parameters $\mathbf{m}$, but also the operator $\mathcal{L}$.
Multiplying equation (2.34) with the adjoint wavefield $u^\dagger$ defined in equation (2.24), applying $\langle . \rangle$ and adding the term to equation (2.32) leads to

$$\delta_{\mathbf{m}}\chi = \Big\langle \nabla_C\chi\,\delta_{\mathbf{m}}C + u^\dagger\,\nabla_{\mathbf{m}}\mathcal{L}(C)\,\delta\mathbf{m} + u^\dagger\,\mathcal{L}(\delta_{\mathbf{m}}C) - u^\dagger\,P(\,S, \delta_{\mathbf{m}}G\,)\Big\rangle. \tag{2.36}$$

With the same set of adjoint operators defined before in equations (2.21) and (2.22), we eliminate terms one and three due to the definition of $u^\dagger$ and obtain

$$\nabla_{\mathbf{m}}\mathcal{X}\,\delta\mathbf{m} = \Big\langle u^\dagger\,\nabla_{\mathbf{m}}\mathcal{L}(C)\,\delta\mathbf{m} - u^\dagger\,P(\,S, \delta_{\mathbf{m}}G\,)\Big\rangle. \tag{2.37}$$

Since the source term for the correlation wavefield also depends on the material parameters $\mathbf{m}$ in terms of the Green's function G, we still have the term $\delta_{\mathbf{m}}G$ in equation (2.37) and the directional derivative cannot be evaluated for arbitrary directions $\delta\mathbf{m}$. Trying to eliminate $\delta_{\mathbf{m}}G$, we consider the derivative of equation (2.8) with respect to $\mathbf{m}$ in the direction $\delta\mathbf{m}$:

$$\nabla_{\mathbf{m}}\mathcal{L}(G)\,\delta\mathbf{m} + \mathcal{L}(\delta_{\mathbf{m}}G) = 0 \tag{2.38}$$

Following the procedure above, i.e. multiplying equation (2.38) with a test field $c^\dagger$, applying the integrals $\langle . \rangle$ and adding the resulting term to equation (2.37), yields

$$\nabla_{\mathbf{m}}\mathcal{X}\,\delta\mathbf{m} = \Big\langle u^\dagger\,\nabla_{\mathbf{m}}\mathcal{L}(C)\,\delta\mathbf{m} - u^\dagger\,P(\,S, \delta_{\mathbf{m}}G\,) + c^\dagger\,\nabla_{\mathbf{m}}\mathcal{L}(G)\,\delta\mathbf{m} + c^\dagger\mathcal{L}(\delta_{\mathbf{m}}G)\Big\rangle. \tag{2.39}$$

Now invoking a second pair of adjoint operators

$$\Big\langle u^\dagger\,P(\,S, \delta_{\mathbf{m}}G\,)\Big\rangle = \Big\langle \delta_{\mathbf{m}}G\,P^\dagger(\,S, u^\dagger\,)\Big\rangle, \tag{2.40}$$

$$\Big\langle c^\dagger\,\mathcal{L}(\delta_{\mathbf{m}}G)\Big\rangle = \Big\langle \delta_{\mathbf{m}}G\,\mathcal{L}^\dagger(c^\dagger)\Big\rangle, \tag{2.41}$$

we can alter equation (2.39) to

$$\nabla_{\mathbf{m}}\mathcal{X}\,\delta\mathbf{m} = \Big\langle u^\dagger\,\nabla_{\mathbf{m}}\mathcal{L}(C)\,\delta\mathbf{m} + c^\dagger\,\nabla_{\mathbf{m}}\mathcal{L}(G)\,\delta\mathbf{m} - \delta_{\mathbf{m}}G\,[\,P^\dagger(\,S, u^\dagger\,) - \mathcal{L}^\dagger(c^\dagger)\,]\Big\rangle. \tag{2.42}$$

When a field $c^\dagger$ can be found that satisfies the second adjoint equation given by

$$\mathcal{L}^\dagger(c^\dagger) = P^\dagger(\, S, u^\dagger\,), \tag{2.43}$$

the term $\delta_{\mathbf{m}} G$ is eliminated. The derivative of the misfit functional $\mathcal{X}$ with respect to material parameters $\mathbf{m}$ can then be computed for any direction $\delta\mathbf{m}$ by

$$\nabla_{\mathbf{m}}\mathcal{X}\,\delta\mathbf{m} = \Big\langle u^\dagger\,\nabla_{\mathbf{m}}\mathcal{L}(C)\,\delta\mathbf{m} + c^\dagger\,\nabla_{\mathbf{m}}\mathcal{L}(G)\,\delta\mathbf{m}\Big\rangle = \int\limits_{\oplus} K(\mathbf{x})\,\delta\mathbf{m}\,d\mathbf{x}, \tag{2.44}$$

where the sensitivity kernel K is in the time domain defined as

$$K(\mathbf{x}) = \int\limits_{\tau} u^\dagger\,\nabla_{\mathbf{m}}\mathcal{L}(C) + c^\dagger\,\nabla_{\mathbf{m}}\mathcal{L}(G)\,dt. \tag{2.45}$$

For the computation of sensitivity kernels for Earth structure, two adjoint equations given by equations (2.24) and (2.43) have to be solved. The steps in solving the adjoint equations follow the recipe introduced in section 2.1 to forward model correlation functions: First, a wavefield $u^\dagger$ is computed, which is then combined with the power-spectral density distribution according to $P^\dagger(\, S, u^\dagger\,)$. The combination then drives in the last step a second wavefield $c^\dagger$ as a distributed source following equation (2.43). For a further interpretation of the second adjoint wavefield, we first consider the right-hand side of equation (2.43) in the frequency domain and for a self-adjoint operator P, meaning that $P = P^\dagger$. We can then write

$$P^\dagger[\, S(\mathbf{x},\omega), u^\dagger(\mathbf{x},\omega)\,] = S(\mathbf{x},\omega)\,u^{\dagger *}(\mathbf{x},\omega). \tag{2.46}$$

Using equation (2.46) as the source term in the scalar version of the representation theorem in equation (2.2) and writing again $u^\dagger = f(\omega)\; G^*(\mathbf{x},\mathbf{x}_1,\omega)$, we obtain

$$c^\dagger(\mathbf{x},\omega) = f^*(\omega) \int\limits_{\oplus} G^*(\mathbf{x},\boldsymbol{\xi},\omega)\Big[S(\mathbf{x},\omega)G(\mathbf{x}_1,\boldsymbol{\xi},\omega)\Big]\,d\boldsymbol{\xi}, \tag{2.47}$$

where the first Green's function $G^*(\mathbf{x},\boldsymbol{\xi})$ is time reversed, since $c^\dagger$ is an adjoint wavefield. Comparing equation (2.47) to the correlation wavefield given by expression (2.7), $c^\dagger$ can be interpreted as an adjoint correlation wavefield with a reference station at $\mathbf{x}_1$, modulated with the adjoint source time function $f(\omega)$.

Link to formulation by Fichtner (2015)[3]

For a link between the derivation presented in section 2.2.1.2 and in *Fichtner* (2015), we start from equation (2.44)

$$\nabla_{\mathbf{m}}\mathcal{X}\,\delta\mathbf{m} = \Big\langle u^{\dagger}_{(2)}\,\nabla_{\mathbf{m}}\mathcal{L}(C)\,\delta\mathbf{m} + c^{\dagger}\,\nabla_{\mathbf{m}}\mathcal{L}(G)\,\delta\mathbf{m}\Big\rangle, \tag{2.48}$$

where we refer to $u^{\dagger}_{(n)}$ as the adjoint wavefield that corresponds to the correlation wavefield at reference station $\mathbf{x}_n$. In the frequency domain it can be written as

$$\begin{aligned}\nabla_{\mathbf{m}}\mathcal{X}\,\delta\mathbf{m} = &\underbrace{\int_{\oplus}\int_{-\infty}^{\infty} u^{\dagger}_{(2)}(\mathbf{x},\omega)\,\nabla_{\mathbf{m}}\mathcal{L}[C(\mathbf{x},\mathbf{x}_0,\omega)]\,\delta\mathbf{m}\,d\omega\,d\mathbf{x}}_{(1)}\\ &+\underbrace{\int_{\oplus}\int_{-\infty}^{\infty} c^{\dagger}(\mathbf{x},\omega)\,\nabla_{\mathbf{m}}\mathcal{L}[G(\mathbf{x},\mathbf{x}_0,\omega)]\,\delta\mathbf{m}\,d\omega\,d\mathbf{x}}_{(2)}.\end{aligned} \tag{2.49}$$

With the definition of the adjoint correlation wavefield $c^{\dagger}$ according to equation (2.47), which is defined by

$$c^{\dagger}(\mathbf{x},\omega) = \int_{\oplus} G^{*}(\mathbf{x},\xi,\omega)\,S(\xi,\omega)\,G(\xi,\mathbf{x}_1)\,f^{*}(\omega)\,d\xi, \tag{2.50}$$

the second part of equation (2.49) is given by

$$(2) = \int_{\oplus}\int_{-\infty}^{\infty}\Big[\int_{\oplus} G^{*}(\mathbf{x},\xi,\omega)\,S(\xi,\omega)\,G(\xi,\mathbf{x}_1)\,f^{*}(\omega)\,d\xi\Big]\,\nabla_{\mathbf{m}}\mathcal{L}(G(\mathbf{x},\mathbf{x}_0,\omega))\,\delta\mathbf{m}\,d\omega\,d\mathbf{x}. \tag{2.51}$$

Since $\nabla_{\mathbf{m}}\mathcal{L}$ is linear, we write

$$(2) = \int_{\oplus}\int_{-\infty}^{\infty}\Big[\int_{\oplus} G^{*}(\mathbf{x},\xi,\omega)\,S(\xi,\omega)\,G(\xi,\mathbf{x}_1)\,d\xi\Big]\,\nabla_{\mathbf{m}}\mathcal{L}(f^{*}(\omega)G(\mathbf{x},\mathbf{x}_0,\omega))\,\delta\mathbf{m}\,d\omega\,d\mathbf{x}, \tag{2.52}$$

and observe that $\nabla_{\mathbf{m}}\mathcal{L}$ is acting on $f^{*}(\omega)G(\mathbf{x},\mathbf{x}_0,\omega)$, which is the adjoint wavefield $u^{\dagger *}_{(1)}(\mathbf{x},\omega)$ for the reference station at $\mathbf{x}_1$ and the corresponding measurement at station $\mathbf{x}_0$. Equation (2.52) thus changes to

$$(2) = \int_{\oplus}\int_{-\infty}^{\infty} C(\mathbf{x},\mathbf{x}_1,\omega)\,\nabla_{\mathbf{m}}\mathcal{L}(u^{\dagger *}_{(1)}(\mathbf{x},\omega))\,\delta\mathbf{m}\,d\omega\,d\mathbf{x}. \tag{2.53}$$

[3]This part is presented in the appendix of the original publication.

Using the adjoint operator defined in equation (2.22), we obtain

$$(2) = \int\limits_{\oplus} \int\limits_{-\infty}^{\infty} u^{\dagger *}_{(1)}(\mathbf{x}, \omega)\, \nabla_{\mathbf{m}} \mathcal{L}^{\dagger}(C(\mathbf{x}, \mathbf{x}_1, \omega))\, \delta\mathbf{m}\, d\omega\, d\mathbf{x}. \tag{2.54}$$

Part 1 of equation (2.49) together with expression (2.54) correspond to equation (32) in *Fichtner* (2015). As expected due to the nature of correlation functions, the final expression is Hermitian in the exchange of $\mathbf{x}_1$ and $\mathbf{x}_0$. For a full evaluation of the gradient according to the expression by *Fichtner* (2015), the wavefield for all reference stations has to be computed. Our derivation allows us to optimize the array in terms of simulations and coverage, convenient due to the high computational costs of full waveform ambient noise inversion.

Example for membrane waves[4]
Similar to the derivation of the adjoint operator $\mathcal{L}^{\dagger}$, the explicit form of $P^{\dagger}$ depends on the definition of P. A derivation for our example case is given in the following.
Starting from expression (2.40), we use the definition of P in equation (2.13) and write

$$\begin{aligned} &\left\langle u^{\dagger}\, P(\, S, \delta_{\mathbf{m}} G\,) \right\rangle \\ &\quad = -\frac{1}{2\pi}\, \mathrm{Re} \int\limits_{\oplus} \int\limits_{\tau} u^{\dagger}(\mathbf{x}, t)\, \sum_{l} S_l(\mathbf{x}) \int\limits_{w_l}^{w_{l+1}} \Big[\int\limits_{\tau} \delta_{\mathbf{m}} G(\mathbf{x}, \mathbf{x}_0, t')\, e^{-i\omega t'}\, dt' \Big]^{*} e^{i\omega t}\, d\omega\, dt\, d\mathbf{x}. \end{aligned} \tag{2.55}$$

Reordering the integrals and the summation over basis functions, we obtain

$$-\frac{1}{2\pi}\, \mathrm{Re} \sum_{l} \int\limits_{\oplus} S_l(\mathbf{x}) \int\limits_{\tau} \int\limits_{w_l}^{w_{l+1}} \int\limits_{\tau} u^{\dagger}(\mathbf{x}, t)\, \delta_{\mathbf{m}} G(\mathbf{x}, \mathbf{x}_0, t') e^{i\omega t'} e^{i\omega t}\, dt'\, d\omega\, dt\, d\mathbf{x}. \tag{2.56}$$

Isolating the adjoint wavefield $u^{\dagger}$ together with the exponential function $e^{i\omega t}$, equation (2.56) changes to

$$-\frac{1}{2\pi}\, \mathrm{Re} \sum_{l} \int\limits_{\oplus} S_l(\mathbf{x}) \int\limits_{\tau} \delta_{\mathbf{m}} G(\mathbf{x}, \mathbf{x}_0, t') \int\limits_{w_l}^{w_{l+1}} \int\limits_{\tau} u^{\dagger}(\mathbf{x}, t) e^{i\omega t}\, dt\, e^{i\omega t'}\, d\omega\, dt'\, d\mathbf{x}. \tag{2.57}$$

The innermost integral is a Fourier transform of the adjoint wavefield $u^{\dagger}$. If we take the complex conjugate of the Fourier transform, taking into account that $u^{\dagger}(\mathbf{x}, t)$ is real, and

[4] The derivation of $P^{\dagger}$ is presented in the appendix of the original publication.

reordering the integrals and summation, we get

$$-\frac{1}{2\pi}\,\mathrm{Re}\int\limits_{\oplus}\int\limits_{\tau}\delta_{\mathbf{m}}G(\mathbf{x},\mathbf{x}_0,t')\sum_l S_l(\mathbf{x})\int\limits_{w_l}^{w_{l+1}}\Big[\int\limits_{\tau}u^{\dagger}(\mathbf{x},t)\,e^{-i\omega t}dt\Big]^{*}e^{i\omega t'}\,d\omega\,dt'\,d\mathbf{x} \\ =\Big\langle\delta_{\mathbf{m}}G\;P^{\dagger}(\,S,u^{\dagger}\,)\Big\rangle. \tag{2.58}$$

For the last step, we compare equation (2.58) to (2.55) and observe that this is exactly what we try to retrieve. In this case, the definitions of P and $P^{\dagger}$ are the same and P is therefore self-adjoint.

In addition, we apply the general expression for the derivative of the objective function $\mathcal{X}$ in direction $\delta\mathbf{m}$ (equation (2.44)) to membrane waves and, for simplicity, only to variations in density ρ. Using the wave operator defined in equation (2.10), we obtain for the derivative of the wave equation operator with respect to ρ

$$\nabla_{\rho}\mathcal{L}(\circ)\,\delta\rho=\delta\rho\,\partial_{tt}\circ\,. \tag{2.59}$$

Consequently, we find

$$\nabla_{\mathbf{m}}\mathcal{X}\,\delta\mathbf{m}=\Big\langle u^{\dagger}\,\partial_{tt}C\,\delta\rho+c^{\dagger}\,\partial_{tt}G\,\delta\rho\Big\rangle=\int\limits_{\oplus}K_{\rho}(\mathbf{x})\,\delta\rho\,d\mathbf{x}. \tag{2.60}$$

Integration by parts and using the terminal conditions for the adjoint wavefield provides a more symmetric version of the density kernel, which is convenient for numerical simulations, and is given by

$$K_{\rho}(\mathbf{x})=-\int\limits_{\tau}\partial_t u^{\dagger}(\mathbf{x},t)\,\partial_t C(\mathbf{x},t)\;+\partial_t c^{\dagger}(\mathbf{x},t)\,\partial_t G(\mathbf{x},t)\,dt. \tag{2.61}$$[5]

Following the same recipe, kernels can be derived for elastic parameters or seismic velocities. Examples for structure kernels for different source distributions are illustrated in figure 2.3. Inherent in each structure kernel are elliptical features. For any point along an ellipse, the sum of the distances to two foci is constant. A change of the medium at any of these points therefore affects the waveforms at a specific traveltime. For a point source and two receivers, the structure kernel is composed of ellipses, each with one focal point at the source position and the other at one of the receivers. Any other source distribution can be explained by a superposition of point sources. For the special case of a homogeneous distribution of noise sources, the sensitivity to each noise source location vanishes and the two focal points are located at the receivers. The kernel then resembles finite-frequency

[5] Error in the original publication. The minus from the integration by parts is missing. We thank Zongbo Xu for pointing it out.

kernels for earthquake tomography (*Dahlen et al.*, 2000; *Dahlen and Baig*, 2002; *Zhou et al.*, 2004; *Tromp et al.*, 2005). The kernel width is again determined by the frequency content.

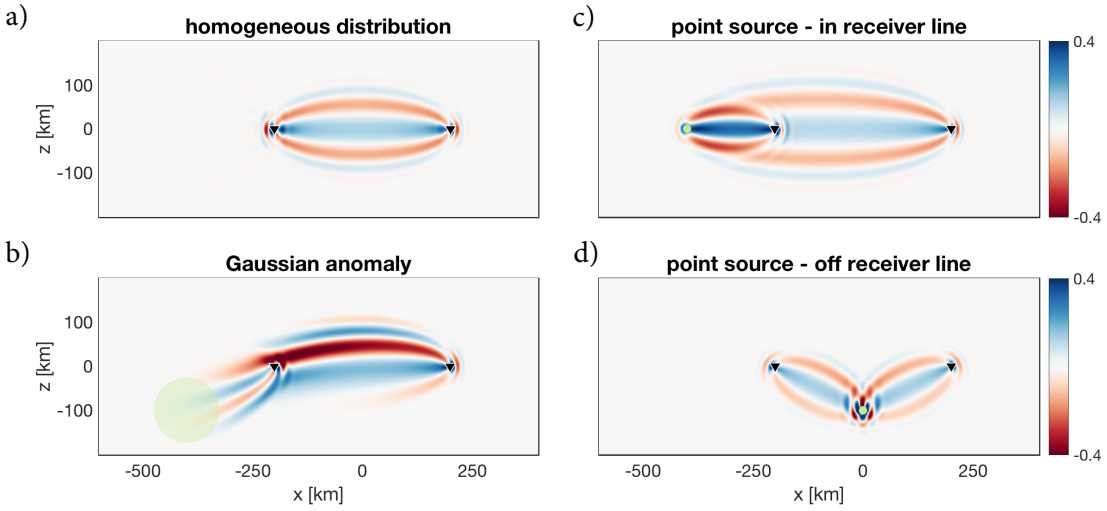

Figure 2.3: Structure kernels for four different source distributions: a) homogeneous, b) Gaussian anomaly and two point sources in c) and d). In the last three scenarios, the source anomalies are indicated in green colors. All kernels are calculated for a frequency band of 0.02 to 0.2 Hz using waveform differences as misfit functional, computed without data. Each source kernel is normalized and the color scale clipped at 0.5 to highlight more Fresnel zones.

2.2.2 Second derivatives[6]

With the developments above, we can attribute differences in synthetic and observed correlation functions either to the material parameters $\mathbf{m}$ or to the power-spectral density distribution S_{nm}. In order to establish the foundation of a resolution analysis that accounts for the resulting trade-offs between noise sources and Earth structure, we extend the theory to the computation of second derivatives. In the context of probabilistic inverse problems, the inverse Hessian matrix in the vicinity of the global model and under the assumption of Gaussian statistics can be interpreted as an approximation of the posterior covariance matrix (*Tarantola*, 2005; *Fichtner and Trampert*, 2011). The Hessian matrix therefore contains all the information on resolution and trade-offs that we are trying to retrieve. For the sake of a clean notation we again present the derivation only for the scalar case, while the same recipe applies for the extension to elastic media.

[6]Expect for mixed source-structure derivatives applied to a perturbation $\delta\mathbf{m}$, second derivatives are presented in the appendix of the original publication.

2.2.2.1 Mixed source-structure derivative H_{ms}

The basic principles of the adjoint method applied above to get an efficient formulation for the computation of first derivatives, are reused in the following to compute second derivatives. We start with the directional derivative of the misfit functional $\mathcal{X}$ with respect to $\delta\mathbf{m}$, which is given by

$$\nabla_{\mathbf{m}}\mathcal{X}\,\delta\mathbf{m} = \nabla_C\mathcal{X}\,\delta_{\mathbf{m}}C = \Big\langle \nabla_C\chi\,\delta_{\mathbf{m}}C \Big\rangle. \tag{2.62}$$

Since we are interested in mixed derivatives, we differentiate equation (2.62) again, but now with respect to S, i.e. we get

$$H_{ms}(\,\delta\mathbf{m},\delta S\,) = \nabla_S\nabla_{\mathbf{m}}\mathcal{X}\,\delta\mathbf{m}\,\delta S = \Big\langle \nabla_C\nabla_C\chi\,\delta_{\mathbf{m}}C\,\delta_S C + \nabla_C\chi\,\delta_{\mathbf{m}S}C \Big\rangle, \tag{2.63}$$

where

$$\delta_{\mathbf{m}S}C = \nabla_S\nabla_{\mathbf{m}}\,C\,\delta\mathbf{m}\,\delta S \tag{2.64}$$

denotes the second-order variation of the correlation function C with a perturbation in $\mathbf{m}$ and in S, and $H_{ms}(\,\delta\mathbf{m},\delta S\,)$ denotes the Hessian with mixed derivatives applied to the directions $\delta\mathbf{m}$ and δS. The problem in equation (2.63) is not only the combined appearance of $\delta_{\mathbf{m}}C$ and $\delta_S C$, but also the second derivative of the correlation function $\delta_{\mathbf{m}S}C$, which would be even more expensive to evaluate for all possible directions $\delta\mathbf{m}$ and δS. Trying to eliminate the latter, we differentiate equation (2.9) with respect to S and then again with respect to $\mathbf{m}$, yielding

$$\mathcal{L}(\delta_S C) - P(\,\delta S, G\,) = 0, \tag{2.65}$$

$$\nabla_{\mathbf{m}}\mathcal{L}(\delta_S C)\,\delta\mathbf{m} + \mathcal{L}(\delta_{\mathbf{m}S}C) - P(\,\delta S,\delta_{\mathbf{m}}G\,) = 0. \tag{2.66}$$

Using again the adjoint wavefield $u^\dagger$ and the two integrals over space and time/frequency $\langle . \rangle$ introduced in equation (2.14) in the same manner as before, but now with equation (2.63), leads to

$$\begin{aligned} H_{ms}(\,\delta\mathbf{m},\delta S\,) = \Big\langle & \nabla_C\nabla_C\chi\,\delta_{\mathbf{m}}C\,\delta_S C + \nabla_C\chi\,\delta_{\mathbf{m}S}C \\ & + u^\dagger\,\nabla_{\mathbf{m}}\mathcal{L}(\delta_S C)\,\delta\mathbf{m} + u^\dagger\,\mathcal{L}(\delta_{\mathbf{m}S}C) - u^\dagger\,P(\,\delta S,\delta_{\mathbf{m}}G\,) \Big\rangle. \end{aligned} \tag{2.67}$$

With the set of adjoint operators defined in equations (2.21) and (2.22), we can eliminate terms two and four due to the definition of $u^\dagger$ in equation (2.24) and obtain

$$H_{ms}(\,\delta\mathbf{m},\delta S\,) = \Big\langle \nabla_C\nabla_C\chi\,\delta_{\mathbf{m}}C\,\delta_S C + u^\dagger\,\nabla_{\mathbf{m}}\mathcal{L}(\delta_S C)\,\delta\mathbf{m} - u^\dagger\,P(\,\delta S,\delta_{\mathbf{m}}G\,) \Big\rangle, \tag{2.68}$$

where only first derivatives of the correlation function and the Green's function are involved. Unfortunately, the choice of the first direction determines the effect of the second and it is therefore not possible to get a general expression for the Hessian operator that can be

evaluated easily for all possible directions for $\delta\mathbf{m}$ and for δS. Our strategy is therefore to choose one direction either for $\delta\mathbf{m}$ or δS and try to get an expression for $H_{ms}(\,\delta\mathbf{m}, \circ\,)$ or $H_{ms}(\,\circ, \delta S\,)$, also known as Hessian-vector product, which can be evaluated for all possible directions δS or $\delta\mathbf{m}$, respectively. We use the same order of the subscripts for both cases, i.e. H_{ms}, since the Hessian matrix is symmetric.

Direction chosen for $\delta\mathbf{m}$

We define the adjoint wavefield $p^\dagger$ by

$$\mathcal{L}^\dagger(p^\dagger) = -\nabla_C \nabla_C \chi^\dagger \, \delta_{\mathbf{m}} C - \nabla_{\mathbf{m}} \mathcal{L}^\dagger(u^\dagger), \tag{2.69}$$

and invoke the adjoint operators

$$\Big\langle [\nabla_C \nabla_C \chi \, \delta_{\mathbf{m}} C] \, \delta_S C = \delta_S C \, [\nabla_C \nabla_C \chi^\dagger \, \delta_{\mathbf{m}} C] \Big\rangle \tag{2.70}$$

and

$$\Big\langle u^\dagger \, \nabla_{\mathbf{m}} \mathcal{L}(\delta_S C) = \delta_S C \, \nabla_{\mathbf{m}} \mathcal{L}^\dagger(u^\dagger) \Big\rangle. \tag{2.71}$$

With the definition of $p^\dagger$ and the two adjoint operators, we can change equation (2.68) to

$$\begin{aligned} H_{ms}(\,\delta\mathbf{m}, \delta S\,) &= \Big\langle -\delta_S C \, \mathcal{L}^\dagger(p^\dagger) - u^\dagger \, P(\,\delta S, \delta_{\mathbf{m}} G\,) \Big\rangle \\ &= \Big\langle -p^\dagger \, \mathcal{L}(\delta_S C) - u^\dagger \, P(\,\delta S, \delta_{\mathbf{m}} G\,) \Big\rangle. \end{aligned} \tag{2.72}$$

With equation (2.65) we remove $\mathcal{L}(\delta_S C)$ from equation (2.72) and replace it with $P(\,\delta S, G\,)$. Since δS then only appears explicitly, we write

$$H_{ms}(\,\delta\mathbf{m}, \circ\,) = \Big\langle -p^\dagger \, P(\,\circ, G\,) - u^\dagger \, P(\,\circ, \delta_{\mathbf{m}} G\,) \Big\rangle \tag{2.73}$$

to illustrate that it can be evaluated for all possible directions δS. Following the idea used in expression (2.26), a Hessian kernel can be defined in a similar way. The Hessian-vector product $H_{ms}(\,\delta\mathbf{m}, \circ\,)$ can be interpreted as the first-order change in the sensitivity to the distribution of noise sources caused by a perturbation $\delta\mathbf{m}$ in the structure model, which we can think of as a scatterer without loss of generality. The source kernel according to equation (2.27) is composed of two components: the adjoint wavefield $u^\dagger$ and the Green's function G. The change of either one of them is accounted for by the two terms in equation (2.73). The wavefield $p^\dagger$ describes the change of the adjoint wavefield $u^\dagger$ caused by scattering of the adjoint and the correlation wavefield, where the latter affects the misfit that drives the adjoint wavefield $u^\dagger$. The second term in equation (2.73) accounts for the scattering of the Green's function. A direct interaction of the change in the adjoint wavefield and the change in the Green's function would lead to higher order terms.

Direction chosen for δS

We again define the adjoint wavefield $p^\dagger$, but now as

$$\mathcal{L}^\dagger(p^\dagger) = -\nabla_C \nabla_C \chi^\dagger \, \delta_S C. \tag{2.74}$$

Following the same procedure as before, we obtain

$$H_{ms}(\, \delta\mathbf{m}, \delta S \,) = \Big\langle -p^\dagger \, \mathcal{L}(\delta_\mathbf{m} C) + u^\dagger \, \nabla_\mathbf{m} \mathcal{L}(\delta_S C) \, \delta\mathbf{m} - u^\dagger \, P(\, \delta S, \delta_\mathbf{m} G \,) \Big\rangle. \tag{2.75}$$

Replacing $\mathcal{L}(\delta_\mathbf{m} C)$ in the first term using the first derivative of equation (2.9) with respect to structure, changes the expression for H_{ms} accordingly to

$$\begin{aligned} H_{ms}(\, \delta\mathbf{m}, \delta S \,) = \Big\langle & p^\dagger \, \nabla_\mathbf{m} \mathcal{L}(C) \, \delta\mathbf{m} + u^\dagger \, \nabla_\mathbf{m} \mathcal{L}(\delta_S C) \, \delta\mathbf{m} \\ & - p^\dagger \, P(\, S, \delta_\mathbf{m} G \,) - u^\dagger \, P(\, \delta S, \delta_\mathbf{m} G \,) \Big\rangle. \end{aligned} \tag{2.76}$$

Term three and four in equation (2.76) prohibit the evaluation of $H_{ms}(\, \circ, \delta S \,)$ for all possible directions $\delta\mathbf{m}$. To eliminate the third term, we multiply the first derivative of the PDE describing the computation of the Green's function in equation (2.8) with the adjoint wavefield $z^\dagger$, apply $\langle . \rangle$ and add it to equation (2.76). To facilitate the understanding, we only write down the terms of interest, which are given by

$$\begin{aligned} \Big\langle -p^\dagger \, P(\, S, \delta_\mathbf{m} G \,) \Big\rangle &= \Big\langle -p^\dagger \, P(\, S, \delta_\mathbf{m} G \,) + z^\dagger \, \nabla_\mathbf{m} \mathcal{L}(G) \, \delta\mathbf{m} + z^\dagger \, \mathcal{L}(\delta_\mathbf{m} G) \Big\rangle \\ &= \Big\langle -\delta_\mathbf{m} G \, P^\dagger(\, S, p^\dagger \,) + z^\dagger \, \nabla_\mathbf{m} \mathcal{L}(G) \, \delta\mathbf{m} + \delta_\mathbf{m} G \, \mathcal{L}^\dagger(z^\dagger) \Big\rangle, \end{aligned} \tag{2.77}$$

where we invoke again the adjoint operators in the second line defined in equations (2.40) and (2.41). If we can now find a wavefield $z^\dagger$ that satisfies

$$\mathcal{L}^\dagger(z^\dagger) = P^\dagger(\, S, p^\dagger \,), \tag{2.78}$$

we can eliminate the first appearance of $\delta_\mathbf{m} G$ in equation (2.76) and the third term is replaced by $z^\dagger \, \nabla_\mathbf{m} \mathcal{L}(G) \, \delta\mathbf{m}$. Following the exact same procedure for the fourth term, now naming the adjoint wavefield $q^\dagger$, we obtain

$$\Big\langle -u^\dagger \, P(\, \delta S, \delta_\mathbf{m} G \,) \Big\rangle = \Big\langle -u^\dagger \, P(\, \delta S, \delta_\mathbf{m} G \,) + q^\dagger \, \nabla_\mathbf{m} \mathcal{L}(G) \, \delta\mathbf{m} + q^\dagger \, \mathcal{L}(\delta_\mathbf{m} G) \Big\rangle, \tag{2.79}$$

and the unpleasant term $\delta_\mathbf{m} G$ vanishes, if a wavefield can be found that satisfies

$$\mathcal{L}^\dagger(q^\dagger) = P^\dagger(\, \delta S, u^\dagger \,). \tag{2.80}$$

Bringing it all together, equation (2.76) changes to

$$\begin{aligned} H_{ms}(\,\delta\mathbf{m},\delta S\,) = \Big\langle & p^\dagger\,\nabla_{\mathbf{m}}\mathcal{L}(C)\,\delta\mathbf{m} + u^\dagger\,\nabla_{\mathbf{m}}\mathcal{L}(\delta_S C)\,\delta\mathbf{m} \\ & + z^\dagger\nabla_{\mathbf{m}}\mathcal{L}(G)\,\delta\mathbf{m} + q^\dagger\nabla_{\mathbf{m}}\mathcal{L}(G)\,\delta\mathbf{m}\Big\rangle, \end{aligned} \tag{2.81}$$

and the Hessian-vector product $H_{ms}(\,\circ,\delta S\,)$ can be defined as

$$\begin{aligned} H_{ms}(\,\circ,\delta S\,) = & \Big\langle p^\dagger\,\nabla_{\mathbf{m}}\mathcal{L}(C)\,\circ\Big\rangle + \Big\langle u^\dagger\,\nabla_{\mathbf{m}}\mathcal{L}(\delta_S C)\,\circ\Big\rangle \\ & + \Big\langle z^\dagger\nabla_{\mathbf{m}}\mathcal{L}(G)\,\circ\Big\rangle + \Big\langle q^\dagger\nabla_{\mathbf{m}}\mathcal{L}(G)\,\circ\Big\rangle. \end{aligned} \tag{2.82}$$

To interpret $H_{ms}(\,\circ,\delta S\,)$, we first study the expression (2.44) for the computation of the structure kernel. In the first term, the adjoint wavefield $u^\dagger$ interacts with the correlation wavefield C and, in the second term, the adjoint correlation wavefield $c^\dagger$ with the Green's function G. As a consequence, the first-order change of the structure kernel given by equation (2.82), has four terms: interaction of 1) C with the change $p^\dagger$ of the adjoint wavefield due to the altered misfit functional, 2) the adjoint wavefield with the altered correlation wavefield $\delta_S C$, 3) G with the modified adjoint correlation wavefield $z^\dagger$[7] because of the change of its forcing term in terms of $p^\dagger$ (equation (2.78)) and 4) G with the modified adjoint correlation wavefield $q^\dagger$ due to a change in S (equation (2.80)). Since both $z^\dagger$ and $q^\dagger$ interact with the Green's function G and due to the linearity of the wave equation to the right-hand side, the two adjoint wavefields can be simulated simultaneously.

2.2.2.2 Second derivative with respect to the distribution of sources

In order to derive second derivatives only with respect to source, we start with the directional derivative of the misfit function $\mathcal{X}$ with respect to S in the direction of δS_1

$$\nabla_S\mathcal{X}\,\delta S_1 = \Big\langle \nabla_C\chi\,\delta_{S_1}C\Big\rangle. \tag{2.83}$$

We differentiate equation (2.83) again with respect to S, but now in the second direction δS_2, which is given by

$$\begin{aligned} H_{ss}(\,\delta S_1,\delta S_2\,) &= \nabla_S\nabla_S\mathcal{X}\,\delta S_1\,\delta S_2 \\ &= \Big\langle \nabla_C\nabla_C\chi\,\delta_{S_1}C\,\delta_{S_2}C + \nabla_C\chi\,\delta_{S_1S_2}C\Big\rangle, \end{aligned} \tag{2.84}$$

where

$$\delta_{S_1S_2}C = \nabla_S\nabla_S\,C\,\delta S_1\,\delta S_2 \tag{2.85}$$

[7] Error in the original publication. Corrected from $p^\dagger$ to $z^\dagger$.

denotes the second-order variation of the correlation function C due to two perturbations δS_1 and δS_2. Since the correlation function is linear in S, we have

$$\delta_{S_1 S_2} C = 0, \tag{2.86}$$

and equation (2.84) simplifies to

$$H_{ss}(\,\delta S_1, \delta S_2\,) = \Big\langle \nabla_C \nabla_C \chi \, \delta_{S_1} C \, \delta_{S_2} C \Big\rangle. \tag{2.87}$$

Invoking the adjoint operator in equation (2.70) and inserting the adjoint wavefield $p^\dagger$, defined by

$$\mathcal{L}^\dagger(p^\dagger) = -\nabla_C \nabla_C \chi^\dagger \, \delta_{S_1} C, \tag{2.88}$$

into equation (2.87), we obtain for H_{ss} applied to δS_1 and δS_2

$$H_{ss}(\,\delta S_1, \delta S_2\,) = \Big\langle -\delta_{S_2} C \, \mathcal{L}^\dagger(p^\dagger) \Big\rangle. \tag{2.89}$$

Using the adjoint operator in equation (2.22) and the first variation of the PDE describing the modeling of the correlation wavefield due to δS (equation (2.17)), $H_{ss}(\,\delta S_1, \delta S_2\,)$ changes to

$$H_{ss}(\,\delta S_1, \delta S_2\,) = \Big\langle -p^\dagger \, \mathcal{L}(\delta_{S_2} C) \Big\rangle = \Big\langle -p^\dagger \, P(\,\delta S_2, G\,) \Big\rangle, \tag{2.90}$$

and the Hessian-vector product is given by

$$H_{ss}(\,\delta S_1, \circ\,) = \Big\langle -p^\dagger \, P(\,\circ, G\,) \Big\rangle. \tag{2.91}$$

By design, equation (2.91) allows us to compute the change of the source kernel due to a perturbation δS_1 in the source distribution. The only term in equation (2.27) describing the computation of the source kernel that is changed by a perturbation in the source distribution is the adjoint wavefield $u^\dagger$. The source perturbation δS_1 changes the correlation function C to $\delta_{S_1} C$, which alters the misfit and consequently also the adjoint wavefield. The latter is accounted for in equation (2.91) by the adjoint wavefield $p^\dagger$, driven by the change of the misfit $\nabla_C \chi \, \delta_{S_1} C$. A convenient consequence is that the routines implemented for the computation of the source kernel can be reused for equation (2.91) and only the adjoint source time function has to be adapted accordingly.

2.2.2.3 Second derivative with respect to structure

The last piece that is missing for a full assembly of the Hessian matrix is the computation of second derivatives only with respect to structure. We start again with the first derivative of the misfit function with respect to $\mathbf{m}$ in the direction $\delta\mathbf{m}_1$

$$\nabla_{\mathbf{m}}\mathcal{X}\,\delta\mathbf{m}_1 = \Big\langle \nabla_C\chi\,\delta_{\mathbf{m}_1}C \Big\rangle, \tag{2.92}$$

and differentiate a second time, but now in the direction of $\delta\mathbf{m}_2$ to obtain

$$\begin{aligned} H_{mm}(\,\delta\mathbf{m}_1,\delta\mathbf{m}_2\,) &= \nabla_{\mathbf{m}}\nabla_{\mathbf{m}}\mathcal{X}\,\delta\mathbf{m}_1\,\delta\mathbf{m}_2 \\ &= \Big\langle \nabla_C\nabla_C\chi\,\delta_{\mathbf{m}_1}C\,\delta_{\mathbf{m}_2}C + \nabla_C\chi\,\delta_{\mathbf{m}_1\mathbf{m}_2}C \Big\rangle, \end{aligned} \tag{2.93}$$

where

$$\delta_{\mathbf{m}_1\mathbf{m}_2}C = \nabla_{\mathbf{m}}\nabla_{\mathbf{m}}C\,\delta\mathbf{m}_1\,\delta\mathbf{m}_2 \tag{2.94}$$

is the second-order variation of the correlation C due to $\delta\mathbf{m}_1$ and $\delta\mathbf{m}_2$. In the following, we try again to eliminate unpleasant terms and therefore prepare convenient tools in terms of the first and second derivative of the PDE describing the computation of correlation functions C, given by

$$\nabla_{\mathbf{m}}\mathcal{L}(C)\,\delta\mathbf{m}_1 + \mathcal{L}(\delta_{\mathbf{m}_1}C) - P(\,S,\delta_{\mathbf{m}_1}G\,) = 0, \tag{2.95}$$

$$\begin{aligned} \nabla_{\mathbf{m}}\nabla_{\mathbf{m}}\mathcal{L}(C)\,\delta\mathbf{m}_1\,\delta\mathbf{m}_2 + \nabla_{\mathbf{m}}\mathcal{L}(\delta_{\mathbf{m}_2}C)\,\delta\mathbf{m}_1 + \nabla_{\mathbf{m}}\mathcal{L}(\delta_{\mathbf{m}_1}C)\,\delta\mathbf{m}_2 + \dots \\ \cdots + \mathcal{L}(\delta_{\mathbf{m}_1\mathbf{m}_2}C) - P(\,S,\delta_{\mathbf{m}_1\mathbf{m}_2}G\,) = 0, \end{aligned} \tag{2.96}$$

and the same for the PDE concerning the modeling of the Green's function G, i.e.

$$\nabla_{\mathbf{m}}\mathcal{L}(G)\,\delta\mathbf{m}_1 + \mathcal{L}(\delta_{\mathbf{m}_1}G) = 0. \tag{2.97}$$

$$\begin{aligned} \nabla_{\mathbf{m}}\nabla_{\mathbf{m}}\mathcal{L}(G)\,\delta\mathbf{m}_1\,\delta\mathbf{m}_2 + \nabla_{\mathbf{m}}\mathcal{L}(\delta_{\mathbf{m}_2}G)\,\delta\mathbf{m}_1 + \cdots \\ \cdots + \nabla_{\mathbf{m}}\mathcal{L}(\delta_{\mathbf{m}_1}G)\,\delta\mathbf{m}_2 + \mathcal{L}(\delta_{\mathbf{m}_1\mathbf{m}_2}G) = 0. \end{aligned} \tag{2.98}$$

We first multiply equation (2.96) with the adjoint wavefield $u^\dagger$, apply $\langle . \rangle$ and add it to equation (2.93), which yields

$$\begin{aligned} H_{mm}(\,\delta\mathbf{m}_1, \delta\mathbf{m}_2\,) = \Big\langle & \nabla_C \nabla_C \chi\, \delta_{\mathbf{m}_1} C\, \delta_{\mathbf{m}_2} C + \nabla_C \chi\, \delta_{\mathbf{m}_1\mathbf{m}_2} C \\ & + u^\dagger\, \nabla_{\mathbf{m}} \nabla_{\mathbf{m}} \mathcal{L}(C)\, \delta\mathbf{m}_1\, \delta\mathbf{m}_2 + u^\dagger\, \nabla_{\mathbf{m}} \mathcal{L}(\delta_{\mathbf{m}_2} C)\, \delta\mathbf{m}_1 \\ & + u^\dagger\, \nabla_{\mathbf{m}} \mathcal{L}(\delta_{\mathbf{m}_1} C)\, \delta\mathbf{m}_2 + u^\dagger\, \mathcal{L}(\delta_{\mathbf{m}_1\mathbf{m}_2} C) \\ & - u^\dagger\, P(\,S, \delta_{\mathbf{m}_1\mathbf{m}_2} G\,)\Big\rangle. \end{aligned} \tag{2.99}$$

Invoking again two adjoint operators for terms two and six in equation (2.99), we can eliminate $\delta_{\mathbf{m}_1\mathbf{m}_2} C$ due to the definition of $u^\dagger$ and equation (2.99) simplifies to

$$\begin{aligned} H_{mm}(\,\delta\mathbf{m}_1, \delta\mathbf{m}_2\,) = \Big\langle & \nabla_C \nabla_C \chi\, \delta_{\mathbf{m}_1} C\, \delta_{\mathbf{m}_2} C + u^\dagger\, \nabla_{\mathbf{m}} \nabla_{\mathbf{m}} \mathcal{L}(C)\, \delta\mathbf{m}_1\, \delta\mathbf{m}_2 \\ & + u^\dagger\, \nabla_{\mathbf{m}} \mathcal{L}(\delta_{\mathbf{m}_2} C)\, \delta\mathbf{m}_1 + u^\dagger\, \nabla_{\mathbf{m}} \mathcal{L}(\delta_{\mathbf{m}_1} C)\, \delta\mathbf{m}_2 \\ & - u^\dagger\, P(\,S, \delta_{\mathbf{m}_1\mathbf{m}_2} G\,)\Big\rangle. \end{aligned} \tag{2.100}$$

Repeating the same procedure using equation (2.98) with the adjoint wavefield $c^\dagger$ defined in equation (2.43), we get

$$\begin{aligned} H_{mm}(\,\delta\mathbf{m}_1, \delta\mathbf{m}_2\,) = \Big\langle & \nabla_C \nabla_C \chi\, \delta_{\mathbf{m}_1} C\, \delta_{\mathbf{m}_2} C + u^\dagger\, \nabla_{\mathbf{m}} \nabla_{\mathbf{m}} \mathcal{L}(C)\, \delta\mathbf{m}_1\, \delta\mathbf{m}_2 \\ & + u^\dagger\, \nabla_{\mathbf{m}} \mathcal{L}(\delta_{\mathbf{m}_2} C)\, \delta\mathbf{m}_1 + u^\dagger\, \nabla_{\mathbf{m}} \mathcal{L}(\delta_{\mathbf{m}_1} C)\, \delta\mathbf{m}_2 \\ & - u^\dagger\, P(\,S, \delta_{\mathbf{m}_1\mathbf{m}_2} G\,) + c^\dagger \nabla_{\mathbf{m}} \nabla_{\mathbf{m}} \mathcal{L}(G)\, \delta\mathbf{m}_1\, \delta\mathbf{m}_2 \\ & + c^\dagger \nabla_{\mathbf{m}} \mathcal{L}(\delta_{\mathbf{m}_2} G)\, \delta\mathbf{m}_1 + c^\dagger \nabla_{\mathbf{m}} \mathcal{L}(\delta_{\mathbf{m}_1} G)\, \delta\mathbf{m}_2 \\ & + c^\dagger \mathcal{L}(\delta_{\mathbf{m}_1\mathbf{m}_2} G)\Big\rangle. \end{aligned} \tag{2.101}$$

Defining two adjoint operators for terms five and nine, we get rid of $\delta_{\mathbf{m}_1\mathbf{m}_2} G$, because of the definition of $c^\dagger$ and equation (2.101) changes to

$$\begin{aligned} H_{mm}(\,\delta\mathbf{m}_1, \delta\mathbf{m}_2\,) = \Big\langle & \nabla_C \nabla_C \chi\, \delta_{\mathbf{m}_1} C\, \delta_{\mathbf{m}_2} C + u^\dagger\, \nabla_{\mathbf{m}} \nabla_{\mathbf{m}} \mathcal{L}(C)\, \delta\mathbf{m}_1\, \delta\mathbf{m}_2 \\ & + u^\dagger\, \nabla_{\mathbf{m}} \mathcal{L}(\delta_{\mathbf{m}_2} C)\, \delta\mathbf{m}_1 + u^\dagger\, \nabla_{\mathbf{m}} \mathcal{L}(\delta_{\mathbf{m}_1} C)\, \delta\mathbf{m}_2 \\ & + c^\dagger \nabla_{\mathbf{m}} \nabla_{\mathbf{m}} \mathcal{L}(G)\, \delta\mathbf{m}_1\, \delta\mathbf{m}_2 + c^\dagger \nabla_{\mathbf{m}} \mathcal{L}(\delta_{\mathbf{m}_2} G)\, \delta\mathbf{m}_1 \\ & + c^\dagger \nabla_{\mathbf{m}} \mathcal{L}(\delta_{\mathbf{m}_1} G)\, \delta\mathbf{m}_2\Big\rangle. \end{aligned} \tag{2.102}$$

Until now, we have not made any assumptions on the forward modeling operator $\mathcal{L}$. For simplicity, we consider in the following only operators that are linear in $\mathbf{m}$. Therefore, the two terms in the expression for $H_{mm}(\,\delta\mathbf{m}_1, \delta\mathbf{m}_2\,)$ containing second derivatives of the

operator $\mathcal{L}$ vanish, leading to

$$\begin{aligned} H_{mm}(\,\delta\mathbf{m}_1, \delta\mathbf{m}_2\,) = \Big\langle & \nabla_C \nabla_C \chi\, \delta_{\mathbf{m}_1} C\, \delta_{\mathbf{m}_2} C + u^\dagger\, \nabla_{\mathbf{m}} \mathcal{L}(\delta_{\mathbf{m}_2} C)\, \delta\mathbf{m}_1 \\ & + c^\dagger \nabla_{\mathbf{m}} \mathcal{L}(\delta_{\mathbf{m}_2} G)\, \delta\mathbf{m}_1 + u^\dagger\, \nabla_{\mathbf{m}} \mathcal{L}(\delta_{\mathbf{m}_1} C)\, \delta\mathbf{m}_2 \\ & + c^\dagger \nabla_{\mathbf{m}} \mathcal{L}(\delta_{\mathbf{m}_1} G)\, \delta\mathbf{m}_2 \Big\rangle. \end{aligned} \tag{2.103}$$

For an incorporation and interpretation of non-linear operators, we refer the reader to *Fichtner and Trampert* (2011). The first three terms in equation (2.103) are unpleasant, because the direction $\delta\mathbf{m}_2$ is contained implicitly in terms of $\delta_{\mathbf{m}_2} C$. Trying to change that, we define two adjoint wavefields $p^\dagger$ and $w^\dagger$ by

$$\mathcal{L}^\dagger(p^\dagger) = -\nabla_C \nabla_C \chi^\dagger\, \delta_{\mathbf{m}_1} C - \nabla_{\mathbf{m}} \mathcal{L}^\dagger(u^\dagger)\, \delta\mathbf{m}_1, \tag{2.104}$$

$$\mathcal{L}^\dagger(w^\dagger) = -\nabla_{\mathbf{m}} \mathcal{L}^\dagger(c^\dagger)\, \delta\mathbf{m}_1. \tag{2.105}$$

Applying the principles used above several times, the first three terms in equation (2.103) can be altered in the following way:

$$\begin{aligned} & \Big\langle c^\dagger \nabla_{\mathbf{m}} \mathcal{L}(\delta_{\mathbf{m}_2} G)\, \delta\mathbf{m}_1 + \nabla_C \nabla_C \chi\, \delta_{\mathbf{m}_1} C\, \delta_{\mathbf{m}_2} C + u^\dagger\, \nabla_{\mathbf{m}} \mathcal{L}(\delta_{\mathbf{m}_2} C)\, \delta\mathbf{m}_1 \Big\rangle \\ & \quad = \Big\langle -\delta_{\mathbf{m}_2} G\, \mathcal{L}^\dagger(w^\dagger) - \delta_{\mathbf{m}_2} C\, \mathcal{L}^\dagger(p^\dagger) \Big\rangle \\ & \quad = \Big\langle -w^\dagger \mathcal{L}(\delta_{\mathbf{m}_2} G) - p^\dagger \mathcal{L}(\delta_{\mathbf{m}_2} C) \Big\rangle. \end{aligned} \tag{2.106}$$

Replacing $-w^\dagger \mathcal{L}(\delta_{\mathbf{m}_2} G)$ and $-p^\dagger \mathcal{L}(\delta_{\mathbf{m}_2} C)$ using equations (2.97) and (2.95), respectively, and then adding expression (2.97), multiplied with $z^\dagger$ and $\langle . \rangle$ applied, equation (2.106) changes to

$$\begin{aligned} & \Big\langle -w^\dagger \mathcal{L}(\delta_{\mathbf{m}_2} G) - p^\dagger \mathcal{L}(\delta_{\mathbf{m}_2} C) \Big\rangle \\ & \quad = \Big\langle w^\dagger\, \nabla_{\mathbf{m}} \mathcal{L}(G)\, \delta\mathbf{m}_2 + p^\dagger\, \nabla_{\mathbf{m}} \mathcal{L}(C)\, \delta\mathbf{m}_2 - p^\dagger\, P(\,S, \delta_{\mathbf{m}_2} G\,) \Big\rangle \\ & \quad = \Big\langle w^\dagger \nabla_{\mathbf{m}} \mathcal{L}(G)\, \delta\mathbf{m}_2 + p^\dagger \nabla_{\mathbf{m}} \mathcal{L}(C)\, \delta\mathbf{m}_2 - p^\dagger\, P(\,S, \delta_{\mathbf{m}_2} G\,) \\ & \qquad + z^\dagger\, \nabla_{\mathbf{m}} \mathcal{L}(G)\, \delta\mathbf{m}_2 + z^\dagger\, \mathcal{L}(\delta_{\mathbf{m}_2} G) \Big\rangle. \end{aligned} \tag{2.107}$$

If we now define $z^\dagger$ as the solution to

$$\mathcal{L}^\dagger(z^\dagger) = P^\dagger(\,S, p^\dagger\,), \tag{2.108}$$

we can write down the final expression for $H_{mm}(\,\delta\mathbf{m}_1, \delta\mathbf{m}_2\,)$ as

$$\begin{aligned} H_{mm}(\,\delta\mathbf{m}_1, \delta\mathbf{m}_2\,) = \Big\langle & u^\dagger\, \nabla_{\mathbf{m}} \mathcal{L}(\delta_{\mathbf{m}_1} C)\, \delta\mathbf{m}_2 + c^\dagger\, \nabla_{\mathbf{m}} \mathcal{L}(\delta_{\mathbf{m}_1} G)\, \delta\mathbf{m}_2 \\ & + w^\dagger\, \nabla_{\mathbf{m}} \mathcal{L}(G)\, \delta\mathbf{m}_2 + p^\dagger\, \nabla_{\mathbf{m}} \mathcal{L}(C)\, \delta\mathbf{m}_2 \\ & + z^\dagger\, \nabla_{\mathbf{m}} \mathcal{L}(G)\, \delta\mathbf{m}_2 \Big\rangle. \end{aligned} \tag{2.109}$$

The Hessian operator applied to the model perturbation $\delta\mathbf{m}_1$ is thus given by

$$\begin{aligned} H_{mm}(\,\delta\mathbf{m}_1, \circ\,) = & \Big\langle u^\dagger\, \nabla_{\mathbf{m}} \mathcal{L}(\delta_{\mathbf{m}_1} C)\, \circ \Big\rangle + \Big\langle c^\dagger\, \nabla_{\mathbf{m}} \mathcal{L}(\delta_{\mathbf{m}_1} G)\, \circ \Big\rangle + \Big\langle w^\dagger\, \nabla_{\mathbf{m}} \mathcal{L}(G)\, \circ \Big\rangle \\ & + \Big\langle p^\dagger\, \nabla_{\mathbf{m}} \mathcal{L}(C)\, \circ \Big\rangle + \Big\langle z^\dagger\, \nabla_{\mathbf{m}} \mathcal{L}(G)\, \circ \Big\rangle. \end{aligned} \tag{2.110}$$

The first two terms account for changes in the forward wavefields C and G caused by the perturbation $\delta\mathbf{m}_1$, the last three terms for changes in the adjoint wavefields $u^\dagger$ and $c^\dagger$, caused by scattering and an altered adjoint source time function. The two adjoint wavefields $w^\dagger$ and $z^\dagger$ can be computed simultaneously, since both interact with the Green's function G and the operator $\mathcal{L}$ is linear in its forcing term.

2.3 Discussion[8]

Due to the general formulation of the problem in section 2.1.1 the derivations are equally applicable to time and frequency domain, and various wave propagation physics, without changing notation. The latter includes any type of medium, including 3-D elastic, heterogeneous and attenuating media. We cannot only reproduce specific derivations in the frequency domain (*Hanasoge*, 2014; *Fichtner*, 2014; *Ermert et al.*, 2016), but also derive corresponding expressions in the time domain, well suited for implementation in modern 3-D wave propagation codes, such as the waveform modeling and inversion package Salvus (*Afanasiev et al.*, 2019) or SPECFEM (*Komatitsch and Tromp*, 2002a,b; *Peter et al.*, 2011). While the last point is also addressed by *Tromp et al.* (2010), the derivation of sensitivity kernels for the distribution of noise sources and structure is more compact in our approach. It furthermore renders the extension to second derivatives possible. Since the formulation is based on principles applied in conventional source-receiver full waveform inversion, it provides a foundation for collaboration and supports the re-use of already developed methods and tools.

Beyond that, the theory unifies the earthquake-based two station method and ambient noise correlations, because we do not impose assumptions on the nature of the wavefield source in equation (2.2). Without any processing that mitigates the effect of energetic signals, the sensitivity to Earth structure will be dominated by large earthquakes (*Fichtner et al.*, 2017) and it might be more efficient to apply conventional two station work flows in such cases. Therefore, the unification primarily loosens the requirement in ambient noise tomography to exclude transient signals in order to be closer to the assumption of diffuse wavefields.

In addition, with a function P in equation (2.9) that is not bilinear in $S_{nm}(\mathbf{x})$ and $G_{m,j}(\mathbf{x}, \mathbf{x}_0)$, the same formulation can be applied to problems such as deconvolution (*Snieder and Şafak*, 2006; *Vasconcelos and Snieder*, 2008a,b) and provides as such a possible framework to generalize different approaches in interferometry.

The assumption on uncorrelated noise sources introduced in equation (2.5) facilitates the forward computation of noise correlation functions. It is, however, not crucial for the application of the method. The correlation length is finite and the evaluation of the double integral in equation (2.4) remains feasible. The basic requirement for the theory to be applicable is to get close to the assumption made on the correlation length in space. In a real data application, one possibility to assess the quality of a specific choice might be to

[8] In contrast to the original publication, the theoretical developments are discussed before the synthetic study.

check if the data can be explained to within the observational uncertainties or if a change of the correlation length, maybe in terms of an additional inversion parameter, is required. To the best of the authors' knowledge there is no observation yet about the quantitative correlation length of different noise sources and since we work with seismic wavelengths that are orders of magnitude larger than ocean waves that mostly generate noise, we use the assumption of uncorrelated noise sources until further insight becomes available. It is interesting to point out that a finite correlation length acts as a low-pass filter and its inference based on correlation functions might not be possible and potentially not necessary.[9] Further constraints on the correlation function itself in terms of convergence are not necessary.

The presented theory is only strictly valid for linearly processed data. The goal for suitable processing is therefore inherently different from commonly applied schemes focusing mainly on improving Green's function recovery (*Bensen et al.*, 2007). One possibility is either to follow the approach proposed by *Fichtner et al.* (2017) and to account for non-linear processing or to keep the processing to a minimum and as linear as possible.

2.4 Recipes for forward and inverse runs[10]

We briefly summarize the findings that will be of most interest for future studies and present short recipes for the forward problem and the computation of sensitivity kernels.

2.4.1 Recipe for forward modeling correlation functions

step 1: Simulate the Green's function using source-receiver reciprocity, i.e. with the source at the reference station, and save the wavefield where the power-spectral density is assumed to be non-zero (equation (2.8)).

step 2: Combine the stored Green's function with the noise source distribution according to the right-hand side of equation (2.9).

step 3: Model the correlation wavefield with the result of step 2 as a distributed source and sample the correlation wavefield at any position where another receiver is located (equation (2.9)).

[9] The last argument is not part of the original publication. It is the result of further discussions and represents our current understanding.

[10] This section is not part of the original publication and is added due to its importance for the next chapters.

For the calculation of the sensitivity kernels, the resulting synthetic correlation functions are compared to the observations in terms of specific misfit functionals and the respective adjoint source time functions are evaluated. For the following recipes, we assume that either a source kernel or a structure kernel is computed. Both can be merged with a suitable combination of misfit functions (see chapter 3).

2.4.2 Recipe for the computation of source kernels

step 4: Run an adjoint simulation according to equation (2.24) with the adjoint source time functions computed above and save the adjoint wavefield where the power-spectral density is assumed to be non-zero.

step 5: Assemble the source kernels according to equation (2.27). This can, in principle, be done in the course of step 4.

2.4.3 Recipe for the computation of structure kernels

step 4: Run an adjoint simulation according to equation (2.24) with the adjoint source time functions computed above and save the adjoint wavefield where the power-spectral density is non-zero.
During the simulation the interaction of the adjoint wavefield and the correlation wavefield of step 3 is integrated over time to obtain the first part of the structure kernel.

step 5: Combine the stored adjoint wavefield with the noise source distribution according to the right-hand side of equation (2.43).

step 6: Run a second adjoint simulation with the result of step 5 as distributed source (equation (2.43)).
During the simulation the interaction of the adjoint wavefield and the Green's function of step 1 is integrated over time to obtain the second part of the structure kernel.

During steps 4 and 6 access to the forward wavefields of steps 1 and 3 are required, which is typically done by saving the corresponding wavefields or by checkpointing techniques (*Griewank*, 1992). The structure kernels resulting from step 4 and 6 are summed to obtain the final kernel.

2.5 Conclusions[11]

In the previous sections we extended the theoretical background for full waveform ambient noise inversion that goes beyond Green's function retrieval. It accounts for the distribution of noise sources in space and frequency, operates for any type of medium, including a 3-D elastic, heterogeneous Earth with attenuation and anisotropy, and models the full seismic wave propagation physics. The general formulation of the forward problem of computing correlation functions facilitates the application of adjoint techniques, which enables us to compute first and also second derivatives efficiently.

[11] In contrast to the original publication, the conclusions regarding the theoretical developments are presented before the synthetic study.

Synthetic Study in 2-D 3

With the theoretical developments presented above, we now try to understand the physics of the problem in a numerical model in 2-D and study how structure and heterogeneous noise source distributions express themselves in noise correlation functions in terms of measurable quantities. We then use the 2-D examples in order to find suitable joint inversion schemes and measurements that are likely to be useful in 3-D real-data problems. The feasibility of the developed strategy is demonstrated in a synthetic inversion.
In the following, we use a 2-D finite-difference discretization of the PDE describing membrane waves (equation (2.10)). The correlations are computed in the time domain for a frequency band from 0.02 to 0.2 Hz.

3.1 Misfit study

A key element for the inversion of both noise sources and structure is the design of misfit functionals that decouple the inversion as much as possible and the awareness of quantities that can only be recovered jointly. We therefore start our developments by studying the effect of heterogeneous noise source distributions and of structure on noise correlation functions in terms of four different misfit functionals. The first one is based on the causal/acausal asymmetry of noise correlations, proposed by *Ermert et al.* (2016), for an inference of the distribution of noise sources with the supposition that it is to first order insensitive to unmodeled Earth structure. The asymmetry A is defined by

$$A = \ln \frac{\int_\tau [w_+(t)C(t)]^2 dt}{\int_\tau [w_-(t)C(t)]^2 dt}, \tag{3.1}$$

where $w_+(t)$ and $w_-(t)$ are time windows centered around signals on the positive and negative lag, respectively. The discrepancy between asymmetries of synthetic and observed correlations can be quantified in terms of an L^2-misfit. A closely related measurement, referred to as energy differences E in the following, directly compares the absolute energy

of windowed signals in synthetics and observations and is given by

$$E = \frac{\int_\tau [w(t)C(t)]^2 dt - \int_\tau [w(t)C^o(t)]^2 dt}{\int_\tau [w(t)C^o(t)]^2 dt}, \tag{3.2}$$

where the superscript ^{o} denotes observations. These two misfits are complemented with waveform differences using the L^2-norm and cross-correlation traveltime measurements. Following *Luo and Schuster* (1991) and *Dahlen et al.* (2000), we define the latter as the traveltime shift, where the time domain cross-correlation between a synthetic and an observed signal reaches its global maximum. With the exception of waveform differences, the measurements are, for now, only performed on the surface wave arrival. In this study, the measurement process is kept simplistic and information from other signals should be exploited for an application with real data.

First, we compile a synthetic reference data set for an array of 16 stations for a homogeneous velocity model and a homogeneous distribution of noise sources, and generate random models with varying degrees of complexity following the approach by *Igel and Gudmundsson* (1997). The strength of the anomalies is chosen such that scattering potential remains constant, i.e. size of the anomaly squared times strength. With this scaling the induced traveltime shift of each anomaly is approximately the same independent of the complexity of the medium. The specific choice for the scaling does not alter the conclusion drawn from this study. The array and three velocity models with varying degrees of complexity are shown in figure 3.1. We then perform two sets of experiments:

Series I: Effect of structure
We evaluate the effect of structural perturbations alone by forward modeling correlations for the different velocity models with a homogeneous source distribution and compute the discrepancy to the reference data set in terms of the four misfit functionals. The respective values are shown as red lines in figure 3.2.

Series II: Effect of source
We repeat this procedure with the same velocity models, but now with a Gaussian-shaped source anomaly superimposed on the homogeneous background. The Gaussian anomaly is placed on the left side of the array (see figure 3.1), which mimics a frequent configuration with strong sources near coasts (*Stehly et al.*, 2006; *Yang and Ritzwoller*, 2008; *Tian and Ritzwoller*, 2015).

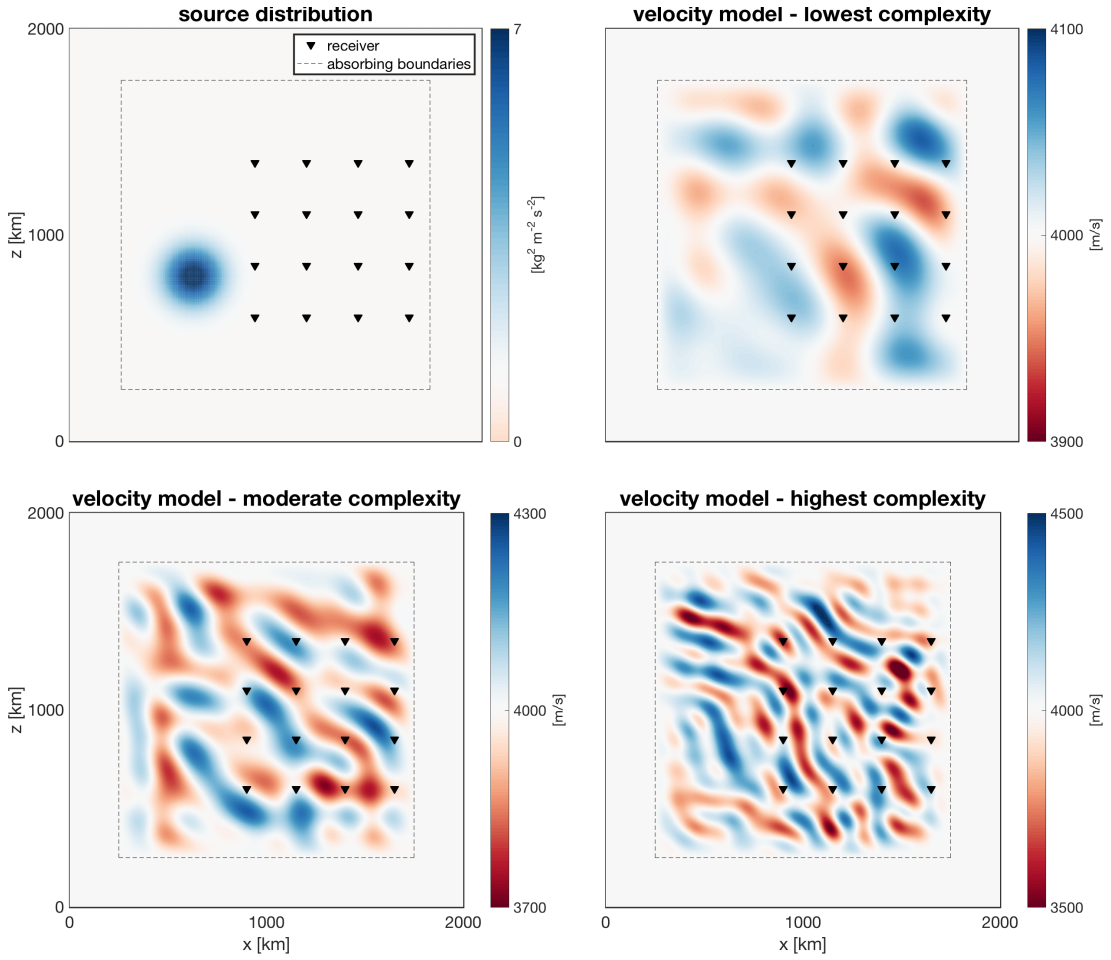

Figure 3.1: Source distribution (top left) and velocity model with lowest (top right), moderate (bottom left) and highest complexity (bottom right) used in the misfit study. Receivers are indicated with black triangles and absorbing boundaries with dashed lines. The source distribution and the model with highest complexity are reused in the inversion example as target model.

The misfit values from this series of models show the combined effect of both noise sources and structure on the measurements and are shown in figure 3.2 as blue line. The difference between misfits caused by structure perturbations only (red lines) and those caused by combined structure and source perturbations (blue lines) provides information on the effect of the heterogeneous noise source.

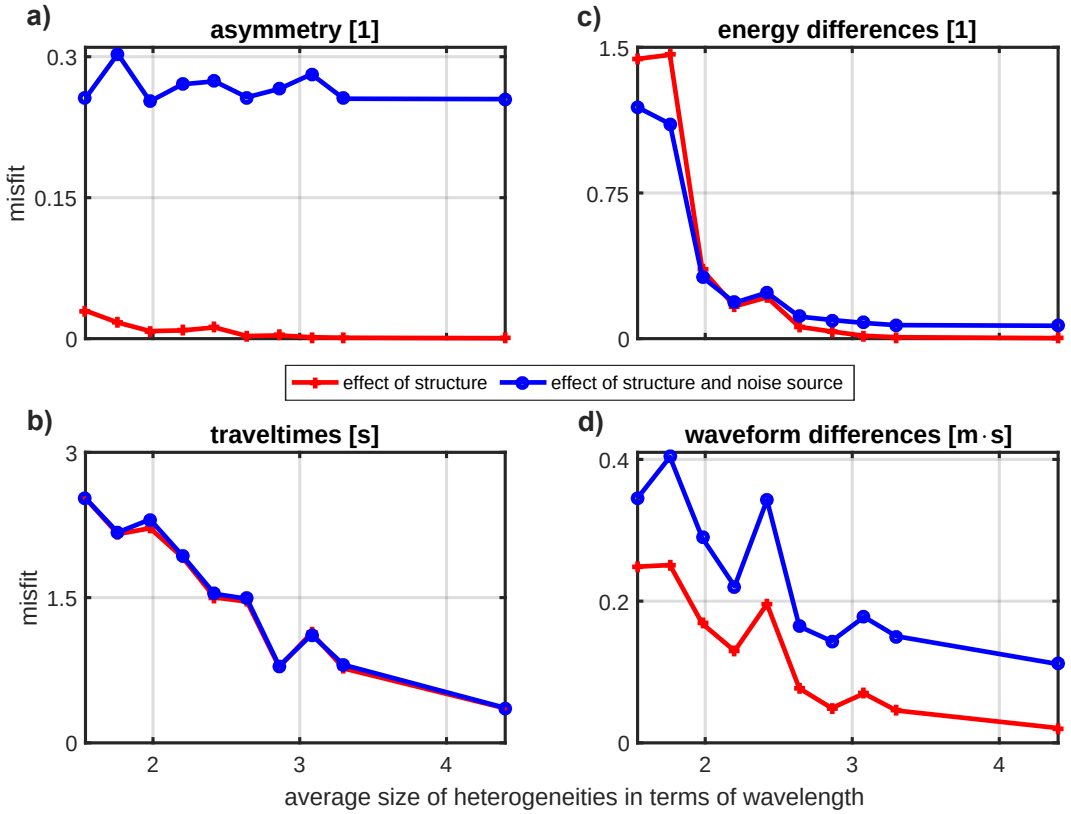

Figure 3.2: Effect of structure (red line) and the combined effect structure and noise sources (blue line) for four different misfit functions: a) asymmetry, b) traveltimes, c) energy differences and d) waveform differences. The misfit values are normalized by the number of recordings and their units are given in the titles. The average size of the anomalies in the velocity models is given in terms of the dominant wavelength.

The asymmetry measurement is mostly affected by the heterogeneous noise source distribution and is insensitive, at least to first order, to Earth structure. We thus confirm the plausibility argument by *Ermert et al.* (2016) that a misfit based on the asymmetry of correlation functions is well suited to study the distribution of noise sources. In contrast, primarily velocity anomalies lead to traveltime differences and, as expected by previous studies (*Tsai*, 2009; *Weaver et al.*, 2009; *Froment et al.*, 2010), the heterogeneous noise source has no profound effect for time-independent tomography. Monitoring applications, which investigate small velocity changes over small time scales, typically use coda waves of correlation functions (*Brenguier et al.*, 2008a,b; *Obermann et al.*, 2013, 2014), aiming at reducing the effect of source variability. In cases where this is not possible, for example due to strong attenuation or the lack of sufficiently strong scatterers, the effect of heterogeneous noise distributions on traveltimes can, however, become significant or even dominant (*Zhan et al.*, 2013; *Delaney et al.*, 2017). The behavior of the energy measurement changes with

the complexity of the structure. For smooth velocity media, the energy of the signal is essentially controlled by the noise source. In strongly heterogeneous media, however, energy is altered through scattering, reflections and focusing effects. These phenomena also lead to more and more complex waveforms, which is expressed by the increase of the misfit based on waveform differences with higher complexity of the velocity model. The shift in magnitude introduced by the source anomaly reflects the resulting amplitude change in the correlation functions.

Inversion strategy

Based on the findings above, we propose the following inversion strategy. Since the influence of heterogeneous noise sources on traveltimes is small, a wave equation traveltime inversion (*Luo and Schuster*, 1991) can be performed first, assuming a homogeneous distribution of noise sources. The resulting model can then be taken as background model for a source inversion based on the asymmetry of noise correlation functions, because this misfit is hardly affected by unmodeled Earth structure. Alternatively, the model inferred from traveltimes serves as initial model for a joint inversion for noise sources and structure using energy and waveform differences. In some cases, a joint inversion is not a straightforward strategy. Updating the source and structure model sequentially is a viable option.[12]

3.2 Inversion example

To explore the potential and limitations of the proposed strategy, we extend the forward solver with an iterative inversion framework that is based on L-BFGS (*Nocedal and Wright*, 2006). In order to deal with the ill-posedness of the inverse problem and to avoid high oscillations in the inverted model, a Tikhonov regularization term (*Tikhonov*, 1963) is added to the misfit function. After running several inversions with different scaling factors for the regularization term, we choose an appropriate value using a pragmatic L-curve approach (*Hansen*, 1992). In addition, we include a Gaussian smoothing operator in the parametrization and choose the dominant wavelength as standard deviation. The inversion is stopped when the norm of the gradient is reduced by a factor of 10^{-3}, which can be achieved with reasonable computational effort and is close to the first-order necessary condition of optimality (*Nocedal and Wright*, 2006).

For the joint inversion of both noise sources and Earth structure, the two misfit functionals, i.e. the energy measurement and waveform differences, are weighted using a convex combination. The weight is chosen based on the magnitude of the individual misfit functions, but no significant changes are observed in the inversion results by varying the relative weight by an order of magnitude. Combining different misfits aims at reducing the null space and

[12] The last point concerning the alternative for a joint inversion was added to include the application to observed data in chapter 6.

at making the misfit functional locally convex, which can lead to a higher convergence rate. In our case, a weight favoring waveform differences does not exploit information about the noise source distribution that energy differences provide, thus the inversion converges slower. To compute synthetic data, we use the heterogeneous noise source distribution and the most complex structure model generated for the misfit study (figure 3.1). The typical size of the heterogeneities is approximately 1.5 times the dominant wavelength. Following the proposed strategy, first traveltimes are exploited by a wave equation traveltime inversion assuming a homogeneous distribution of noise sources. The inversion result is presented in figure 3.3. A smooth representation of the velocity structure is recovered and small scale features are lost. This demonstrates the limitation of traveltime tomography, but also its robustness to retrieve the big picture, even when heterogeneous noise source distributions are ignored.

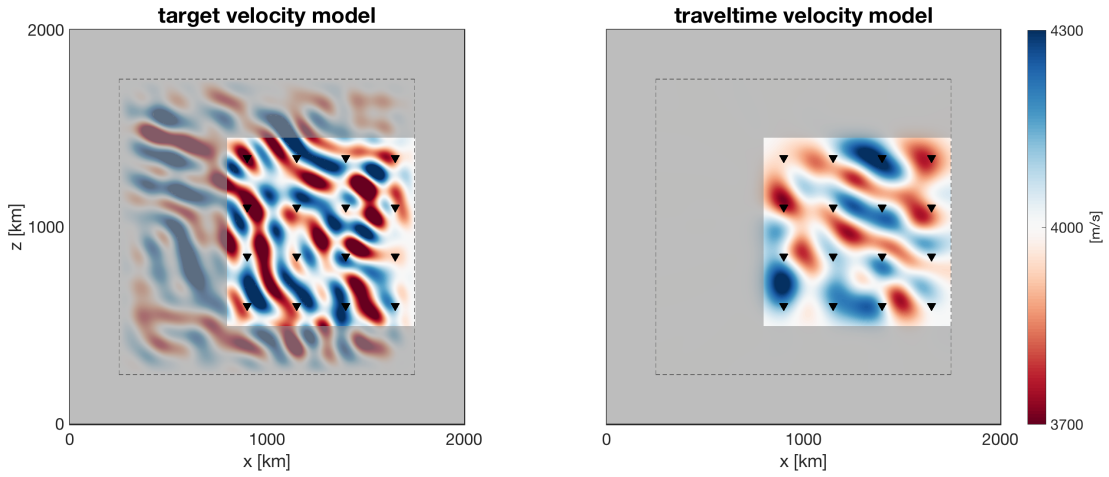

Figure 3.3: Target velocity model (left) and inverted model (right) obtained by a wave equation traveltime tomography with a homogeneous distribution of noise sources. To facilitate their comparison, the velocity models are shaded outside of the array, where low resolution is expected.

Using the velocity model obtained from traveltimes as background model, we invert for the distribution of noise sources based on the asymmetry measurement (figure 3.4). It is possible to locate the strong anomaly on the left side of the array. In regions with only the background noise level, the energy is decreased. By dividing the energy on the causal/acausal branch, the asymmetry of noise correlation functions is not sensitive to the absolute energy level. In our example, the asymmetry can therefore be explained by either introducing a corresponding change in the power-spectral density or with a similar anomaly, but smaller in magnitude and in combination with a reduction of the background noise level.

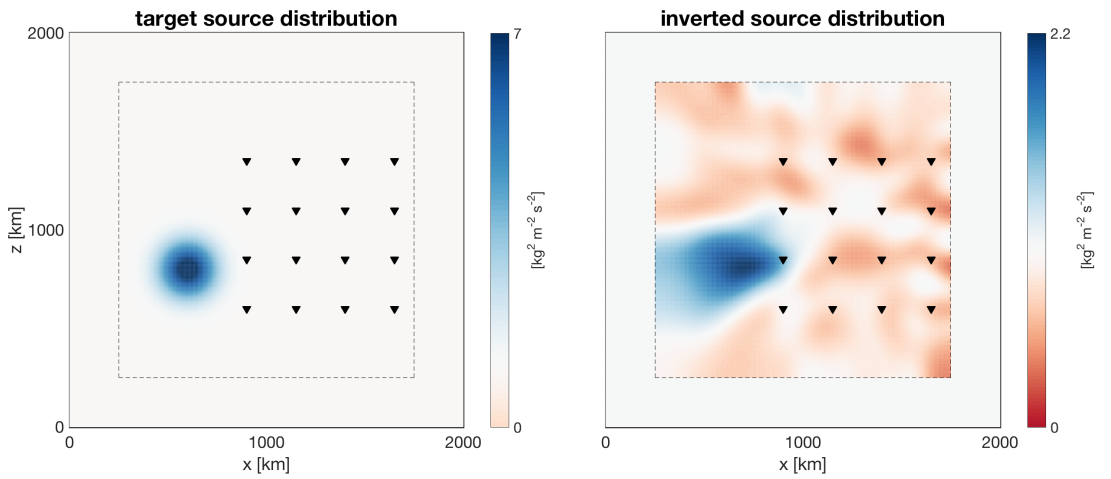

Figure 3.4: Inverted source distribution using the asymmetry of noise correlation functions. The velocity model from the wave equation traveltime inversion is used as a background model.

Instead of only focusing on the source distribution, we finally perform a joint inversion starting with a homogeneous noise source distribution and the velocity model obtained from traveltimes (figure 3.5). As misfit functional we use the proposed combination of energy and waveform differences. Since the source inversion above based on the asymmetry measurement is not sensitive to the absolute energy level and the misfit function for the joint inversion also exploits amplitude information, we do not take the respective source model as initial model and start from a homogeneous distribution of noise sources. Within the array, a high resolution image of the target velocity model is recovered and the noise source anomaly is located accurately.

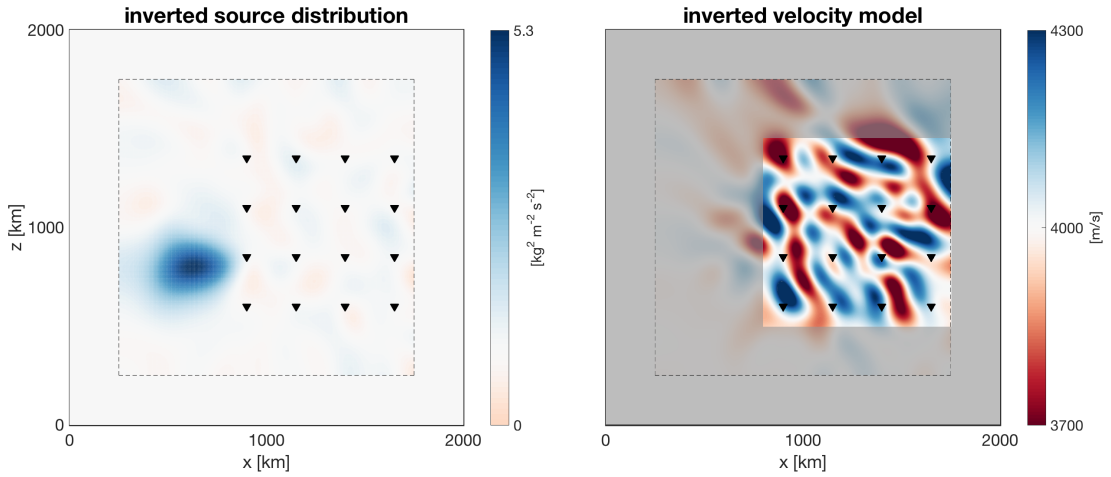

Figure 3.5: Source distribution (left) and velocity model (right) recovered by the joint inversion.

3.3 Trade-offs

3.3.1 Trade-offs and resolution for joint inversion model

In order to assess resolution and trade-offs in the joint inversion, we apply the theoretical developments regarding second derivatives to the model obtained by the joint inversion for the source distribution and velocity model presented above. Introducing a perturbation in the structure model changes the sensitivity to Earth structure. Close to the vicinity of the optimal model, this change in the sensitivity would be the first update in an iterative inversion procedure. It therefore gives a conservative estimate of the resolution in terms of a point spread function, also referred to as spatial intra-parameter trade-off. In figure 3.6, we introduce a scatterer in the velocity model of approximately one third of the dominant wavelength in the center of the array and compute the corresponding Hessian-vector product for the misfit function used in the joint inversion, i.e. the convex combination of waveform and energy differences (right panel in figure 3.6). We infer an approximate width of the point spread function of three times the size of the scatterer, i.e. one dominant wavelength, and a smearing of the perturbation in diagonal direction.

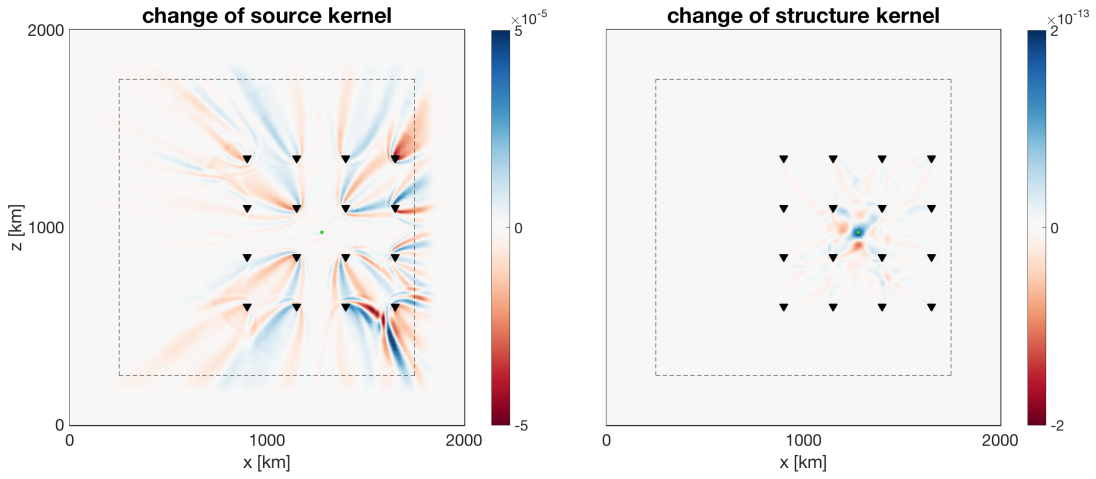

Figure 3.6: Hessian applied to a perturbation in the velocity model. Introducing a perturbation in the velocity model in the center of the array (green dots) changes the source kernel (left) and the structure kernel (right).

At the same time, the perturbation of the velocity model changes the sensitivity to the distribution of noise sources (left panel in figure 3.6). Following the line of arguments above, the change of the source kernel indicates how noise sources can compensate for variations in Earth structure. It is interesting to note that no change in the source distribution is proposed at the location of the scatterer.

3.3.2 Source-structure trade-offs for different measurements

For a further investigation of the trade-offs for the asymmetry measurement and energy differences, we compute Hessian-vector products for both measurements, but now for a perturbation in the source distribution at the center of the array (figure 3.7). Comparing the ratios between the change of the structure kernel and the change of the source kernel is an indicator for the extent of trade-offs. The ratio for the asymmetry measurement is approximately one order of magnitude smaller and thus confirming its capability to better decouple the inverse problem than energy differences.

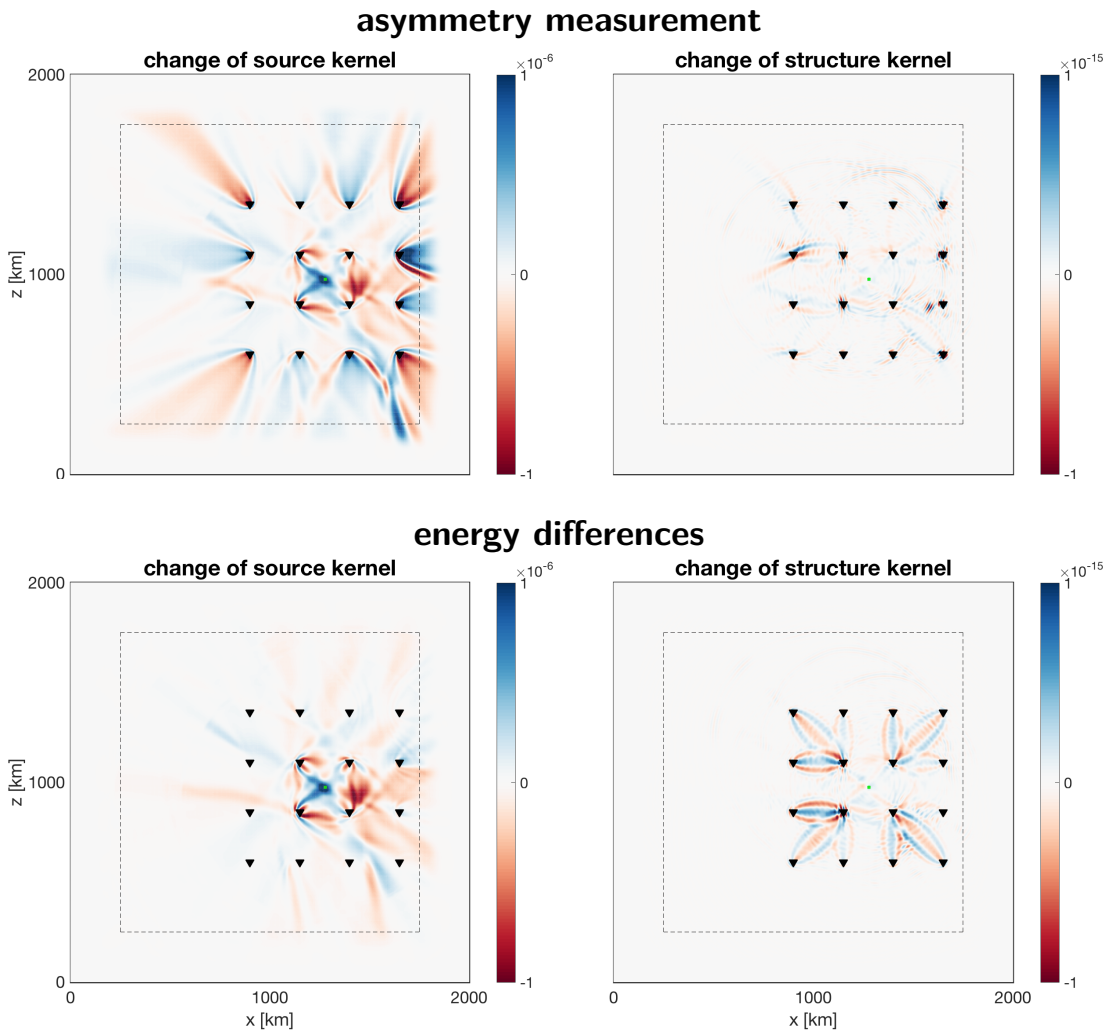

Figure 3.7: Hessian applied to a perturbation in the source distribution (green dots) for the asymmetry measurement (top) and energy differences (bottom). Please note that absolute amplitudes of Hessian-vector products are difficult to interpret.

3.4 Discussion

In the following paragraphs we discuss further details of the developed method, including benefits and limitations, as well as possible directions for further research.

3.4.1 Inversion strategy and example

We estimate the effect of heterogeneous noise sources and structure on four different misfit functionals and then propose an inversion strategy. The misfit study is not meant to be exhaustive and to cover all possible configurations. By the specific choice of the heterogeneous noise source distribution we intend to include the most common configuration with strong noise sources near coasts. To validate the main finding regarding the capability of the asymmetry measurement and energy differences to map noise sources, two related Hessian-vector products are included.

After obtaining a model from a wave equation traveltime inversion assuming a homogeneous distribution of noise sources, further steps depend on the respective target. Either a source inversion can be performed using the asymmetry measurement or a joint inversion based on energy and waveform differences. In the latter, we include amplitude information, which highly depends on the applied processing and whose information content is in general up for debate (*Prieto et al.*, 2011; *Tsai*, 2011). If one is, however, not specifically interested in the absolute energy level of the noise sources, amplitude-based misfit functionals can be used, since relative amplitudes within a carefully processed data set carry information. A possible alternative for the inversion of observed correlation functions is a time- and frequency-dependent phase misfit (*Fichtner et al.*, 2008), which has been applied successfully in conventional source-receiver full waveform inversion (*Fichtner et al.*, 2009, 2013; *Fichtner and Villaseñor*, 2015; *Simutė et al.*, 2016).
In general, an important component of a successful application of full waveform ambient noise inversion is to explore more misfits and possibly develop new measurements. One approach could be to extract "too-early-to-be-physical" arrivals. Under perfect conditions, we would retrieve the Green's function by correlating noise traces and the first arrivals would be governed by the seismic velocity. Since we never fulfill the required assumptions, spurious arrivals are introduced even before the first possible arrivals. These contain valuable information on noise source locations that could improve source inversions. Further research in that direction is needed to assess its potential.

The presented joint inversion example illustrates that it is possible to go beyond traditional noise tomography, which mostly exploits fundamental-mode surface waves. A good inference of the distribution of noise sources is essential, which is analogous to traditional source-receiver methods. We expect that the benefit of full waveform ambient noise inver-

sion will be even larger in 3-D, since higher-mode surface waves are not excited correctly (*Halliday and Curtis*, 2008; *Kimman and Trampert*, 2010), which is necessary for their exploitation in methods that assume a perfect retrieval of the Green's function.

The presented inversion is performed only for one frequency band and we therefore only include one distribution of noise sources. Since noise sources are frequency dependent, a more complete approach would be to allow several distributions in space, for example in terms of L basis functions as presented in the examples above, and invert for them at the same time. The asymmetry measurement and also energy differences, however, do not carry enough frequency information and the same asymmetry or energy can be obtained by changing any basis function. For the application to data, we will for now honor the frequency dependence by inverting for noise sources in subsequent frequency bands. A joint approach is the topic for further research.

3.4.2 Trade-offs

Traditional ambient noise tomography works under the assumption of a homogeneous distribution of noise sources and thereby seemingly avoids the necessity to constrain the noise source distribution and to characterize trade-offs. The concept is simplistic, but to some extent oversimplified, since it fails to describe the physical system where both the distribution of noise sources and Earth structure determine the actual waveforms in correlation functions. The proposed method allows us to jointly invert for the distribution of noise sources and structure. Similar to earthquake tomography, errors in the inference of source properties map into tomographic images of Earth structure (*Valentine and Woodhouse*, 2010). Trade-offs between source and structure can never be avoided completely, but to honor and to be able to interpret results obtained by joint inversion they have to be quantified. Exactly for that purpose, we present a second-order adjoint approach, enabling us to perform a resolution analysis that accounts for intra- and inter-parameter trade-offs. The trade-off kernel in figure 3.6 indicates indeed that a change in the source distribution can compensate for a scatterer introduced in the structure. In the inversion example, this trade-off seems to be manageable, but it is likely to be larger when scattering is dominant. A detailed and quantitative analysis of trade-offs will, however, only be possible with data taking measurement errors into account and is subject for further research. The same concepts can be applied to develop and characterize different misfit functionals aiming at decoupling the inversion as much as possible.

3.4.3 Application to data

For the application of the developed method to observed correlation functions, we extend in chapter 4 the spectral element solver Salvus (*Afanasiev et al.*, 2019), which allows us to compute correlation functions in 3-D media with heterogeneous noise sources at the surface and the corresponding sensitivity kernels for the distribution of noise sources and Earth structure. The first goal is a global inversion for the Hum period band (chapter 6). The application to regional scales poses further challenges, because noise sources and structure outside of the domain of interest affect the correlation functions. Further research is needed to solve this problem.

3.5 Conclusions

The numerical study revealed that the sensitivity of different observables to the distribution of noise sources and to structure varies. Based on that, we designed and implemented an appropriate inversion scheme in order to constrain both of them. The presented joint inversion example demonstrates that full waveform ambient noise inversion has the potential to improve the resolution of tomographic images compared to traditional ambient noise tomography and, in addition, to refine noise source location. An improvement of the latter is essential for a better understanding of noise generation. Inherent trade-offs between source and structure are quantified using Hessian-vector products.

Extension to 3-D 4

The results of the synthetic study in 2-D reveal the potential of full waveform ambient noise inversion. Being aware that the results of a synthetic study cannot prove that a method will work equally well or with similar benefits with real data, the possible improvements with our approach encourage us to continue in this direction and to extend our developments to 3-D. An efficient framework for 3-D media with arbitrary noise source distributions is crucial for the application to observed correlation functions.

4.1 Theory for vector-valued wavefields in the time domain[13]

Before defining what the desired framework is supposed to do, we have to take a closer look at the theory for vector-valued wavefields. The theoretical developments in chapter 2 are for convenience mostly presented for scalar wavefields. We briefly work out the theory for vector-valued wavefields in the following and include specific assumptions made in the subsequent studies. We present it in the time-domain to ensure a close proximity to the final implementation.

4.1.1 Forward theory

The correlation function C_{ij} between the i- and j-components of two seismograms, one recorded at $\mathbf{x}_1$ and the other at $\mathbf{x}_0$, is given by

$$C_{ij}(\mathbf{x}_1, \mathbf{x}_0, t) = \sum_{n,m} \int\limits_{\oplus} \int\limits_{\oplus} G_{i,n}(\mathbf{x}_1, \boldsymbol{\xi}, t) \star G_{j,m}(\mathbf{x}_0, \boldsymbol{\xi}', -t) \star \mathcal{F}^{-1}[S_{nm}(\boldsymbol{\xi}, \boldsymbol{\xi}', \omega)]\, d\boldsymbol{\xi} d\boldsymbol{\xi}', \quad (4.1)$$

where $\star$ and $\oplus$ denote convolution and the volume of the Earth, respectively. The i-component of the Green's function with the source at $\boldsymbol{\xi}$ in n-direction is indicated with $G_{i,n}(\mathbf{x}, \boldsymbol{\xi}, t)$ and $S_{nm}(\boldsymbol{\xi}, \boldsymbol{\xi}', \omega)$ is the power-spectral density distribution of the noise sources. We represent the inverse Fourier transform with $\mathcal{F}^{-1}[\circ]$, which is used to transform $\circ$ to its time-domain equivalent. By averaging C_{ij} over many realizations, which is typically estimated by stacking over many time intervals (*Bensen et al.*, 2007), we assume that

[13] Derivations regarding forward theory and source kernels are borrowed from the publication of chapter 5 and presented in slightly extended form.

neighboring noise sources are temporally uncorrelated in the sense that

$$S_{nm}(\boldsymbol{\xi}, \boldsymbol{\xi}', \omega) = S_{nm}(\boldsymbol{\xi}, \omega)\, \delta(\boldsymbol{\xi} - \boldsymbol{\xi}'). \tag{4.2}$$

We argue that this assumption, which is also invoked for Green's function retrieval, is reasonable for the period band we consider and that the contribution from neighboring noise sources decays relatively quickly with respect to the seismic wavelength. It reduces the computational costs of the forward theory and is as such not necessary for the theoretical developments (see section 2.3 for a detailed discussion). The correlation function in equation (4.1) consequently changes to

$$C_{ij}(\mathbf{x}_1, \mathbf{x}_0, t) = \sum_{n,m} \int\limits_{\oplus} G_{i,n}(\mathbf{x}_1, \boldsymbol{\xi}, t) \star G_{j,m}(\mathbf{x}_0, \boldsymbol{\xi}, -t) \star \mathcal{F}^{-1}[S_{nm}(\boldsymbol{\xi}, \omega)]\, d\boldsymbol{\xi}. \tag{4.3}$$

To reduce complexity, we confine ourselves in the following to the correlation between vertical recordings and assume that the contribution of horizontally acting noise sources and shear traction forces on the vertical component is negligible. In addition, we consider noise sources to be located only in specific parts $\odot \subseteq \oplus$ of the domain, e.g. the surface of the Earth (e.g. *Gualtieri et al.*, 2013; *Ardhuin et al.*, 2015). Equation (4.3) reduces to

$$C_{zz}(\mathbf{x}_1, \mathbf{x}_0, t) = \int\limits_{\odot} G_{z,z}(\mathbf{x}_1, \boldsymbol{\xi}, t) \star G_{z,z}(\mathbf{x}_0, \boldsymbol{\xi}, -t) \star \mathcal{F}^{-1}[S_{zz}(\boldsymbol{\xi}, \omega)]\, d\boldsymbol{\xi}. \tag{4.4}$$

The continuous frequency dependence of $S_{zz}(\boldsymbol{\xi}, \omega)$ cannot be resolved in a realistic inverse problem. We therefore parameterize $S_{zz}(\boldsymbol{\xi}, \omega)$ in terms of L spectral basis functions $s^l(\omega)$ and corresponding distributions in space $\mathcal{S}^l_{zz}$. The forward model is then given by

$$C_{zz}(\mathbf{x}_1, \mathbf{x}_0, t) = \int\limits_{\odot} G_{z,z}(\mathbf{x}_1, \boldsymbol{\xi}, t) \star \Big\{ G_{z,z}(\mathbf{x}_0, \boldsymbol{\xi}, -t) \star \Big[\sum_{l=1}^{L} \mathcal{F}^{-1}[s^l(\omega)] \mathcal{S}^l_{zz}(\boldsymbol{\xi}) \Big] \Big\}\, d\boldsymbol{\xi}. \tag{4.5}$$

Interpreting $\mathbf{x}_1$ as a free space variable, we observe that equation (4.5) has the form of a representation theorem (*Aki and Richards*, 2002). The cross-correlation C_{zz} can be interpreted as a wavefield with $G_{z,z}(\mathbf{x}_0, \boldsymbol{\xi}, -t) \star [\sum_{l=1}^{L} \mathcal{F}^{-1}[s^l(\omega)] \mathcal{S}^l_{zz}(\boldsymbol{\xi})]$ as forcing term, which can be evaluated efficiently using source-receiver reciprocity. For each reference station - in this case $\mathbf{x}_0$ - the corresponding correlation functions are obtained by sampling the correlation wavefield at the respective receivers.

4.1.2 Source kernels

To study the sensitivity with respect to noise sources, we follow the derivations in chapter 2 and derive kernels for the spatial distribution $\mathcal{S}^l_{zz}(\boldsymbol{\xi})$ for the forward problem defined in equation (4.5). A kernel represents the first-order change of a misfit functional and tells us in our case which noise sources have an influence on the measurement. The kernel $K^l(\mathbf{x})$ is given by

$$K^l(\mathbf{x}) = -\int u^\dagger_z(\mathbf{x},t)\left\{\mathcal{F}^{-1}[s^l(\omega)] \star G_{z,z}(\mathbf{x},\mathbf{x}_0,-t)\right\} dt, \tag{4.6}$$

where $u^\dagger_z$ denotes the z-component of the adjoint wavefield (see equation (2.24)). We obtain the adjoint wavefield by injecting the adjoint source time functions, which depend on the specific choice of the measurement, at the receiver locations in the vertical direction. If we consider one receiver at $\mathbf{x}_1$, we can rewrite equation (4.6) and obtain

$$K^l(\mathbf{x}) = -\int \left\{f(t) \star G_{z,z}(\mathbf{x},\mathbf{x}_1,-t)\right\}\left\{\mathcal{F}^{-1}[s^l(\omega)] \star G_{z,z}(\mathbf{x},\mathbf{x}_0,-t)\right\} dt, \tag{4.7}$$

where $f(t)$ is the adjoint source time function. The first Green's function $G_{z,z}(\mathbf{x},\mathbf{x}_1,-t)$ is time-reversed due to the terminal conditions of the adjoint operator (*Tarantola*, 1988; *Tromp et al.*, 2005; *Plessix*, 2006; *Fichtner et al.*, 2006). The kernel is composed of two Green's functions, the first convolved with the adjoint source time function and with its source at $\mathbf{x}_1$ and the second filtered in the period band of the basis function $s^l(\omega)$ and its source at $\mathbf{x}_0$. For an efficient source inversion, *Ermert et al.* (2017) proposed and implemented a scheme that uses a precomputed Green's function database, since only the power-spectral density and the adjoint source time functions in equations (4.4) and (4.6) change during an inversion.

4.1.3 Structure kernels

For the sensitivity to changes in structure, we follow again the developments in chapter 2. The final kernel $K(\mathbf{x})$ can be written as

$$K(\mathbf{x}) = \int \mathbf{u}^\dagger \, \nabla_{\mathbf{m}} \boldsymbol{\mathcal{L}}(\mathbf{C}) + \mathbf{c}^\dagger \, \nabla_{\mathbf{m}} \boldsymbol{\mathcal{L}}(\mathbf{G}) \, dt, \tag{4.8}$$

where $\mathbf{G}$, $\mathbf{C}$ and $\mathbf{u}^\dagger$ denote the Green's function, the correlation wavefield and the adjoint wavefield according to equations (2.8), (2.9) and (2.24), respectively. The adjoint correlation wavefield $\mathbf{c}^\dagger$ is defined by

$$c^\dagger_i(\mathbf{x},t) = \int\limits_{\odot} G_{i,z}(\mathbf{x},\boldsymbol{\xi},-t) \star \left\{u^\dagger_z(\mathbf{x},-t) \star \left[\sum_{l=1}^{L} \mathcal{F}^{-1}[s^l(\omega)]\mathcal{S}^l_{zz}(\boldsymbol{\xi})\right]\right\} d\boldsymbol{\xi}. \tag{4.9}$$

Equations (4.8) and (4.9) closely relate to equations (2.45) and (2.43). For a comprehensive collection of expressions for sensitivities to different parameters for different physics, we refer the reader to chapter 9 in *Fichtner* (2010).

4.2 Requirement list

The final implementation of the theory is by nature just one possible approach out of many. In case someone is interested to implement their own approach, we list in the following the requirements that shaped our framework. In addition, this is intended to help the reader understand specific choices and also the effort spent on certain aspects.

a) Wavefield simulations in 3-D, visco-elastic media.

b) Arbitrary distribution of the power-spectral density $\mathcal{S}_{zz}$ in both space and frequency.

c) Computation of sensitivity kernels with respect to structure and the distribution of ambient noise sources.

d) Convenient work flow for computation of correlation functions and sensitivity kernels due to multi-step forward and inverse runs:

   - 3 steps for forward simulation (see recipe in section 2.4.1).
   - Evaluation of different misfit functionals and calculation of the respective adjoint source time functions.
   - + 2 steps for source kernel (see recipe in section 2.4.2).
   - + 3 steps for structure kernel (see recipe in section 2.4.3).

e) Guarantee of consistency of work flow.

f) Exploitation of efficiencies due to potentially expensive simulations and large wavefield files.

4.3 Implementation

The choice that had the largest imprint on the implementation is the choice of the wave propagation code. Fortunately, this phase of the project fell together with the development of Salvus (*Afanasiev et al.*, 2019). I hereby would like to thank the whole Salvus team who were all involved in one way or another and especially Christian Boehm for his commitment to implement specific features and to adapt the whole inversion framework. I honestly believe that otherwise the following chapters would not have been possible in a remotely comparable way.

4.3.1 Meeting the requirements

a) Wavefield simulations are based on Salvus. We can therefore account for 3-D heterogeneous and attenuating media, as well as for complex domains. Due to this choice, we operate in the time domain.

b) Noise sources are defined as a superposition of different spectral basis functions and their spatial distributions.

c) Structure kernels are based on Salvus. The assembly of source kernels is implemented externally, because they depend on the definition and the choice of the spectral basis functions.

d) SalvusFlow is used to manage and automate the interaction between simulations, preparation of distributed sources, measurements and assembly of source kernels.

e) Test functions are implemented to validate the implementation and to guarantee the consistency of the work flow. Gradient tests, for instance, are run on a routine basis.

f) Efficiencies are exploited on different levels and only some of them are explained in the following:

   - We save the displacements of the Green's functions and the adjoint wavefields in steps 1 and 4 of the recipes in section 2.4 only where the power-spectral densities are assumed to be non-zero. In most of the following cases, the noise sources are assumed to be located on the surface of the domain, which reduces the storage requirements significantly.

   - By default, Salvus saves wavefields at each time step and at each Gauss-Lobatto-Legendre (GLL) point with polynomial order 4. Depending on the specific application and the desired accuracy, the polynomial degree and the time interval can be adapted to reduce storage requirements. During simulations distributed sources are projected back to polynomial order 4 and interpolated linearly between stored time steps, e.g. for step 3 of recipe 2.4.1.

- Inspired by SalvusFlow, simulations and their specific role in the recipe for the forward or the inverse run are stored in a database. This enables us to keep track of the various steps and to reuse existing simulations. The latter is extremely useful for source inversions and mimics partly the approach taken by *Ermert et al.* (2017).
- The lengths of the acausal and the causal branches are treated independently. To accurately capture the relative amplitudes on both branches, a long generating wavefield, i.e. the Green's function of the reference station, is necessary, which translates to a long acausal branch. If it is possible to define a maximum time for the latest measurement window, for instance if the data quality only allows one to perform measurements on the minor-arc surface waves, the simulation time for the causal branch can be cut off accordingly (*Boehm and Fichtner*, 2018). This leads to a significant reduction of the compute time.
- If only one spectral basis function is defined, step 2 in the recipe for the forward problem given by the convolution of the Green's function with the time domain equivalent of the power-spectral density distribution is simplified by defining an appropriate source time function for the simulation of the Green's function. The assembly of the distributed source for the correlation wavefield thus reduces to the time reversal of the wavefield and the multiplication with the power-spectral density distribution. This shortcut also reduces the costs for the composition of the source kernel.

4.3.2 Example for work flow

In order to show what the framework introduced above is capable of, we give a short illustration of a typical scenario in the following. For this purpose, we assume that the power-spectral densities are only non-zero at the surface of the domain.
The computation of correlation functions starts with the generation of the mesh with SalvusMesh, in this case for a global domain for PREM with a minimum resolved period of 100 s. SalvusMesh detects the surface of the domain, which is then used to set up the distributions of noise sources for the spectral basis functions defined by the user. Here we use a Gaussian basis function covering the period band from 100 to 300 s. With these ingredients, we follow the recipe in section 2.4.1 for forward modeling correlation functions. The resulting synthetic correlation functions are compared to the observations and the respective adjoint source time functions are evaluated. Depending on the specific objective, different misfit functionals can be used (see figure 4.1). We then compute a source kernel (see figure 4.2a) and a structure kernel (see figure 4.2b) according to the recipes given in section 2.4.

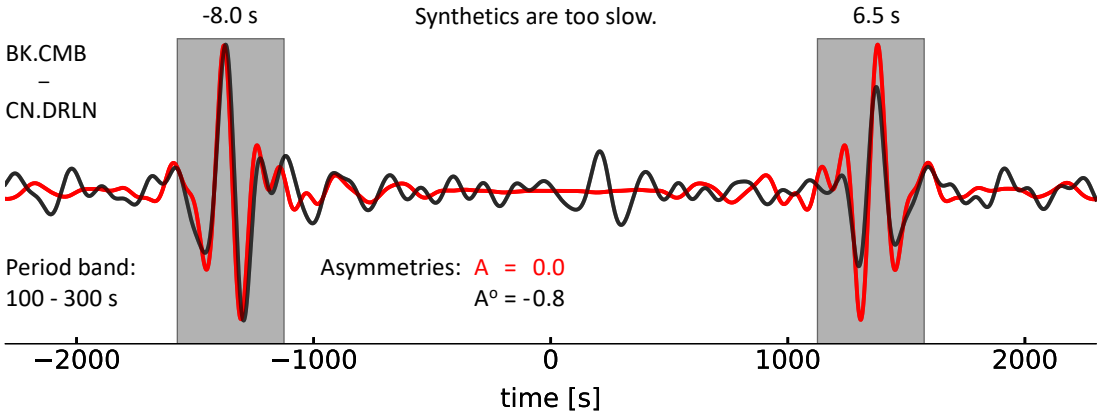

Figure 4.1: Observed (black) and synthetic (red) correlation functions for the station pair BK.CMB - CN.DRLN for the period band between 100 and 300 s. The windows for the surface wave arrivals are sketched with gray boxes. The cross-correlation time shifts reveal that the synthetics are a bit too slow, -8.0 and 6.5 s on the acausal and the causal branch, respectively. Please note the different sign convention for both branches. As expected and quantified by the asymmetry measurement A according to equation (3.1), the synthetic correlation function is symmetric for a homogeneous distribution of noise sources. The observed correlation function, however, is asymmetric indicating stronger noise sources behind station CN.DRLN.

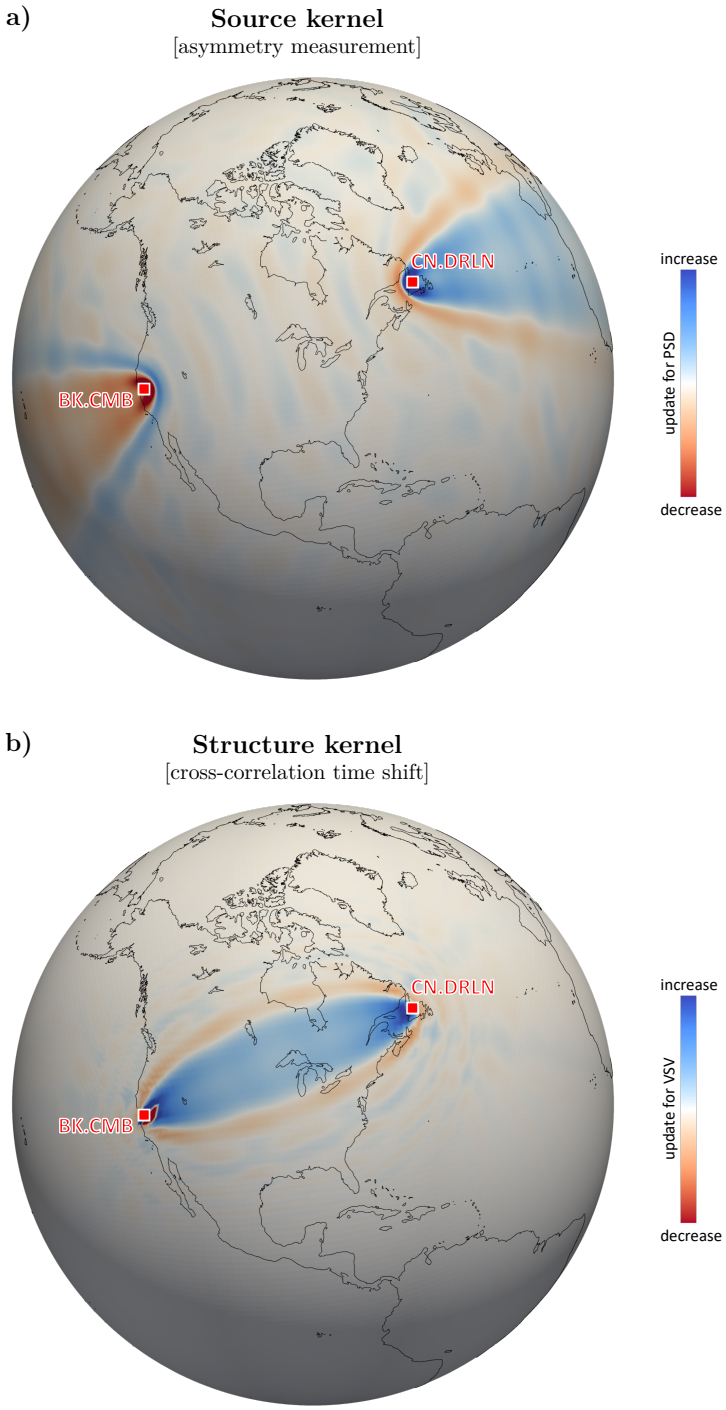

Figure 4.2: Example of a) a source and b) a structure kernel for the station pair BK.CMB - CN.DRLN for the period band between 100 and 300 s. The synthetics computed for PREM with a homogeneous distribution of noise sources and the corresponding observations are shown together with the measurement process in figure 4.1. The source kernel indicates stronger noise sources behind station CN.DRLN and the structure kernel suggests that PREM is too slow on average for the continental craton.

Sensitivity of Seismic Noise Correlation Functions to Global Noise Sources 5

For a first application of the developed framework we study source sensitivity kernels for different time windows. Surface waves in seismic noise correlation functions are routinely exploited for tomographic studies. However, the observation and proper interpretation of body waves is considerably more difficult. To understand body-wave generation in particular and the emergence of noise correlation signals in general, we investigate the sensitivity of correlation functions with respect to global noise sources. Treating noise correlation functions as self-consistent observables, without the enforcement of Green's function retrieval, enables us to investigate the quantitative contribution of different noise sources in space to a signal in a specific time window.

The source sensitivity kernel for a surface wave reveals the expected dominant and broad region of stationary phase, and thereby confirms the robustness of noise tomography in its current state. In contrast, kernels for potential body waves are highly oscillatory and indicate significant contributions from cross-terms, e.g. from body wave - surface wave interactions. While the short-wavelength nature of the body wave kernel may in the future allow us to infer noise sources with great detail, the importance of cross-terms combined with the natural heterogeneity of noise sources renders an interpretation of such an arrival as a pure body wave almost impossible. Furthermore, we show that even long-wavelength Earth structure significantly distorts sensitivity kernels. It is therefore essential to incorporate 3-D heterogeneities into high-resolution imaging of ambient noise sources, especially at higher frequencies.

5.1 Motivation

The evidence that empirical Green's functions can be obtained from the ambient noise field (*Shapiro and Campillo*, 2004; *Sabra et al.*, 2005a) triggered a large number of tomographic studies (e.g. *Shapiro et al.*, 2005; *Sabra et al.*, 2005b; *Nishida et al.*, 2009; *Mordret et al.*, 2015; *Green et al.*, 2017). Their success and the omnipresence of the ambient noise field allow us to increase the illumination in tomographic studies, which was previously dictated by the distribution of earthquakes. The most robust feature in noise correlation functions is the fundamental-mode Rayleigh wave (*Halliday and Curtis*, 2008; *Kimman and Trampert*, 2010). The depth resolution in ambient noise tomography can therefore be relatively poor compared to some forms of earthquake tomography that may use body and higher-mode surface waves. Nonetheless, body waves are present in the ambient noise field (*Schulte-Pelkum et al.*, 2004; *Gerstoft et al.*, 2006, 2008; *Landès et al.*, 2010; *Ruigrok et al.*, 2011; *Gal et al.*, 2015; *Liu et al.*, 2016), and the excitation of secondary microseism P-waves can be modeled following the approaches by *Gualtieri et al.* (2014); *Farra et al.* (2016). Their emergence in correlation functions is also confirmed on local (*Roux et al.*, 2005a; *Draganov et al.*, 2007, 2009; *Ruigrok et al.*, 2011; *Draganov et al.*, 2013; *Panea et al.*, 2014; *Nakata et al.*, 2015; *Olivier et al.*, 2015; *Dantas et al.*, 2018), regional (*Zhan et al.*, 2010; *Poli et al.*, 2012a) and global scales (*Poli et al.*, 2012b; *Nishida*, 2013; *Boué et al.*, 2013; *Haned et al.*, 2016). However, several problems are encountered with their observation and interpretation. Body waves in correlation functions are mostly found under favorable conditions, which cannot be met everywhere on Earth. Due to the difference in geometrical spreading and attenuation compared to surface waves, the probability to detect them is higher in local studies. Otherwise, specific geological settings that support certain seismic phases such as Moho-reflected phases are required (*Zhan et al.*, 2010; *Poli et al.*, 2012a). For long periods (25-100 s) earthquake coda waves contribute to the recovery of deep Earth phases (*Lin and Tsai*, 2013; *Lin et al.*, 2013; *Boué et al.*, 2014; *Poli et al.*, 2017) and pollute the reconstruction from the ambient noise background field (*Boué et al.*, 2014). For a thorough study of body waves, a large dataset and/or careful processing are paramount (*Panea et al.*, 2014; *Nakata et al.*, 2015; *Olivier et al.*, 2015). To the best of the authors' knowledge, only a few studies have exploited body waves retrieved from noise correlation functions for tomographic purposes (*Nakata et al.*, 2015; *Olivier et al.*, 2015) and due to the limitations mentioned above it has not become a standard extension of ambient noise tomography.

The problems with retrieving body waves from ambient noise correlation functions arise because Earth's ambient seismic field does not generally fulfill the conditions needed for Green's function retrieval, which is the theoretical background of ambient noise tomography. The correlation of wavefields that are diffuse and equipartitioned (*Lobkis and Weaver*, 2001; *Weaver and Lobkis*, 2001) or, equivalently, caused by an isotropic distribution of both

mono- and dipolar uncorrelated noise sources (*Wapenaar*, 2004; *Wapenaar and Fokkema*, 2006) are equal to the inter-station Green's function. On Earth, however, the ambient seismic noise field is excited by a heterogeneous and time-variant distribution of noise sources (*Ardhuin et al.*, 2011, 2015). While many applications of ambient noise tomography have been published to date, the attempt to force a correlation function into the corset of a Green's function is a limiting factor, particularly for applications using body waves, higher-mode surface waves, or full waveform inversion.

The goal of this study is to advance our understanding of the generation of signals in a correlation function in general and of body waves in particular. Deciphering the retrieval of body waves in correlation functions is indispensable for their usage in ambient noise tomography, which is necessary to improve its resolution capabilities. We follow the approach by *Tromp et al.* (2010); *Hanasoge* (2013); *Fichtner* (2014); *Fichtner et al.* (2017); *Ermert et al.* (2017) - referred to as full waveform ambient noise inversion - and drop the principle of Green's function retrieval. Considering correlation functions as self-consistent observables enables us to account for the distribution of noise sources, heterogeneous media and the full seismic wave propagation physics. We do not rely on stationary phase analysis, which is typically applied to understand the emergence of signals in Green's function reconstructions (*Snieder*, 2004; *Ruigrok et al.*, 2008).
In the following, we first develop an intuition based on ray-theoretical considerations. We then investigate noise correlation functions without the principle of Green's function retrieval and study their sensitivity with respect to global noise sources. In addition, we examine the effect of 3-D structure, before we discuss possible implications of our findings for ambient noise tomography.

5.2 Ray-theoretical approach: Mapping differential traveltimes

In order to gain a first insight into the generation of signals in noise correlations, we begin with a ray-theoretical approach. Despite the seeming randomness of the ambient seismic field, the physics of wave propagation ensures that coherent arrivals can be extracted. A noise source generates seismic waves that are successively recorded by several stations. Cross-correlation detects the coherent arrivals and thereby reveals the differential traveltime of this ambient signal between the stations (*Wapenaar et al.*, 2010). If, for example, an S-wave arrives at time t_0 at one station and at time t_1 at another station, we obtain the differential traveltime $t_1 - t_0$ through the cross-correlation function, i.e.

$$\int \delta(t' - t_0)\delta(t' - t_1 + t)\, dt' = \delta(t - (t_1 - t_0)). \tag{5.1}$$

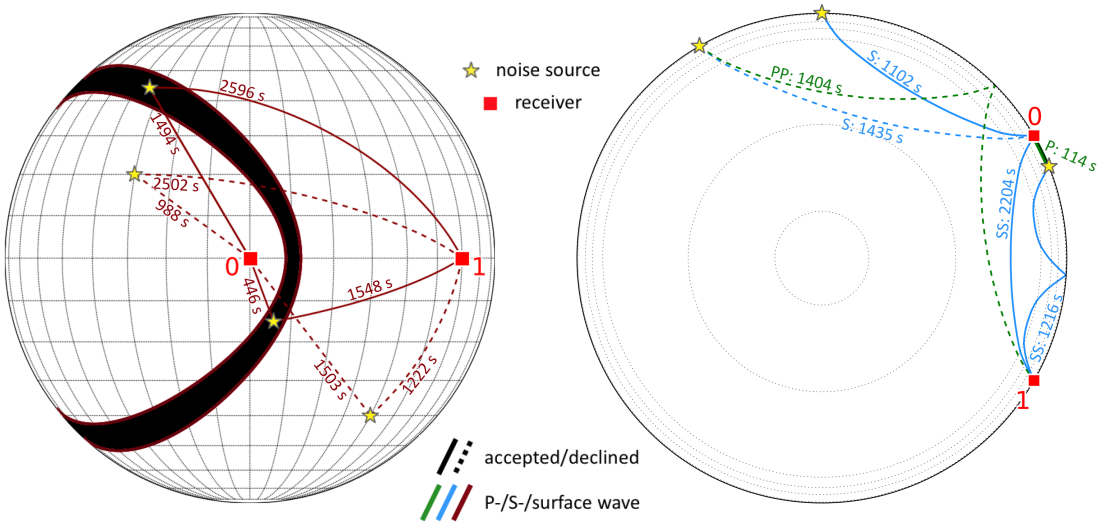

Figure 5.1: For an illustration of the ray-theoretical approach, we trace surface waves (left) and body waves (right) from potential noise source locations (yellow stars) to two stations (red squares), which are 60° apart. Ray pairs that contribute to the defined traveltime of 1,102 s are plotted as solid lines, others as dashed lines. The actual traveltimes are added next to the respective rays. In order to facilitate the generalization of the few examples in the surface wave case, we indicate noise sources that contribute to a time window from 1,000 to 1,200 s in black.

In addition, cross-terms between similar arrivals may occur. The cross-correlation may see an S- and an SS-wave as a coherent arrival. In figure 5.1, we illustrate surface and body waves that contribute to the differential traveltime of 1,102 s for two stations that are located 60° apart on the equator. Body wave traveltimes are computed for PREM (*Dziewoński and Anderson*, 1981) with the TauP module in ObsPy (*Krischer et al.*, 2015) and for surface waves we divide the great circle distance by a constant group velocity of 4 km/s. To map noise sources on the globe that contribute to a specific time window of a correlation function, we avail ourselves of the ray-theoretical approach and go through a regular latitude/longitude-grid for the noise sources and trace rays from each location to the two stations. We make the assumption of spatially uncorrelated noise sources and only include contributions from co-located noise sources (see section 4.1 and equation (4.2)). For simplicity, we only consider minor- and major-arc (R1 and R2) surface waves, S-, SS-, P- and PP-waves. If the differential traveltime of any ray pair, i.e. one ray from the noise source to the first station and another ray from the noise source to the second station, falls within a defined time window, we set the contribution of the noise source to 1, otherwise to 0. Maps showing noise sources that contribute to the signal on the causal branch in a window around the expected surface wave (window from 1,500 to 1,920 s) and in a window around the expected S-wave (window from 1,000 to 1,200 s; expected arrival time in PREM 1,102 s) are presented in figure 5.2. Since we only consider ray traveltimes here, we define

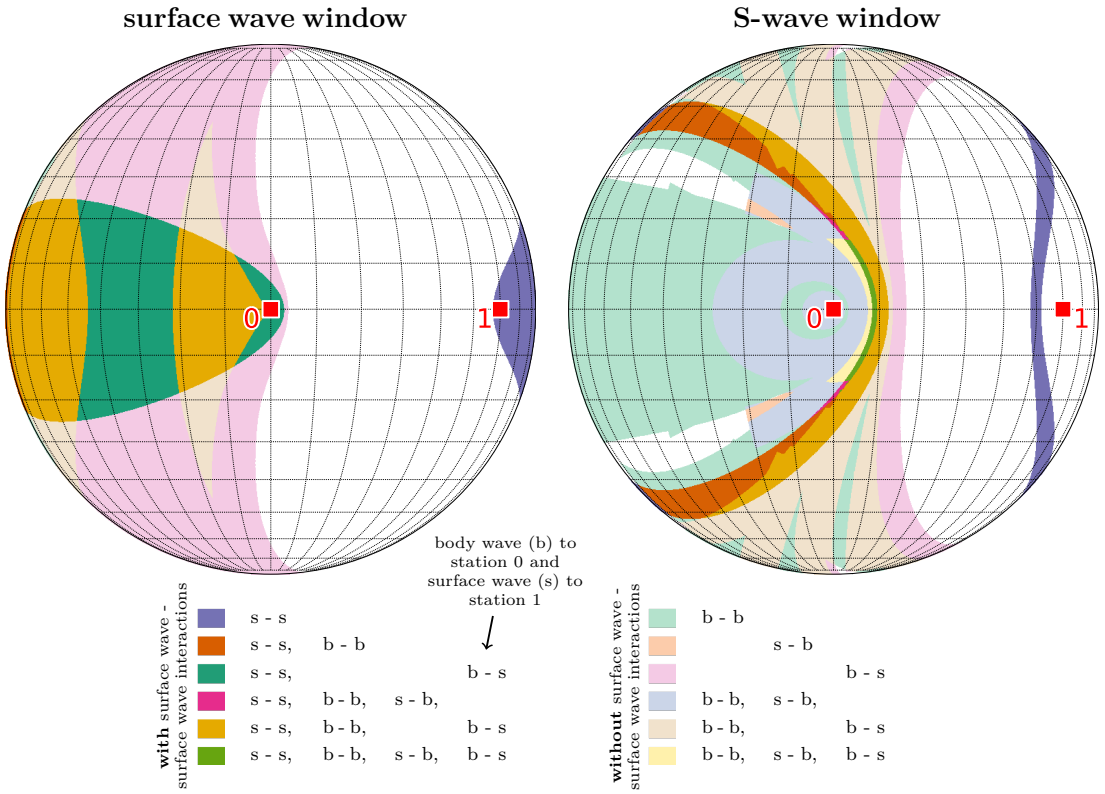

Figure 5.2: Noise sources in the colored regions lead to a signal in the surface wave (left) or in the S-wave (right) window on the causal branch of a correlation function for two stations, which are 60° apart. All possible combinations of different wave types for the displayed longitude-latitude range are color-coded. For instance, the region where both surface wave - surface wave (s - s) interactions and a body wave to station 0 and a surface wave to station 1 (b - s, note that the order is important) contribute to a window is shown in dark green. Strong and pale colors are used to distinguish combinations with and without pure surface wave contributions, respectively. Both stations are plotted as red squares.

the latter window relatively broad to account for the band-limited nature of seismic waves. Figure 5.2 illustrates which noise sources in space contribute to the signal in the surface wave and the S-wave window. They contain features we expect, e.g. the broad region of stationary phase for the surface wave signal or the hyperbola for the S-wave window, both generated by surface wave - surface wave interactions. Cross-terms from different wave types, e.g. surface wave - body wave interactions, are also possible. Their importance is, however, hard to evaluate. It would be tedious and computationally expensive to account for their amplitude behavior, attenuation and polarization, to include more waves types and to incorporate finite-frequency effects. To address these limitations and to refine the maps allowing for a thorough interpretation, we present a full waveform approach in the following.

5.3 Full waveform ambient noise source sensitivities[14]

Interpreting noise correlation functions in terms of Green's functions (e.g. *Lobkis and Weaver*, 2001; *Wapenaar*, 2004; *Sánchez-Sesma and Campillo*, 2006) deceptively renders the distribution of noise sources unimportant. Therefore, in order to study its influence, we regard correlation functions as self-consistent observables.

The forward problem of modeling correlation functions for arbitrary noise source distributions in both space and frequency (equation (4.4)) and the computation of source sensitivity kernels (equation (4.6)) is implemented based on the spectral-element solver Salvus (*Afanasiev et al.*, 2019). Our method is therefore capable of accounting for 3-D heterogeneous and attenuating media, as well as for complex domains, and models the full seismic wave propagation physics. For details on the theory and implementation the reader is referred to chapters 2 and 4.

In the following, we consider noise sources to be located on the surface of the Earth and we only use one spectral basis function, a Gaussian covering the period band from 50 to 100 s. We simulate correlation functions for a homogeneous distribution of noise sources in PREM including attenuation. The corresponding noise correlation functions for receivers along the equator are shown in figure 5.3. The correlation functions are symmetric with respect to lag-time zero and the Rayleigh wave is dominant.

[14]The theoretical developments of the original paper are presented in extended form in chapter 4.

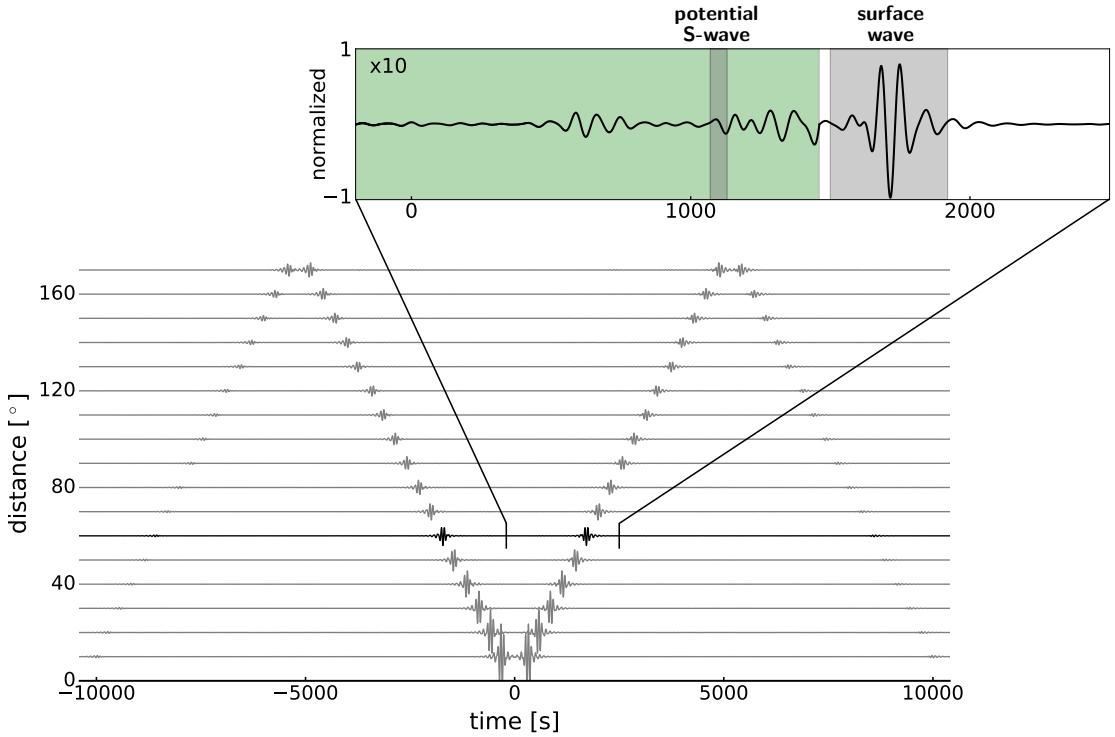

Figure 5.3: Lower panel: correlation functions computed for a homogeneous distribution of noise sources in PREM for a period band of 50 to 100 s. Top panel: zoom-in on the correlation function at 60° distance. The gray boxes indicate the windows defined around the potential S-wave and the surface wave. The window around the former is smaller compared to the ray-theoretical example due to the band-limited nature of the simulations. The part in green is amplified by a factor of 10 to enhance visibility.

We select the correlation function $C_{zz}(\mathbf{x}_1, \mathbf{x}_0, t)$ at 60° distance, once again define two windows, one around the surface wave and the other around the expected S-wave arrival (see figure 5.3), and measure the energy of the windowed signals in terms of

$$E = \frac{1}{2} \int \Big[w(t) C_{zz}(\mathbf{x}_1, \mathbf{x}_0, t) \Big]^2 \, dt, \tag{5.2}$$

where E denotes the signal energy measured in the time window $w(t)$. For the inversion of observed correlation functions, different misfit functionals such as the asymmetry of correlations are more suitable (*Ermert et al.*, 2016, 2017) and their choice is topic of current research. By using the corresponding adjoint source time function, which is

$$f(t) = -w^2(t) C_{zz}(\mathbf{x}_1, \mathbf{x}_0, t) \tag{5.3}$$

(e.g. *Fichtner*, 2010), we ask ourselves, where changes in the noise source distribution decrease the energy in the defined windows. We consequently see all noise sources that

potentially contribute to a specific time window. The kernels are shown in figure 5.4. In addition, we compute sensitivity kernels for the same time windows for a model with Moho topography from Crust 1.0 (*Laske et al.*, 2013) and 3-D perturbations from S20RTS (*Ritsema et al.*, 1999). The latter are added to the S-velocity model and with the scaling proposed by *Ritsema and van Heijst* (2002) also to the P-velocity model. A comparison with the kernels computed for PREM is presented in figure 5.5. Kernels for the expected P-wave arrival are shown in figure 5.6[15].

The sensitivity kernel for the surface wave signal in figure 5.4 reveals a broad and dominant first Fresnel zone behind station 0, which is in this context typically referred to as region of stationary phase (*Snieder*, 2004). R3 surface waves are necessary to explain the sensitivity between both stations. According to figure 5.2, the tails branching off the region of stationary phase are caused by body wave - surface wave interactions. Pure body wave contributions are not visible. The nature of the sensitivity kernel for the potential S-wave is completely different. We do not observe a broad region of stationary phase and the kernel is highly oscillatory. Almost all the features can be explained by the wave types considered in figure 5.2. Even for the window around a potential body wave, the hyperbola from pure surface wave interactions is dominant. We also note a counterpart from multiple orbit surfaces waves closer to station 1. While the main tails branching off the dominant hyperbola are again body wave - surface wave interactions, small contributions from body wave - body wave interactions might be visible in high latitudes. Behind station 0, we observe a combination of pure body wave and surface wave - body wave contributions.
The model with S20RTS and Moho topography (figure 5.5) leads to an asymmetric sensitivity structure for the surface wave signal and shifts the kernel towards North away from the symmetry axis, i.e. the equator in our setup. For the S-wave window, 3-D structure also induces changes in the sensitivity structure and in its amplitude distribution. Major differences are highlighted. The hyperbola from surface wave - surface wave interactions is altered significantly. Some of the oscillations of the kernel are shifted, e.g. behind station 0, and new ones are introduced.

5.4 Discussion

The sensitivity kernels computed for the surface wave signal confirm the robustness of traditional ambient noise tomography. The requirements to obtain a physically meaningful surface wave signal in a noise correlation function are relatively easy to meet due to the broad region of stationary phase, as predicted by *Snieder* (2004) and *Roux et al.* (2005b), and due to negligible contributions from cross-terms.

[15]Figure 5.6 is presented in the supporting information of the original publication.

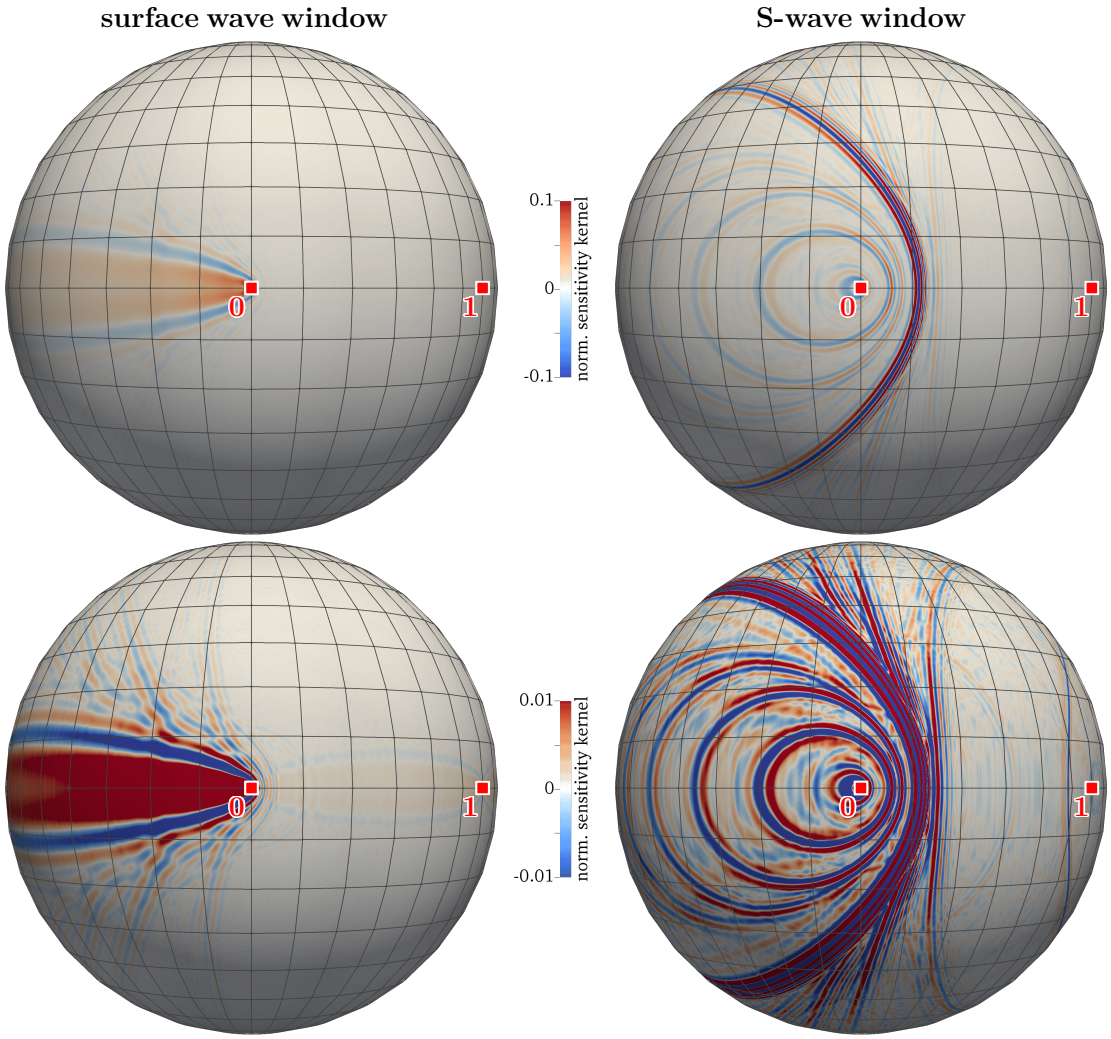

Figure 5.4: Source sensitivity kernels for a window around the surface wave (left) and around the expected S-wave (right). Note that the upper and lower panels show the same normalized kernels, but the color bars are clipped at different values to enhance certain features and to show their relative importance. The maximum absolute value of the surface wave kernel is three orders of magnitude larger compared to the respective value of the body wave kernel. The surface wave window is again from 1,500 to 1,920 s, but the S-wave window is shorter, from 1,070 to 1,130 s (expected arrival time in PREM 1,102.2 s). Both stations are indicated with red squares.

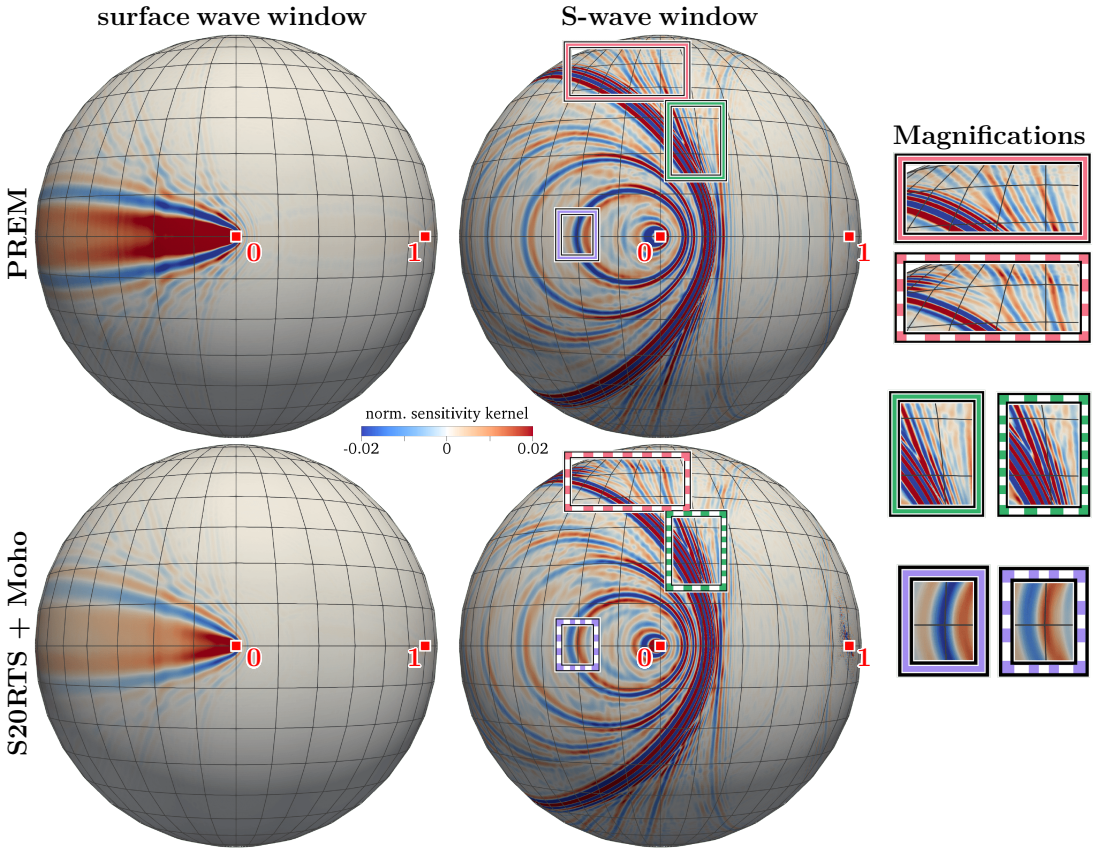

Figure 5.5: Source sensitivity kernels for a window around the surface wave (left) and around the expected S-wave (center) computed for PREM (top) and for S20RTS with Moho topography (bottom). The time windows are defined as before. The symmetry axis for the surface wave kernel is shifted towards North. Major differences for the S-wave window are indicated with boxes and their blow-ups are shown on the right. Both kernels for the surface wave and both kernels for the body wave are normalized with the same values, and the color bar is clipped at 0.02 to enhance certain features. The stations are indicated with red squares.

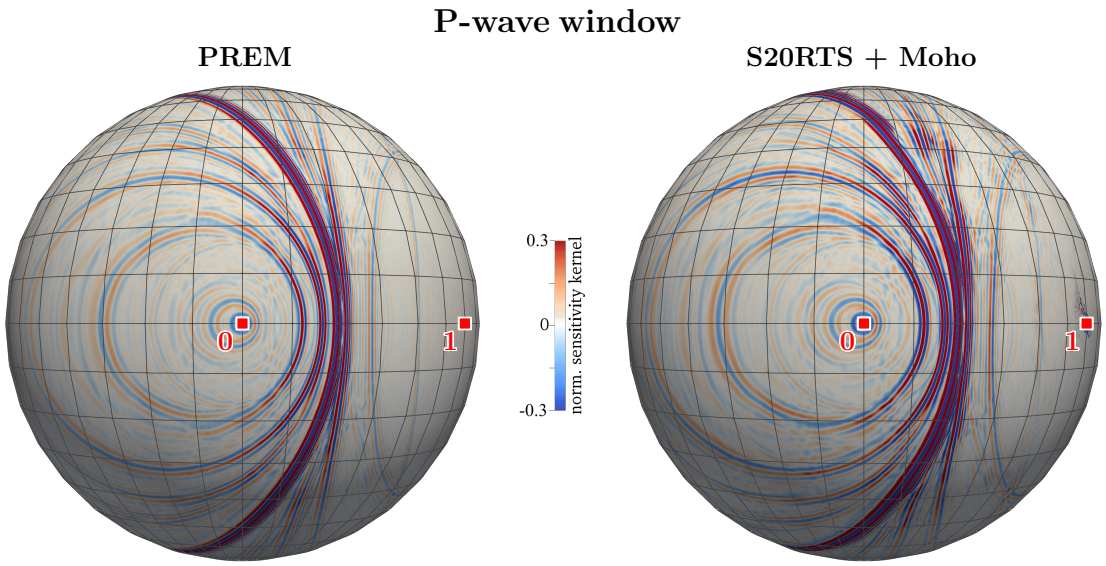

Figure 5.6: Source sensitivity kernel for a window around the expected P-wave (expected arrival time 607.2 s) computed for PREM (left) and S20RTS with Moho topography (right). The window is defined from 580 to 640 s. The kernel is normalized and the color bar is clipped at 0.03 to enhance certain features. Both stations are indicated with red squares.

The kernel for a potential body wave is highly oscillatory and contributions from cross-terms are significant. A spherical harmonic analysis (see figure 5.7) of the noise source kernels in figure 5.4 confirms quantitatively that features up to spherical harmonic degree 10 are between 2 and 4 orders of magnitude smaller. Observed body wave arrivals in cross-correlations are therefore obtained by either strong long-wavelength components of the noise source distribution or by very localized sources. Filtered kernels corresponding to both hypotheses are presented in figure 5.8[16]. Since dominant long-wavelength components in the source distribution would further amplify surface wave signals, we favor the second scenario for the generation of arrivals before the surface wave signal. Potential localized sources are for instance earthquakes (*Lin and Tsai*, 2013; *Lin et al.*, 2013; *Boué et al.*, 2014; *Poli et al.*, 2017), but also ambient noise sources in combination with the ocean source site effect (*Gualtieri et al.*, 2014; *Farra et al.*, 2016; *Retailleau et al.*, 2018).
As described by *Forghani and Snieder* (2010), the confinement of noise sources to the Earth's surface induces an underrepresentation of body waves in correlation functions, which has to be taken into account for an interpretation of correlation functions in terms of Green's function retrieval. However, also considering the significance of cross-terms from different wave types for signals before the surface wave renders this approach extremely difficult, at least for the investigated period band. A physically meaningful body wave can

[16]Figure 5.8 is presented in the supporting information of the original publication.

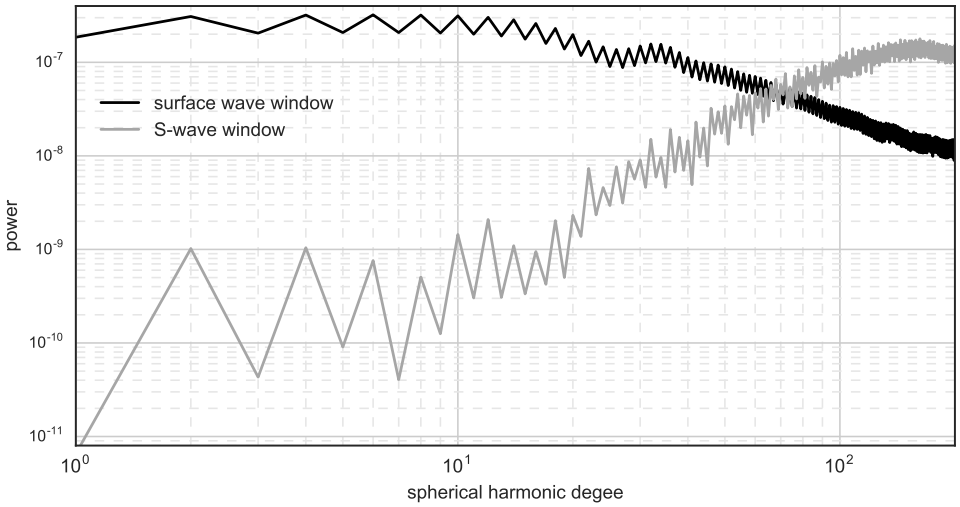

Figure 5.7: Spherical harmonic analysis of the kernel for the surface wave window (black) and the S-wave window (gray) presented in figure 5.4. Both spectra are computed for the normalized kernels. SHTOOLS (*Wieczorek et al.*, 2017) was used for the spectral analysis of the kernels.

only be obtained if the noise sources are in the right location and if the contributions from cross-terms are negligible or cancel out. For a legitimate interpretation of a signal as a body wave, careful analysis and knowledge about the noise source distribution is indispensable.

The interpretation of the results strictly only holds for the studied period band from 50 to 100 s. The partitioning of the ambient noise field in terms of different wave types varies with frequency and surface wave attenuation is often significantly stronger than body wave attenuation (*Coughlin et al.*, 2019). The relative importance of the cross-terms consequently changes and a thorough analysis is necessary. Nevertheless, the physics of the problem remains the same and sources at depth are required for the retrieval of body waves in correlation functions (*Halliday and Curtis*, 2008; *Kimman and Trampert*, 2010).[17]

Even for the relatively long periods considered in this study, the 3-D velocity model composed of S20RTS with Moho topography affects the sensitivity kernels. Note that the perturbations of S20RTS are rather smooth and moderate in magnitude. The observed shift of the fast oscillations of earlier arrivals can lead to erroneous inferences of the power-spectral density distribution. For a high resolution imaging of ambient noise sources, 3-D structure should be taken into account, especially for higher frequencies. This is practically feasible with approaches such as the one by *Ermert et al.* (2017).

[17] This paragraph is not part of the original publication and was added to note that the results might change for different frequencies.

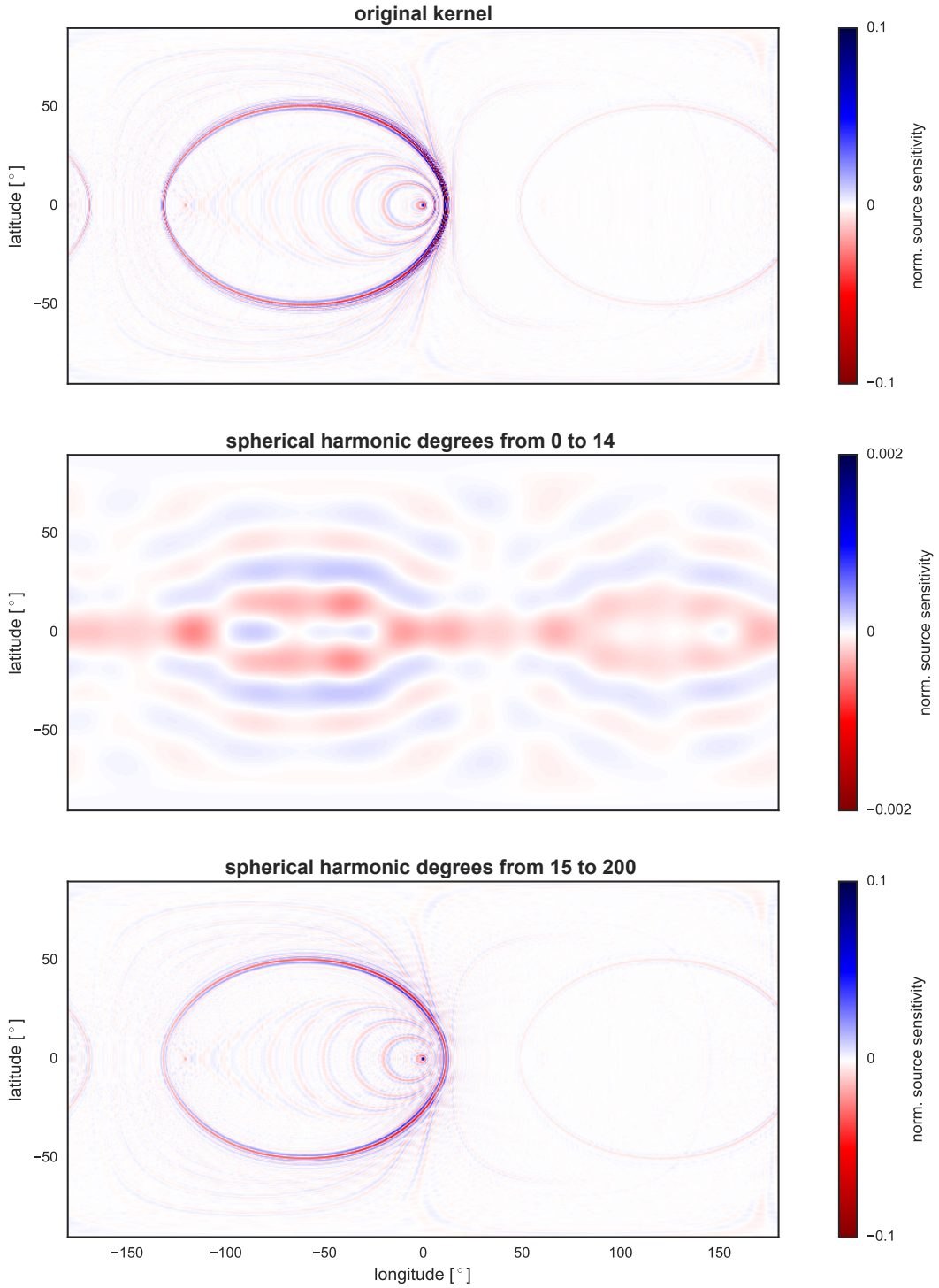

Figure 5.8: The kernel for a potential body wave (top) is filtered from spherical harmonic degrees 0 to 14 (center) and from 15 to 200 (bottom). The long-wavelength component of the kernel is two orders of magnitude smaller and is in agreement with figure 5.7. SHTOOLS (*Wieczorek et al.*, 2017) was used for filtering the kernel.

Full waveform ambient noise inversion addresses the main problems discussed above. It accounts for 3-D heterogeneous and attenuating media and cross-terms are included naturally. The advantage of the latter is that an interpretation in terms of a certain wave type is not necessary. In addition, we can take advantage of the oscillatory nature of the source sensitivity kernels for signals outside the surface wave window in order to improve the resolution of current noise source inversions (*Retailleau et al.*, 2017). The absolute difference in magnitude of the kernels for different windows can be compensated by normalizing the measurements correspondingly.

5.5 Conclusions

Studying the noise source sensitivity of correlation functions reveals that the interpretation of signals in terms of surface and body wave arrivals is fundamentally different for periods longer than 50 s. Due to a broad and dominant region of stationary phase, surface waves in the respective noise correlations are a robust feature. The sensitivity kernel for a potential body wave, however, is highly oscillatory and the contribution from different wave types is significant. The observation of such an arrival is difficult and its identification as a pure body wave is susceptible to misinterpretation. As a consequence, conclusions regarding the partitioning of the ambient noise field in terms of surface waves and body waves are not possible based on their occurrence in correlation functions.[18]
Incorporating the cross-terms as well as 3-D structure is crucial for improving the resolution of ambient noise source inversions, which in turn is a key ingredient for full waveform ambient noise inversion.

[18]The last point was added after a discussion with Daniel C. Bowden.

5.6 Extension to volumetric sources[19]

In the derivations of Green's function retrieval in *Wapenaar* (2004) the receiver pair is surrounded by both mono- and dipolar uncorrelated noise sources on a closed surface. In most configurations, however, noise sources are assumed to be located on the surface of the Earth. As mentioned in the introduction and above, there are various consequences. The most important one in this context is that body waves and higher-mode surface waves are not excited correctly in correlation functions (*Halliday and Curtis*, 2008; *Kimman and Trampert*, 2010). A typical argument to trivialize this problem and to render the consequences of the study above irrelevant is that scatterers act as secondary sources, which in turn leads to a more homogeneous distribution of noise sources (*Hadziioannou et al.*, 2009; *Colombi et al.*, 2014). In order to study this effect, we allow for sources throughout the whole domain. For now, we keep the assumption that only $\mathcal{S}_{zz}$ is non-zero (equation (4.4)). A more comprehensive study in the future should include the remaining components and the current results should be interpreted with caution.

We follow the line of thought from above, model correlation functions and investigate which noise sources in space contribute to a specific window in time. The correlation functions are simulated for a frequency band between 0.2 and 0.8 Hz in a box domain that is 300 km wide in both horizontal directions and 75 km deep (see figure 5.9). Initially, the P and S velocities of the isotropic medium are homogeneous with 5.8 km/s and 4.0 km/s, respectively. The boundaries are absorbing except for the free surface, where the receivers are located at a distance of 50 km from each other.

[19] This section is not part of the original publication and can be seen as a follow-up investigation triggered by further discussions and by reactions to the conclusions drawn above.

The source sensitivity kernel for the window around the surface wave (this time measured on both branches) depicts again a dominant broad region of stationary phase with negligible contributions from cross-terms and from sources at depth (figure 5.9).

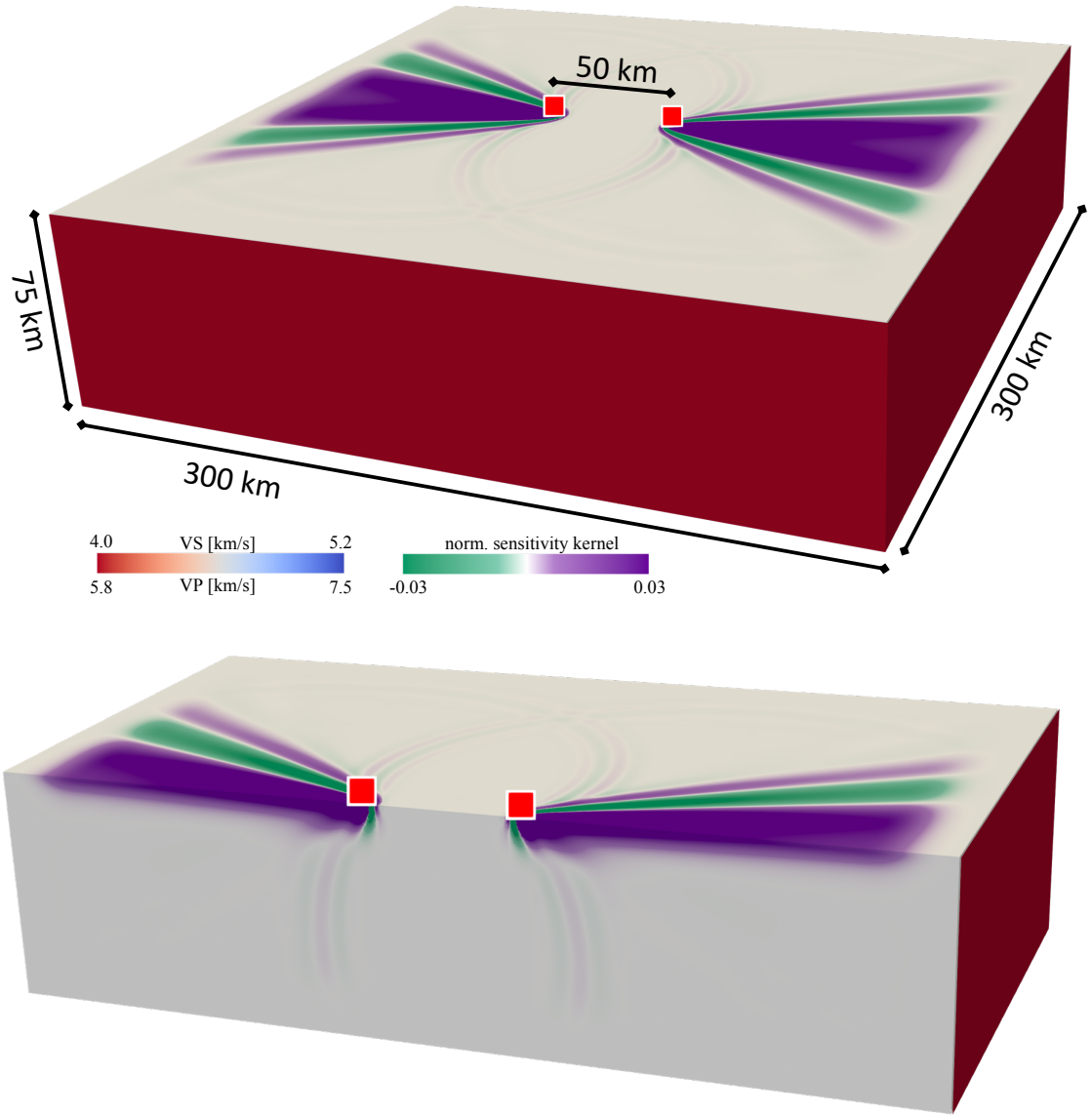

Figure 5.9: Volumetric source sensitivity kernel for the surface wave window. The top figure shows the domain together with the velocity model and the normalized sensitivity kernel at the surface. The effect of the absorbing boundaries can be observed on the sides. The receivers, indicated with red boxes, are located at the surface with a distance of 50 km from each other. Their center point is in the center of the domain. The bottom figure presents a vertical slice through the plane containing both receivers.

For the S-wave window, the source sensitivity kernel (figure 5.10) shows similar features on the surface compared to figure 5.4 and the same interpretation holds. We observe a strong contribution from surface wave - surface wave interactions and energy coming from body waves and interactions between body and surface waves. The vertical slice through the domain additionally reveals significant contributions at depth. For their interpretation we adapt the ray-theoretical approach used above, which confirms that body wave - body wave interactions are expected in this form (figure 5.11).

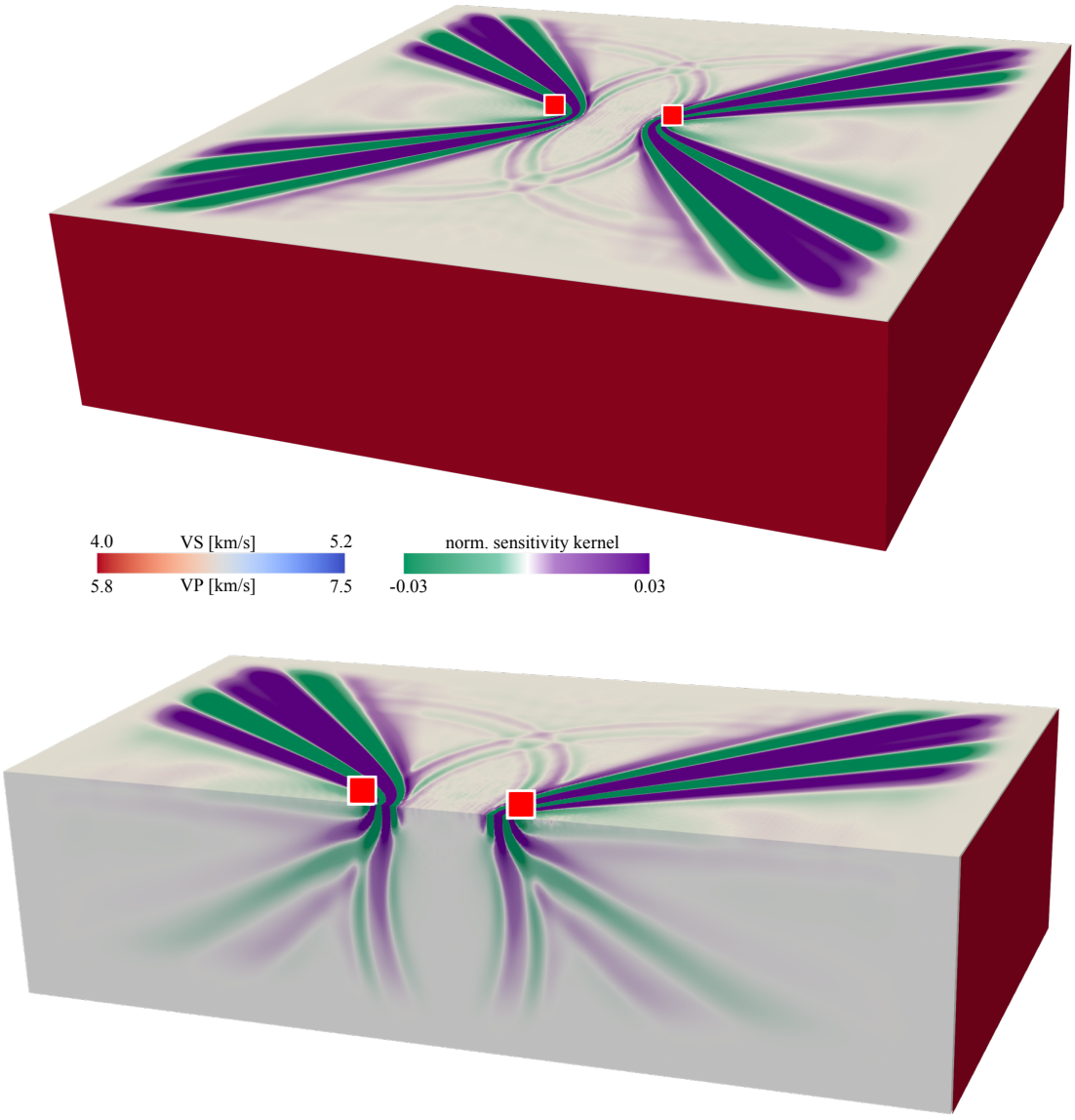

Figure 5.10: Same as figure 5.9, but now for a window defined on the correlation function around the expected S-wave.

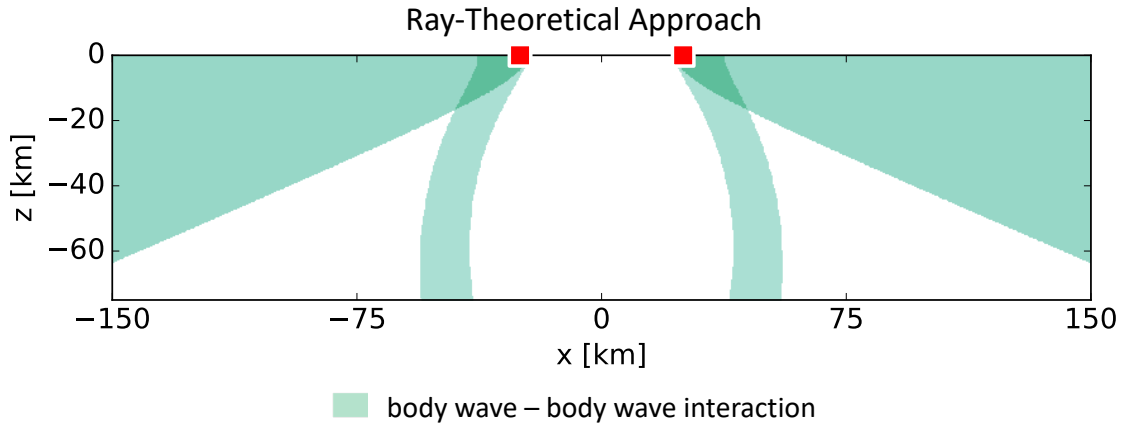

Figure 5.11: Ray-theoretical explanation for the source sensitivity at depth observed in figure 5.10 for the S-wave window. The body wave - body wave interactions are colored in green and the receivers are indicated again with red boxes.

In a homogeneous velocity model, however, the contribution from turning waves is missing. We therefore introduce a velocity gradient in our model and compute again the source sensitivity kernel for the S-wave window (figure 5.12). The hyperbolas behind the stations are then more pronounced and the contribution from turning waves can also be seen in the vertical slice.

The conclusion that we can draw here even with our simplified approach where we only consider $\mathcal{S}_{zz}$ to be non-zero (see equation (4.4)) is that only specific regions at depth contribute to a certain time window and different scatterers might even cancel out due to the oscillatory nature of the sensitivity kernel also at depth. As a consequence, the presence of scatterers throughout the medium might not, by itself, cause enough contributions to explain the presence of body waves.

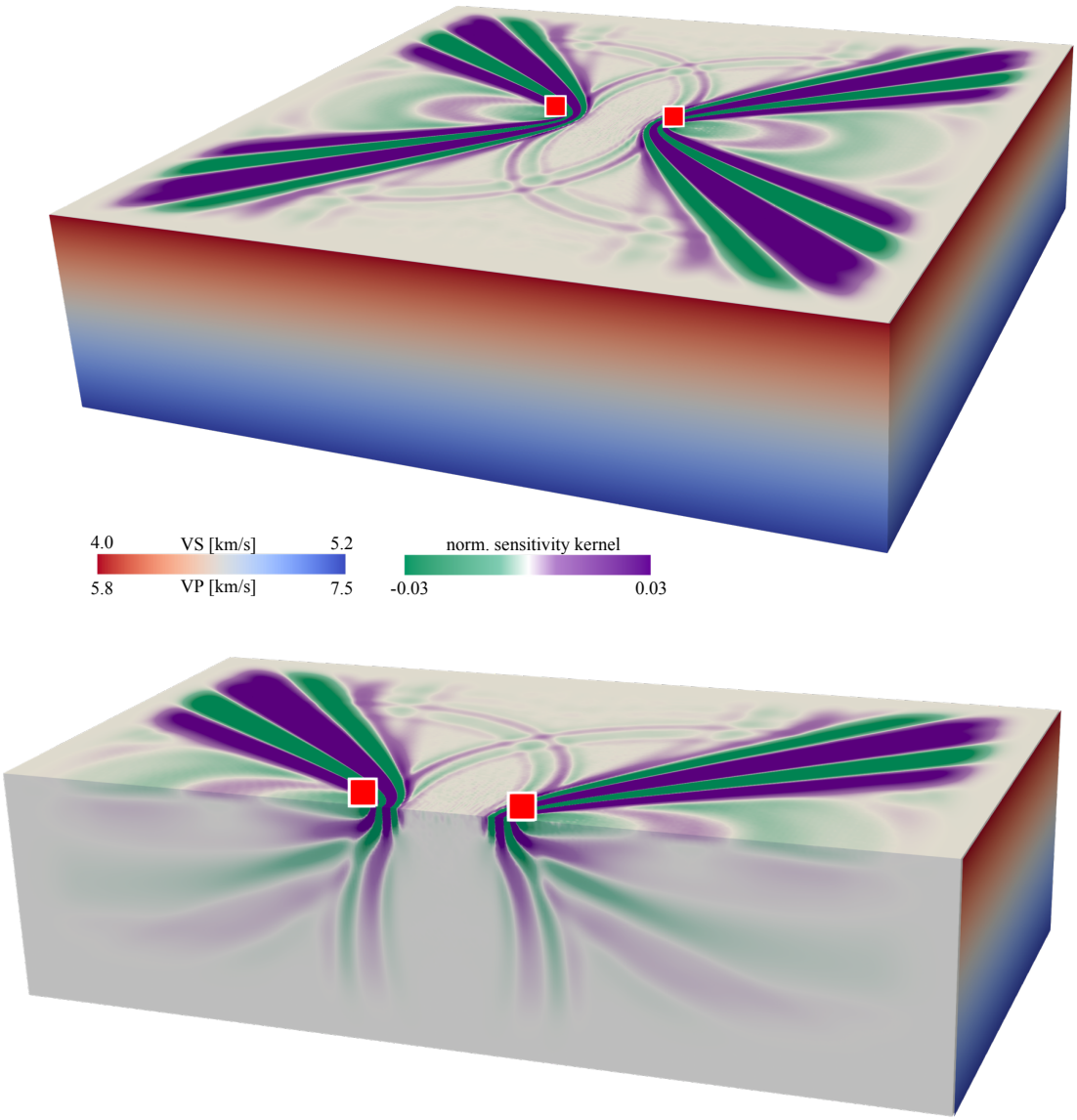

Figure 5.12: Same as figure 5.10, but now with a gradient in the velocity model.

Global-scale Full Waveform Ambient Noise Inversion Applied to Earth's Hum 6

For a first application, we consider a global dataset focusing on the Earth's Hum (*Nishida et al.*, 2000; *Rhie and Romanowicz*, 2006; *Traer and Gerstoft*, 2014; *Ardhuin et al.*, 2015) and invert for the source power-spectral density and for Earth structure. Noise sources can be observed coherently over large distances (*Schulte-Pelkum et al.*, 2004; *Hillers and Ben-Zion*, 2011), which renders full waveform ambient noise inversion an inherently global problem. For the targeted period band between 100 and 300 s, we can afford to simulate correlation functions for a global domain multiple times and circumvent complications for the application to finite domains (see chapter 7 for a detailed discussion). In addition, the Earth's Hum is a suitable candidate for a proof of concept. The long-wavelength structure of the Earth is generally well known and both *Nishida et al.* (2009) and *Haned et al.* (2016) demonstrated that a global tomography is possible with signals emerging in correlations of long period ambient noise recordings. Furthermore, *Ermert et al.* (2016, 2017) investigated its power-spectral density distribution based on the inversion of correlation functions. A thorough validation of the different aspects is thus possible.

6.1 Dataset

We use the dataset prepared by *Ermert et al.* (2016, 2017). Because of the relatively long periods of the Earth's Hum and its low magnitude, only data from STS-1 broadband seismometers were considered. Continuous recordings for 146 stations between 2004 and 2013 were retrieved from the IRIS data management center (ds.iris.edu/mda/_STS-1). Cross-correlations were computed for $\sim$9 h windows and then stacked, where each correlation function was normalized by the energy of both traces to down-weight the contribution of large-amplitude signals. Further non-linear processing steps, typically applied in ambient noise studies (e.g. *Bensen et al.*, 2007; *Schimmel et al.*, 2011), were avoided specifically so the resulting correlations can be interpreted as a solution of the wave equation (*Fichtner et al.*, 2017). In the following, we study the Northern Hemisphere winter, and so all Decembers, Januaries and Februaries of the 10 years were stacked in order to increase the signal-to-noise ratio. The correlations were pre-filtered with a passband between 20 and 500 s. We narrow the frequency content and apply an additional zero-phase filter to focus on

the period band between 100 and 300 s. We argue that the correlations are contaminated by earthquakes for periods smaller than 100 s and a more elaborate processing scheme would be necessary for periods longer than 300 s, e.g. including barometric corrections (*Bormann*, 2012). For a more detailed description of the data compilation and processing, we refer the reader to *Ermert et al.* (2016, 2017).
Ermert et al. (2017, 20xx) estimated the data error by comparing asymmetry measurements from correlations between quasi co-located stations of the Canadian Yellowknife array and all other stations. The maximum distance between the stations of the array is 10 km and consequently much less than the seismic wavelength used in this study, which is on the order of 1000 km. The correlation between individual recordings of the array and a common reference station should yield similar values for the asymmetry. Differences are expected due to instrumental noise and site-specific effects. For the considered period band, the data variance is relatively high and we estimate that the misfit should only be reduced by ∼30 percent. In contrast, phase measurements seem relatively stable (figure 2 in *Ermert et al.* (2017)) and the variance is smaller than the misfit residual expected for the final model.

6.2 Inversion setup

The inversion is based on limited-memory BFGS (L-BFGS) (*Nocedal and Wright*, 2006) and we apply a diffusion-based smoothing operator to the gradients, where the smoothing length is based on the dominant wavelength. We enforce power-spectral densities larger than zero and stop the source inversion once the misfit reaches the level of the estimated error of the asymmetry measurement.

Even though we only consider relatively long periods, the simulations are rather expensive. To accurately capture the symmetry of the correlation functions, we require a generating wavefield, i.e. an acausal branch of ∼6 h. We thus reduce the computational costs with the following measures: (i) Since the data quality only allows us to make measurements on the minor-arc surface wave, we limit the causal branch to 7,000 s. (ii) We approximate the power-spectral density distribution for the period band between 100 and 300 s with one Gaussian spectral basis function and one corresponding spatial distribution. The Green's function in step 1 of the recipe in section 2.4.1 is thus already modeled for the appropriate frequency range, which simplifies the convolution in step 2 and the assembly of the source kernel significantly. (iii) Only 50 receivers act as reference stations, typically referred to as virtual sources (figure 6.1), while trying to ensure a good coverage. This selection is only possible with the new formulation of the theory in chapter 2, which does not require simulations for all reference stations for a full evaluation of the gradient. (iv) The computational domain is reduced to a spherical shell with 1,000 km depth, which is possible

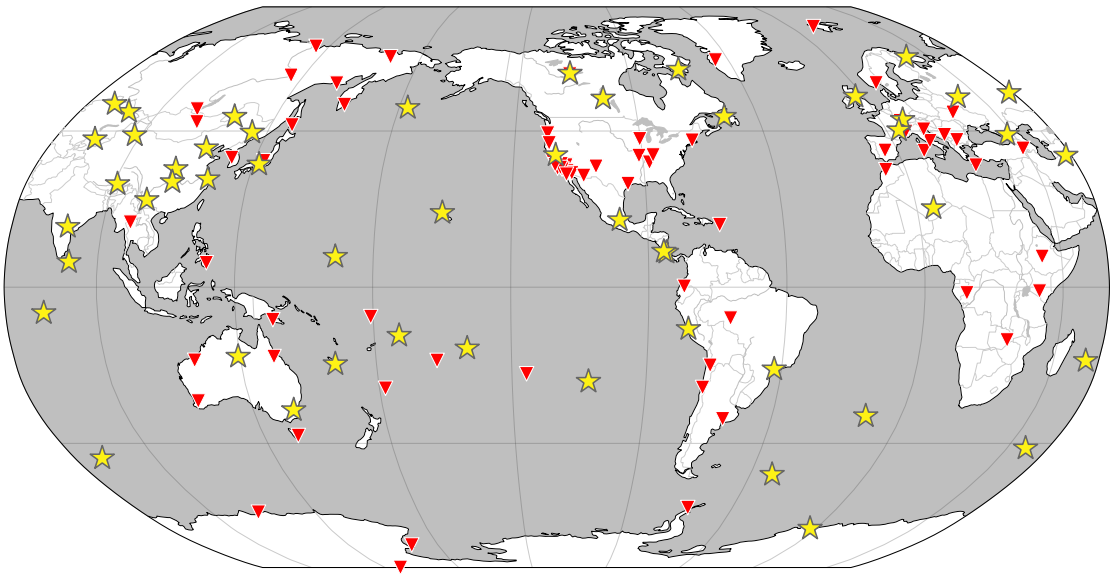

Figure 6.1: Distribution of STS-1 stations used in the inversion. Both red triangles and yellow stars indicate receivers. The latter also denotes their transformation to virtual sources.

because the correlations are dominated by fundamental surface waves. For a maximum period of 300 s, they are hardly sensitive to structure deeper than 700 km (*Boschi et al.*, 2009). We do not observe changes in the correlation waveforms by increasing the depth of the spherical shell.

The source inversion is based on the asymmetry of the correlation functions (equation (3.1)) and for the structure inversion cross-correlation time shifts (*Luo and Schuster*, 1991; *Dahlen et al.*, 2000) are measured on the surface wave packages on the causal and the acausal branches. Due to the relatively high level of incoherent noise, we apply different quality criteria to ensure extraction of meaningful information. We only consider correlation functions with a minimum number of 200 stacked windows. For the asymmetry calculation, we require a signal-to-noise ratio of 2 on either the causal or the acausal branch. Time shifts larger than half a dominant period are rejected and we demand a cross-correlation coefficient of at least 0.6 between the windowed synthetics and observations. The windows for the source and structure inversions are 1,200 s wide and centered on the arrival of a Rayleigh wave with a group velocity of 3,700 m/s. Measurements with overlapping windows are discarded. *Ermert et al.* (2017) applied a similar strategy for the definition of the windows and reported satisfactory results for this simplistic approach.

Considering all the different quality criteria, we measure the asymmetry of 2,732 correlations and 1,658 time shifts. The number of the latter fluctuates on the order of tens in the course of the inversion. In 415 cases, traveltime information can be extracted on both the causal and the acausal branch of the same correlation function. Since the distribution of ambient noise

sources is not homogeneous, differences in both time shifts are expected. The asymmetry in time contains valuable information on the noise source distribution and its usage is currently under investigation (see section 7.3).
In order to estimate the potential resolution of the final models, we plot the ray density for both the source and the structure inversions in figures 6.2 and 6.3, where we account for the respective quality control. Although finite-frequency effects exploited in full waveform ambient noise inversion are neglected, ray coverage provides a useful proxy.
The approach in figure 6.2 is inspired by the ray-based source imaging method introduced by *Ermert et al.* (2016). Since the source sensitivity for the asymmetry measurement is mostly located behind both stations (see figure 4.2a), we plot rays along the great-circle major arc starting from each receiver. To imitate attenuation, we restrict the length of the rays to 10,000 km. Figure 6.2 reveals a relatively good coverage in general. The concentration of stations on the continents of the Northern Hemisphere leads to two broad bands of rays connecting Europe - South America - South Pacific - Asia - Europe and South America - North America - Asia - Indian/Atlantic Ocean - South America. The center of the Pacific Ocean and the southern part of the Atlantic Ocean are covered less, but still show a significant crossing of rays.
For the ray density plot for the structure inversion in figure 6.3, the station pairs are connected by rays on the great-circle minor arc, which mimics the sensitivity to structure (see figure 4.2a). The resulting coverage is significantly different with a higher density on the Northern Hemisphere, especially on the continents, compared to the Southern Hemisphere. We will thus mostly focus on the Northern Hemisphere for the interpretation of the final velocity model. An interesting feature worth pointing out is that we get a relatively good coverage in North Asia, a region normally problematic in tomographic studies due to the lack of earthquakes.

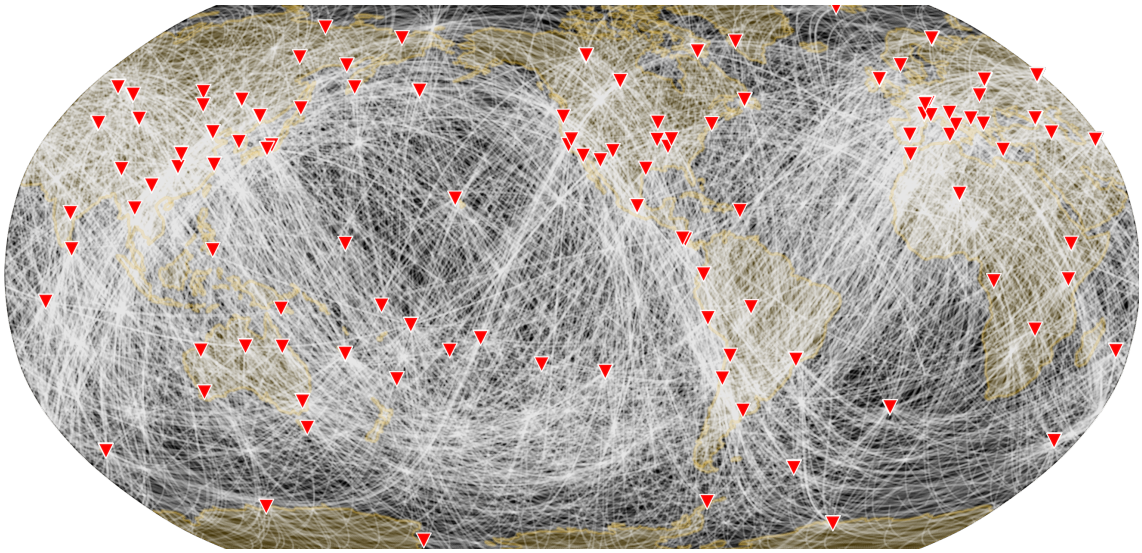

Figure 6.2: Ray density plot for the inversion of the distribution of ambient noise sources. The rays are approximated as lines along the great-circle major arc starting from both receivers (red triangles) and with a length of 10,000 km. The data selection based on the criteria described in the text is accounted for in this plot.

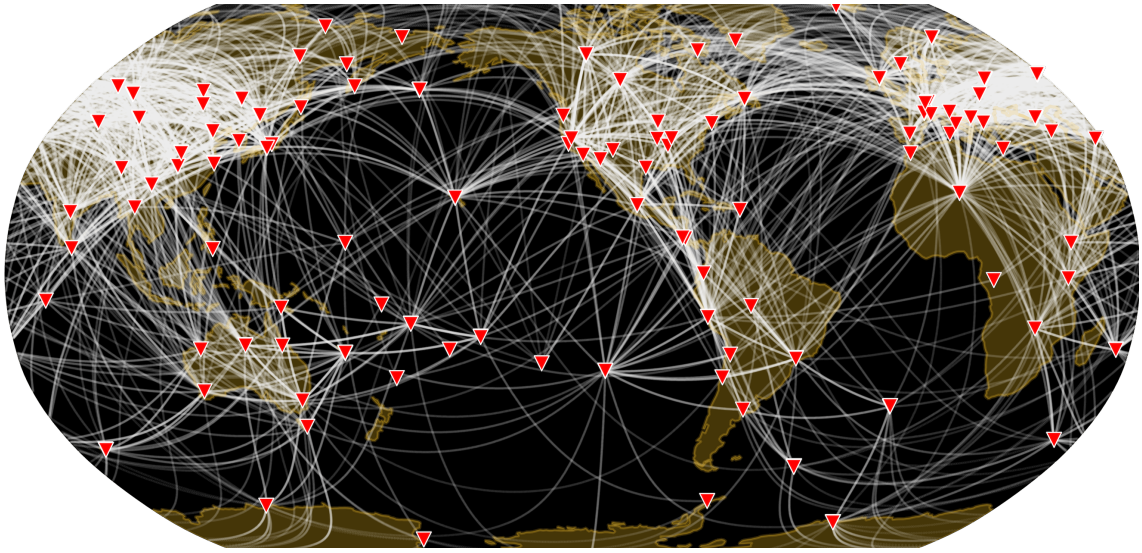

Figure 6.3: Ray density plot for the structure inversion. In contrast to figure 6.2, the rays connect both stations along the great-circle minor arc in order to mimic the sensitivity to structure. The data selection based on the criteria described in the text is accounted for in this plot. The intensity gives an indication of the coverage of a specific region.

6.3 Proof of concept

For a proof of concept, we start with a model that is as unbiased as possible. The initial model is thus composed of a homogeneous distribution of noise sources on the Earth's surface and PREM, including anisotropy and attenuation (*Dziewoński and Anderson*, 1981). We remove the layer at 15 km depth for computational efficiency and extend the first layer to the next discontinuity at 24.4 km depth.
Although feasible in principle and also employed in the synthetic study in chapter 3, we do not perform a joint inversion, but update the source and the structure model in sequences. Finding an appropriate weighting necessary for a joint inversion is not straightforward, in general, and especially not in this study due to the high computational costs. The approach taken here seems, however, reasonable, since the asymmetry is to first order insensitive to unmodeled Earth structure and the traveltime bias due to sources is considered to be small (*Tsai*, 2009; *Weaver et al.*, 2009; *Yao and van der Hilst*, 2009; *Froment et al.*, 2010). In total, we perform 6 iterations for the distribution of the ambient noise sources and 8 iterations for structure. The order of the different updates is at this stage of the developments arbitrary and is chosen such that we can reuse simulations of the Green's functions several times for the source inversion (see section 4.3), while still allowing us to investigate the interdependence of the different updates. The final order and the evolution of the misfits is plotted in figure 6.4. While the traveltime misfit is reduced by ∼55 percent and further updates are possible, we reach the error level estimated for the asymmetry measurement after 6 iterations, which translates to a final misfit reduction of ∼30 percent. Each sequence of source updates has a minor influence on the following sequence of structure updates and vice versa. The related misfit changes are on the order of ∼1 percent (dashed lines in figure 6.4).

The final model for the distribution of the power-spectral density is shown in figure 6.5. The interpretation is not straightforward due to the two-sided nature of the sensitivity kernels of the asymmetry measurement (figures 2.3 and 4.2a). We thus mostly focus on the anomalies with high power-spectral density and avoid interpreting regions with magnitudes lower than average. Smearing effects along the two broad bands of rays described above that connect Europe and South America with Asia are visible, but do not dominate the features that we interpret in the following. The strongest sources are imaged in the oceans on the Northern Hemisphere, i.e. along the coasts of the northern Pacific and in the Northeast Atlantic. We also observe strong contributions in the Coral and Tasman Sea, in the southern parts of the Pacific, Atlantic and Indian Ocean. In general, sources on continents are weak, except for an anomaly in North Asia.

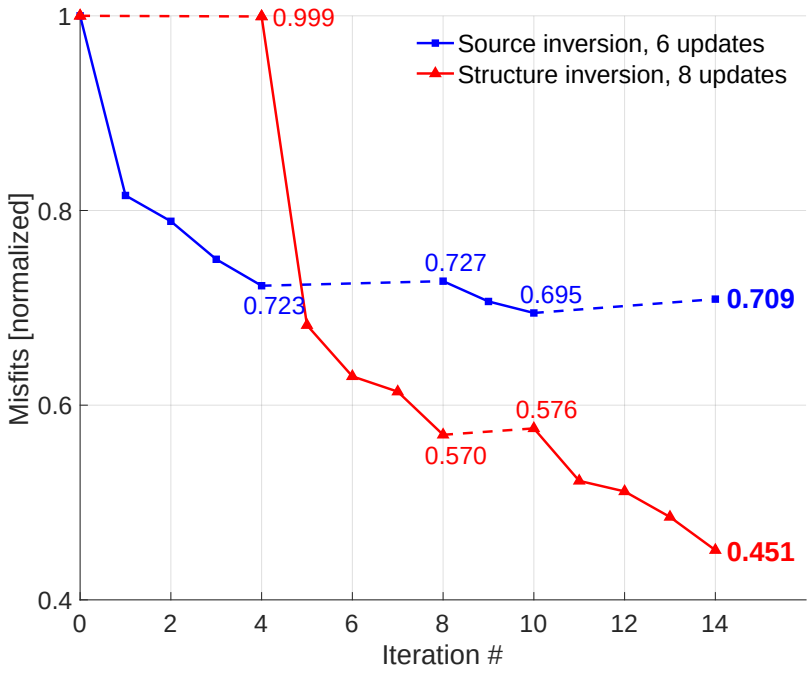

Figure 6.4: Misfit evolution for the source inversion (blue line) and for the structure inversion (red line). The dashed lines connect sequences of the same kind. Misfit values are given at the beginning and at the end of each sequence.

Most of the described features can be linked to the result obtained by *Ermert et al.* (2017). They use a precomputed database of Green's functions computed for S40RTS (*Ritsema et al.*, 2011) and Crust2.0 (*Bassin et al.*, 2000) to calculate correlation functions and source sensitivity kernels. Their final model is shown in figure 6.6. The anomalies in our study are more confined in space and more regions have zero power-spectral density, which are probably consequences of reducing the misfit more, i.e. by ∼30 percent instead of ∼18 percent in *Ermert et al.* (2017). This illustrates the benefit of choosing L-BFGS over steepest descent, since the models are updated 6 times in both cases. Major differences in our inversion result are weaker sources at the coast of Chile, stronger contributions in the southern Atlantic and in North Asia. All in all, we argue that our model supports the interpretation by *Ermert et al.* (2017) and their conclusions drawn regarding the excitation of the Earth's Hum. We refer the reader to their publication for more details.

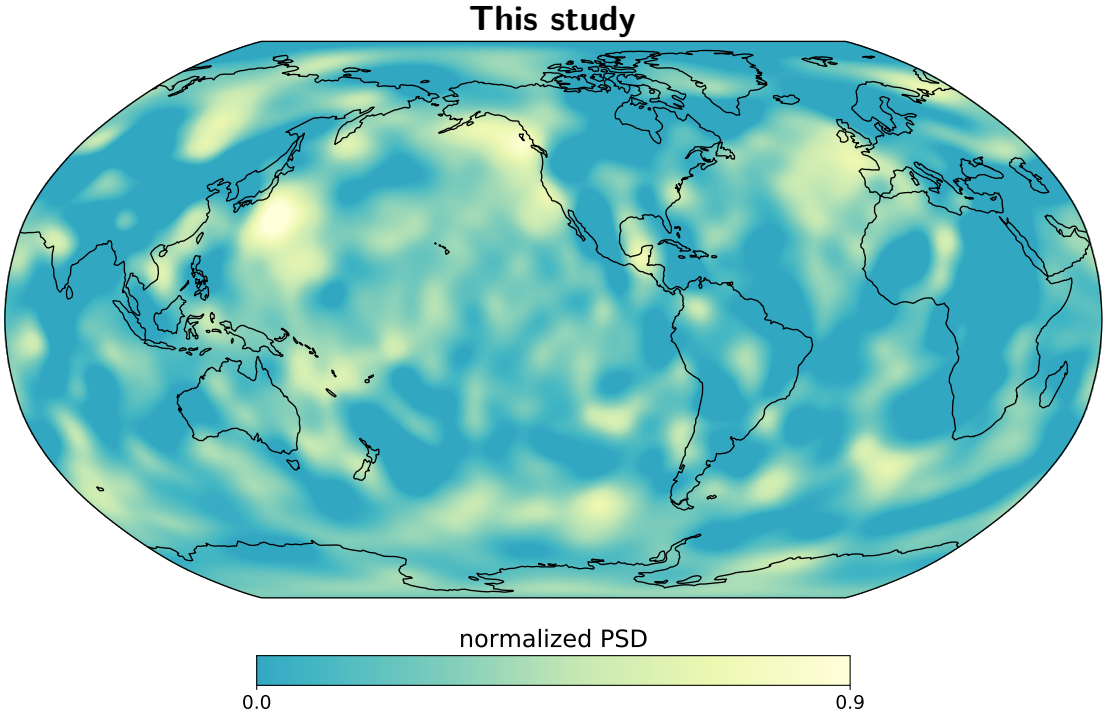

Figure 6.5: Final inversion model for the power-spectral density (PSD) distribution of the Earth's Hum. The values are normalized and the color bar is clipped to highlight regions with strong contributions.

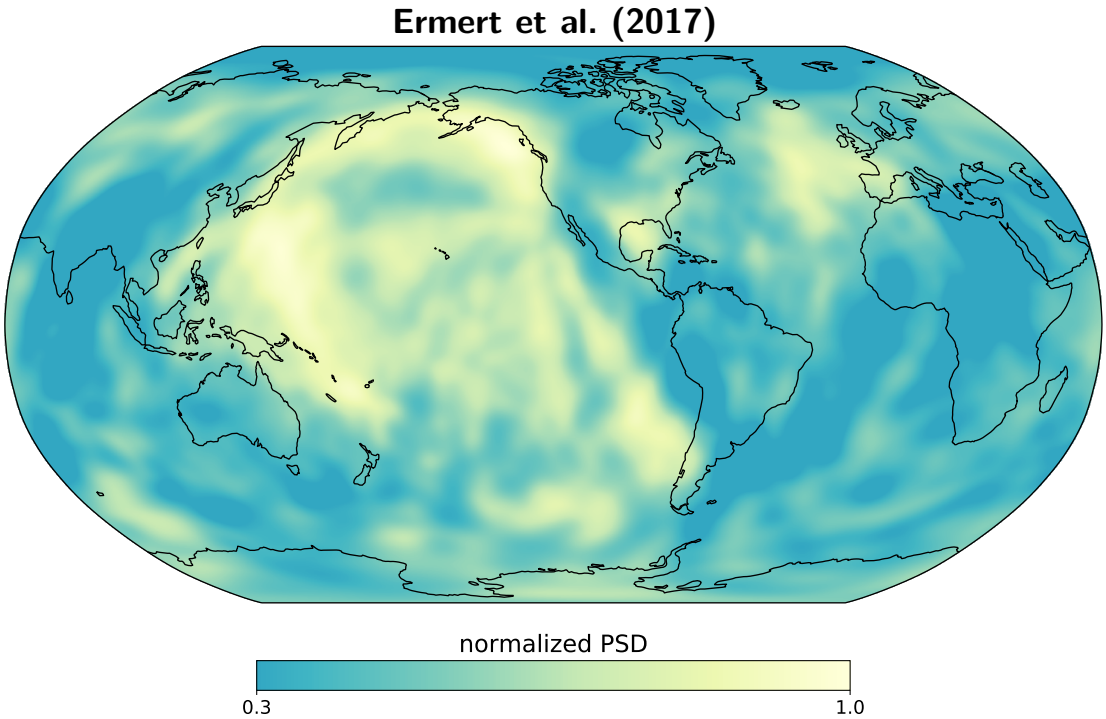

Figure 6.6: Hum source model (normalized) by Ermert et al. (2017). The color bar is clipped such that the mean has a similar color compared to figure 6.5.

The final VSV velocity model from the inversion of correlation functions for a period band between 100 and 300 s is presented in figure 6.7. In order to facilitate its interpretation we plot S20RTS (*Ritsema et al.*, 1999) at 100 km depth in figure 6.8. The depth for the comparison could be chosen differently to better match the depth sensitivity of Rayleigh waves (e.g. *Boschi et al.*, 2009), but we expect a strong imprint of the crust and upper mantle, since we do not account for its variability in our 1D starting model. A higher magnitude of the deviations from the mean in S20RTS can be explained by the exploitation of higher-frequencies and a different inversion approach.
Considering the wavelengths of several hundreds of kilometers and the relatively small number of time shift measurements in this study, we get a good agreement with S20RTS. The continental cratons are faster on average, i.e. North America, Australia and to a large extent also Eurasia, South America and Africa. We image a slow Pacific belt, the African rift system and the northern part of the Mid-Atlantic Ridge. Strong undulations of the crust caused by mountain ranges are imaged as slow anomalies, e.g. the Himalayas, the Andes and potentially also the Urals. *Nishida et al.* (2009) estimated a crustal correction for the considered period band and we observe a strong correlation with the features described above. As expected by the ray coverage (figure 6.3), the resolution in the Northern Hemisphere is significantly better compared to the Southern Hemisphere. We therefore present the additional comparison to the Collaborative Seismic Earth Model CSEM (*Afanasiev et al.*, 2016; *Fichtner et al.*, 2018) in figures 6.9 and 6.10 focusing on the Northern Hemisphere. We observe similar anomalies where CSEM is not updated since it starts from S20RTS and regional refinements appear as smooth versions in our model. For the identification of specific features, we refer the reader to the interpretation above. A smaller magnitude of the deviations from the mean is expected again for our inversion result, since information from higher frequency waveforms and more iterations are used for the regional refinements in CSEM.

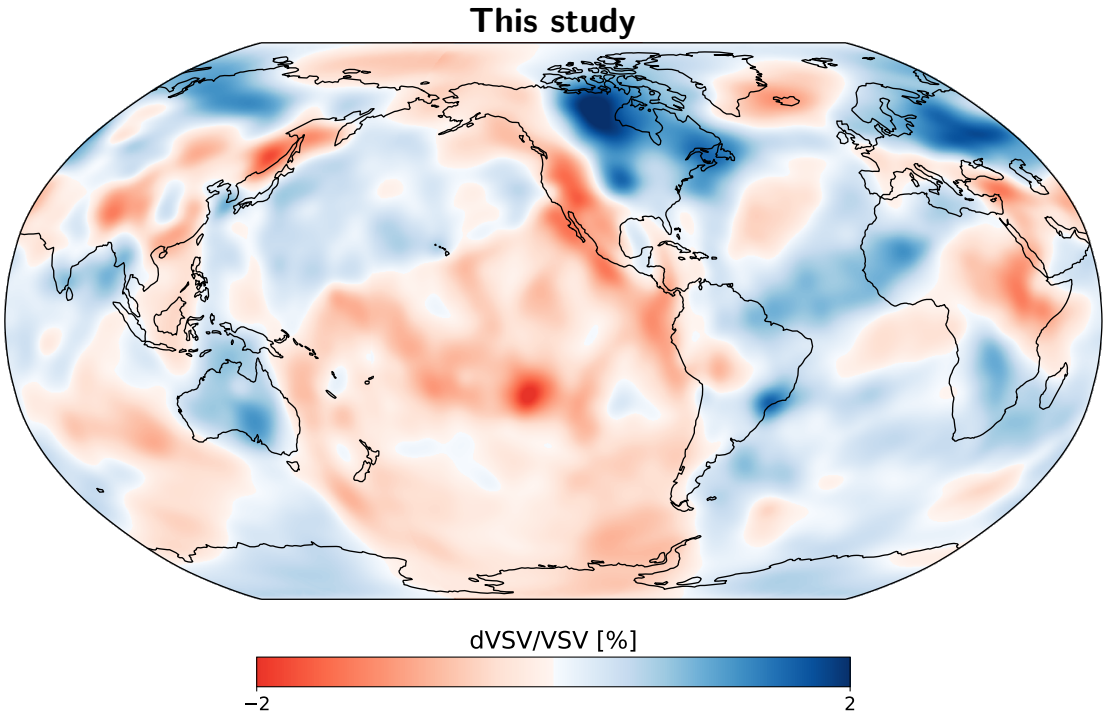

Figure 6.7: Final inversion result for VSV presented in deviations from the mean in percent.

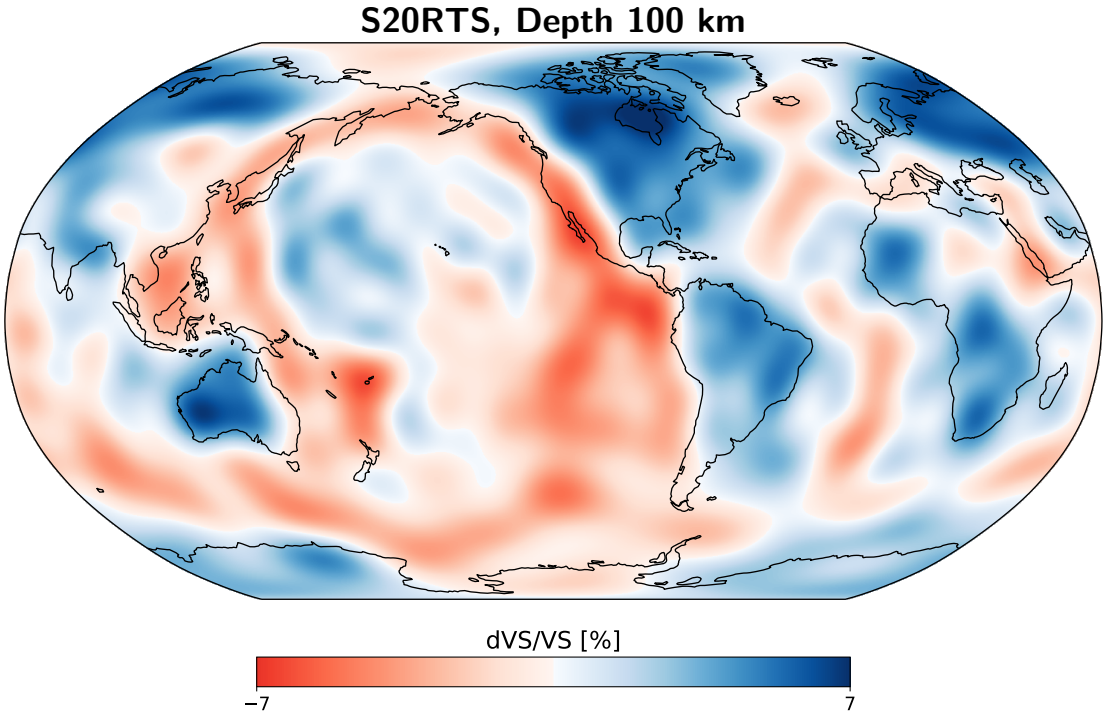

Figure 6.8: S20RTS plotted at 100 km depth in deviations from the mean. The velocity model was downloaded from Submachine (https://www.earth.ox.ac.uk/~smachine, *Hosseini et al.*, 2018).

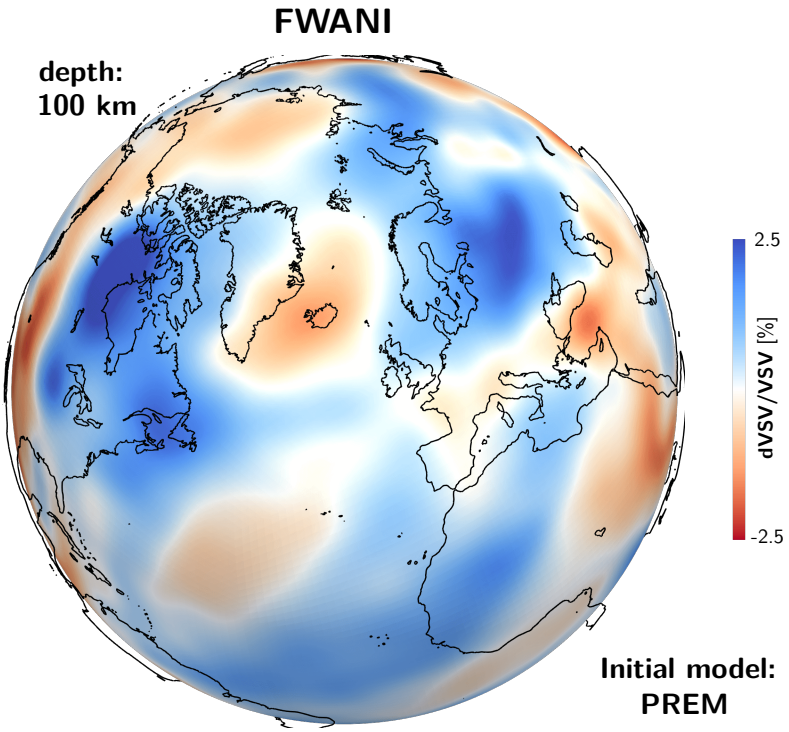

Figure 6.9: Final inversion result for VSV with a focus on the Northern Hemisphere.

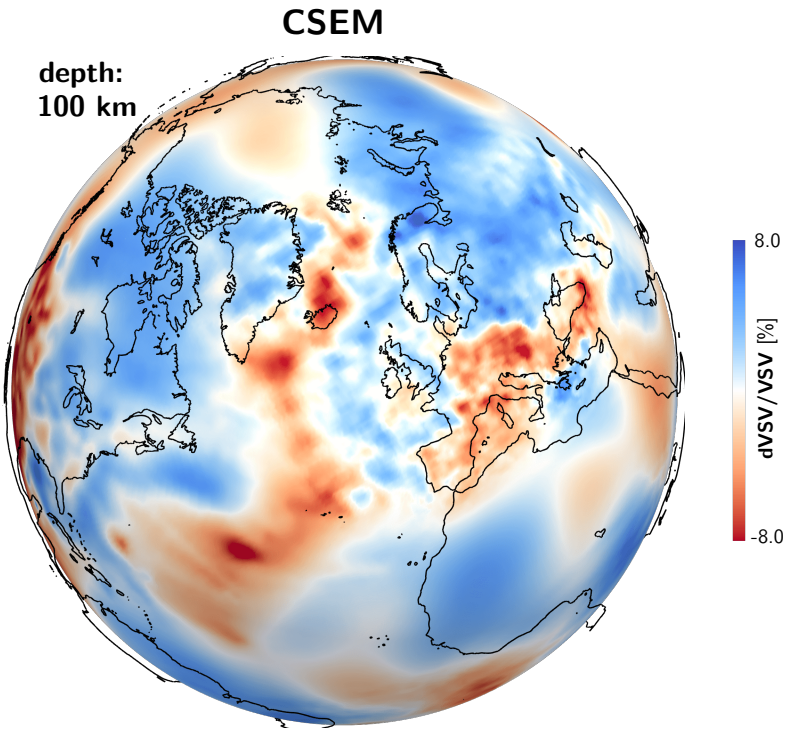

Figure 6.10: VSV velocity model of CSEM at 100 km depth with a focus on the Northern Hemisphere.

6.4 CSEM update

With the successful proof of concept in section 6.3, we take the opportunity and contribute to the Collaborative Seismic Earth Model CSEM (*Afanasiev et al.*, 2016; *Fichtner et al.*, 2018). The goal of CSEM is to provide a collaborative and evolutionary framework for the construction of a 3-D model of the internal structure of the Earth. At the current stage, the model is mostly based on waveforms from earthquakes. Noise correlations are also included for the Iberian Peninsula and for Southeast Asia, however, under the simplifying assumption of Green's function retrieval. Full waveform ambient noise inversion enables us to include correlation functions in a more consistent way.
The first-generation CSEM contains 12 regional refinements built from waveform data with varying minimum period. One global inversion was performed to ensure the consistency of the different sub-regions. Similarly, we use the existing CSEM model and apply a global update using the dataset and framework described above. In order to represent the small-scale features in the regional refinements, small elements are necessary if the velocity model is defined on their vertices and the simulations would be expensive. We thus use the Gauss-Lobatto-Legendre (GLL) basis of the discretized model to define the velocity model, which allows us to keep large elements and to represent most features in CSEM. We acknowledge support and effort from Sölvi Thrastarson and Dirk-Philip van Herwaarden as well as Christian Boehm, who made it possible on the CSEM- and the Salvus-side, respectively.

We start again from a homogeneous distribution of noise sources, follow the procedure for the first sequence in section 6.3 and update the source distribution 4 times. The misfit reduction and resulting model are presented in figures 6.11 and 6.12. Although a comparison of models that have not converged is difficult, we also show the source model after 4 iterations with PREM as structure model in figure 6.13. As expected, the features in the latter are less pronounced compared to the final model presented in section 6.3. While with PREM we observe sources in North Asia that are stronger than imaged by *Ermert et al.* (2017), using CSEM reduces the difference. In addition, the strong contribution close to Japan and in the North Atlantic are slightly more focused.

The structure update (see figure 6.14) is meant to ensure the consistency of the different models and should not be the dominant feature of CSEM. We thus follow *Afanasiev et al.* (2016) (see figure 9 therein) and only allow maximum perturbations of $\sim$1 percent. Comparing the gradients with PREM as starting model, we conclude that there is no clear correlation between the regional refinements in CSEM and our global update. We restrain ourselves and do not go into details with the interpretation of the gradient.

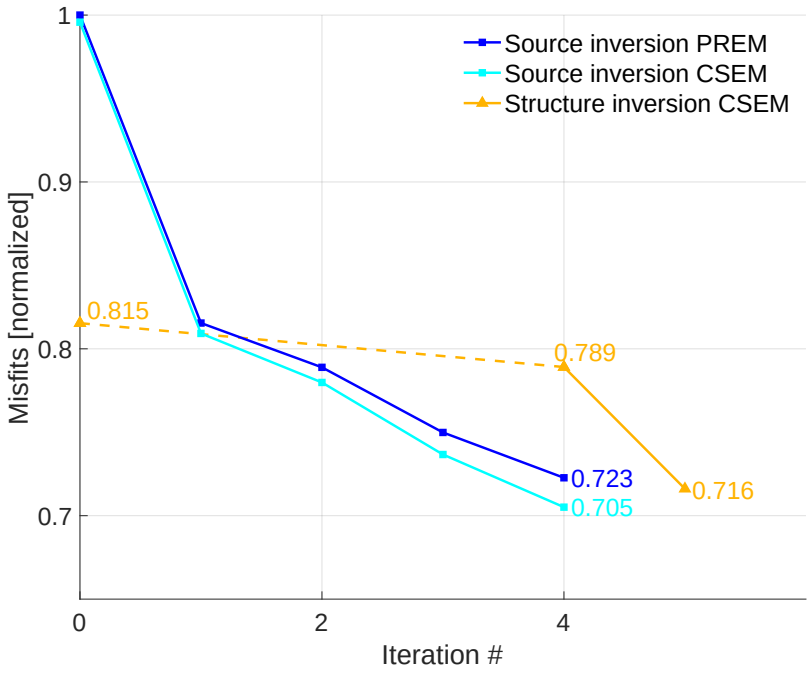

Figure 6.11: Misfit evolution for the source inversion (cyan line) and traveltime misfit reduction by updating CSEM with a maximal absolute perturbation of 1 percent (orange line). The evolution of the first source inversion sequence with PREM as structure model is shown in blue. The misfit values are presented relatively to the respective initial misfits with PREM as starting model (section 6.3). The dashed line connects the initial traveltime misfit and the value after the source inversion.

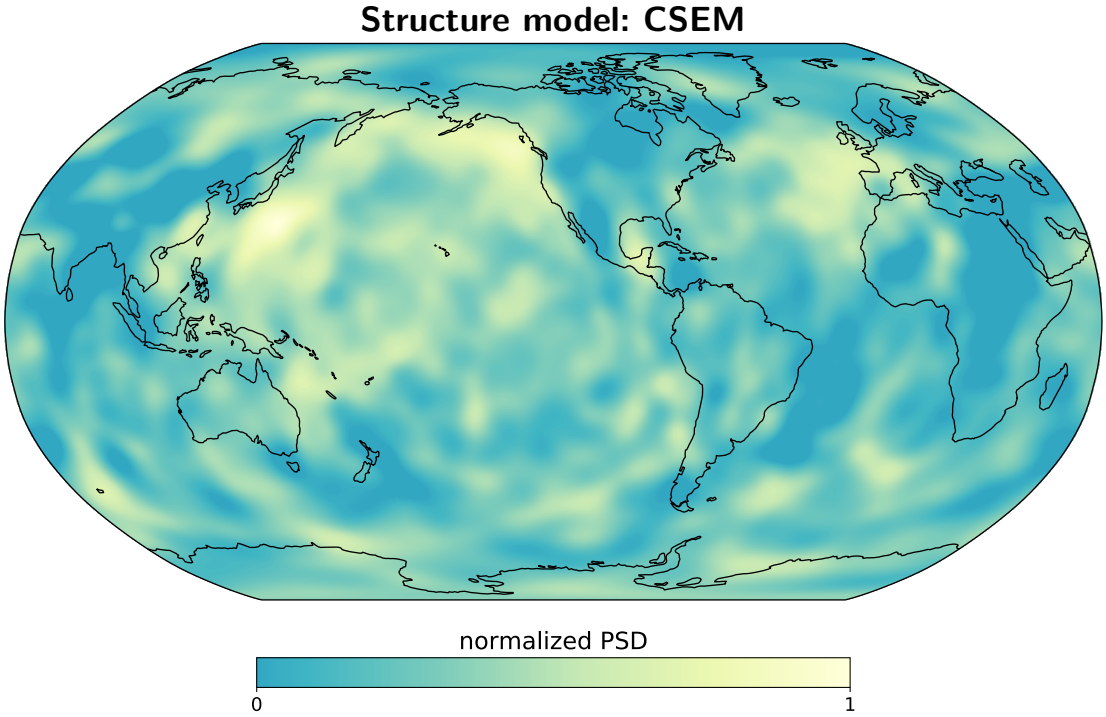

Figure 6.12: Distribution (normalized) of the power-spectral density of the Earth's Hum after 4 iterations with CSEM as structure model.

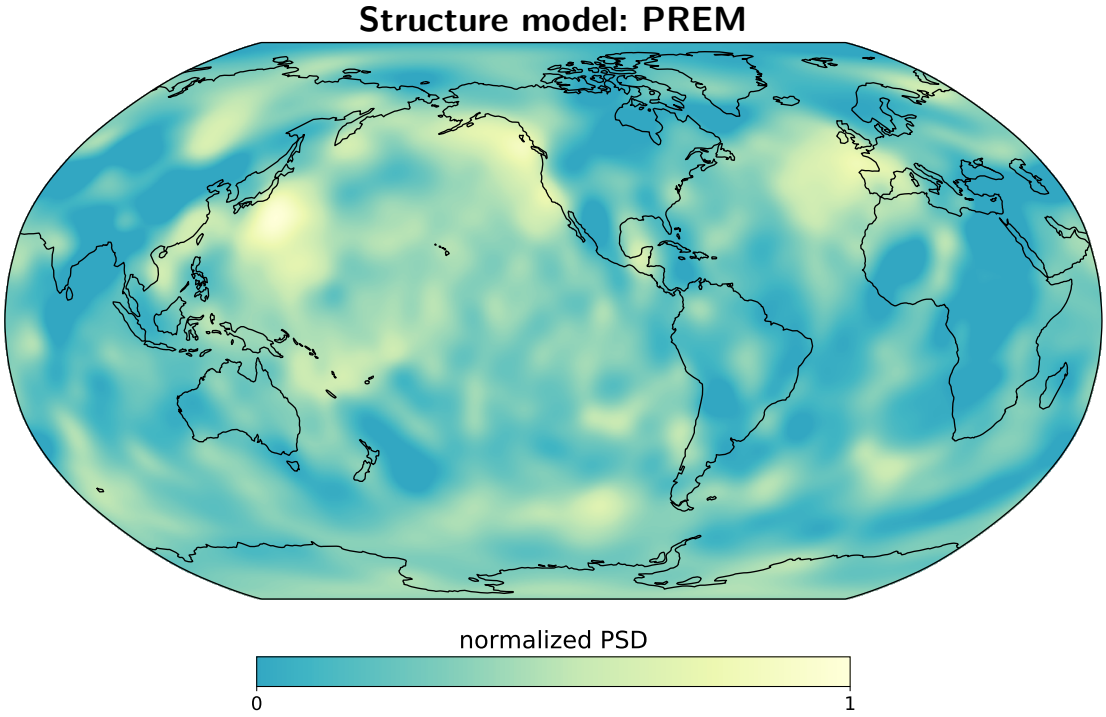

Figure 6.13: Same as figure 6.12, but with PREM as structure model. Its maximum value (3.61e10) is slightly lower than the maximum (3.63e10) in figure 6.12. The latter is used for the normalization in both figures. The maximum value of the final inversion model shown in figure 6.5 is almost twice as large (5.61e10).

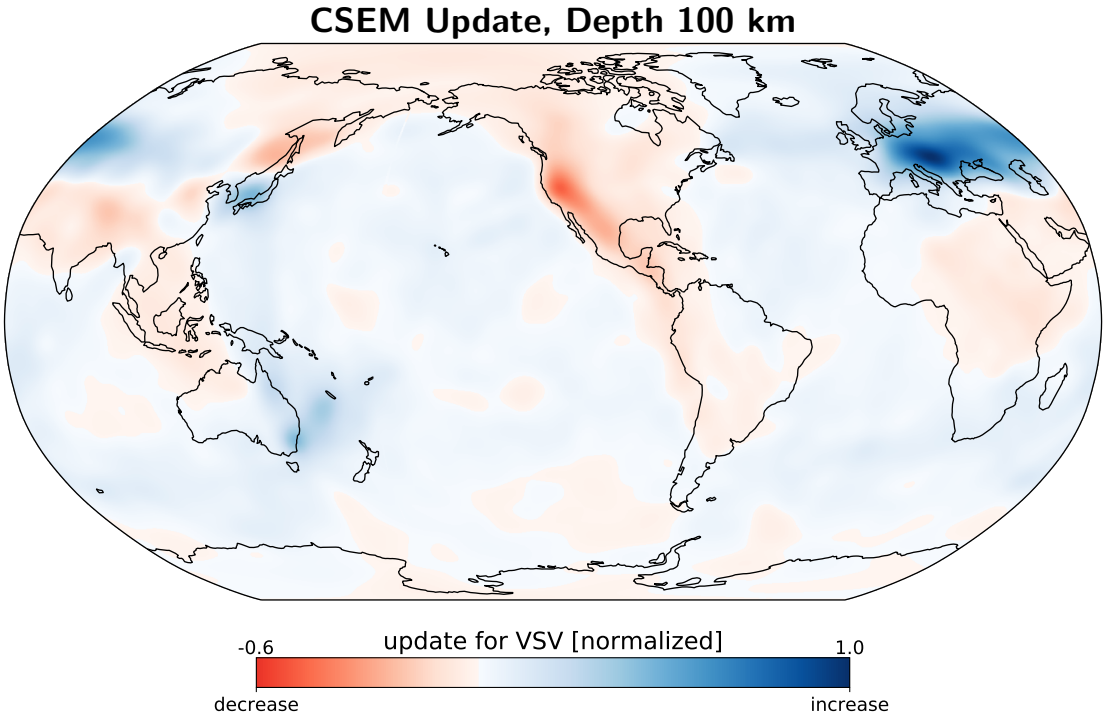

Figure 6.14: VSV update for CSEM at 100 km depth. The update is normalized and the color bar is clipped to enhance certain features. Blue (red) indicates that the velocity is increased (decreased) in order to reduce the misfit.

6.5 Conclusions

The inversion for the distribution of noise sources and for structure reveals reasonable results. Full waveform ambient noise inversion can thus be used as a tomographic method by itself and has the potential to provide complementary information in regions with poor earthquake coverage, e.g. in North Asia. We are able to confirm the findings by *Ermert et al.* (2017) and identify tomographic features that are known from global velocity models. For the tomography it is important to point out that we only use ~1,600 time shift measurements, which is orders of magnitude less than typically considered for global scale inversions (e.g. *Ritsema et al.*, 1999; *Simmons et al.*, 2010; *Ritsema et al.*, 2011; *Lebedev and Schaeffer*, 2013; *Auer et al.*, 2014; *French and Romanowicz*, 2014; *Bozdağ et al.*, 2016).

Ideas for Future Research 7

This chapter is supposed to summarize different projects that we started and to give ideas for possible future research directions. The selection of topics represents our current state of knowledge and is as such, of course, biased. We recommend to take it with a grain of salt and hope that it does not narrow the reader's creativity. New ideas and innovative approaches can render our thoughts below superfluous relatively quickly. Please keep that in mind while reading it (also addressed to ourselves).

7.1 Joint inversion of earthquake data and noise correlation functions

Ambient noise tomography is generally accepted as a tomographic method and also believed to provide complementary information compared to earthquake tomography in terms of coverage in space and frequency. In the inversion presented in chapter 6, for instance, North Asia is covered relatively well, where the distribution of earthquakes is sparse. A joint inversion of earthquake data and ambient noise correlations is thus a logical next step. It is already done by means of dispersion curve analysis (*Yang et al.*, 2008; *Zhou et al.*, 2012) and is, in principle, possible with full waveform inversion by means of ambient noise adjoint tomography (*Chen et al.*, 2014; *Lu et al.*, 2018), since it is based on exactly the same framework used for earthquakes (*Simutė et al.*, 2016; *Krischer et al.*, 2018). Independent of the applied tomographic method, errors in the source properties deteriorate tomographic reconstructions (*Valentine and Woodhouse*, 2010). Violating the assumptions necessary for Green's function retrieval is a source of uncertainty and we argue that the effects become more critical when the extraction of waveform information is increased. Full waveform ambient noise inversion consequently provides a more consistent framework for the proposed joint inversion. Since our implementation is based on Salvus, a first attempt to combine both data types is straightforward.

7.2 Source distribution in finite domains

A crucial component that determines to a large extent the success of full waveform ambient noise inversion is the inference of the distribution of noise sources. As stated above, errors in the source properties are mapped into tomographic images of Earth structure. Ambient noise source studies see contributions from far away (*Schulte-Pelkum et al.*, 2004; *Hillers and Ben-Zion*, 2011), which impedes a straightforward truncation of the computational domain. While attenuation reduces the effect of distant sources, current processing techniques applied in ambient noise tomography try to homogenize the azimuthal coverage (*Bensen et al.*, 2007), which can have the tendency to down-weight local sources and to enhance distant contributions. For specific period bands and noise source distributions keeping the processing as minimal as possible might thus already allow a restriction of the domain. From the point of view of tomography, an alternative representation of the ambient noise source distribution that captures the illumination but forbids an interpretation of the source distribution as a physically meaningful quantity is a viable approach. The idea presented in the following falls into this category.
Delaney et al. (2017) investigated the effect of heterogeneous and non-stationary noise sources on traveltime estimates of surface waves in the context of noise-based monitoring. They proposed to quantify the source-induced bias, which may induce velocity changes of up to 0.25 percent within one day, and then correct for it in either the data or model space. The source distribution was parameterized simplistically in terms of an annulus surrounding the investigated array, which encompasses the azimuthal variation of the power-spectral density distribution.

First steps towards a new source parameterization
Preliminary work on improving the source parameterization favors a representation with a superposition of eigenvectors of the Hessian matrix (see figures 7.1 and 7.2), i.e. based on the second derivatives derived in chapter 2. This source parameterization has several advantages:

(i) Sources within and potentially also outside the computational domain can be incorporated, both not possible with a ring of sources. Waves from distant noise sources, for instance, basically arrive as plane waves and it might be possible to capture them with this parameterization.

(ii) The eigenvectors describe what is possible to resolve with the station geometry, similar to array response functions (*Rost and Thomas*, 2002).

(iii) The parameterization adapts to the physical content of the observed correlation functions.

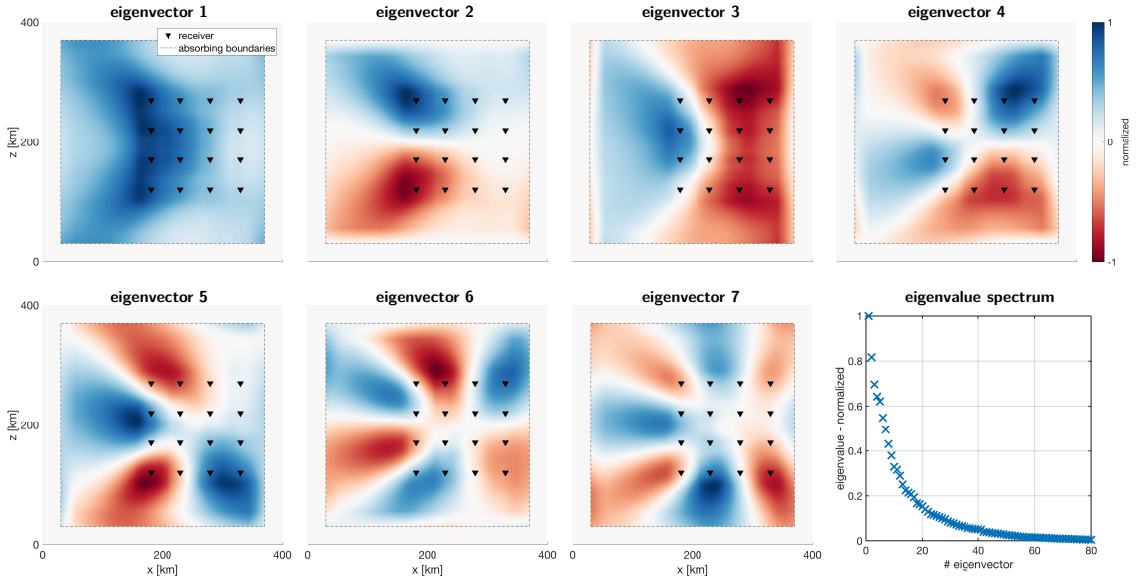

Figure 7.1: Examples of eigenvectors proposed for the improved parameterization of the noise source distribution. The eigenvectors and eigenvalues describe what is resolvable with the available data. They change, for instance, with station geometry and with the employed measurement (waveform differences in this case). With increasing number, the complexity of the eigenvectors increases and the respective eigenvalue, i.e. the inverse of the associated uncertainty, decreases (bottom right). Data errors define a threshold for the maximum eigenvectors resolvable in an inversion and thus only a limited number is required.

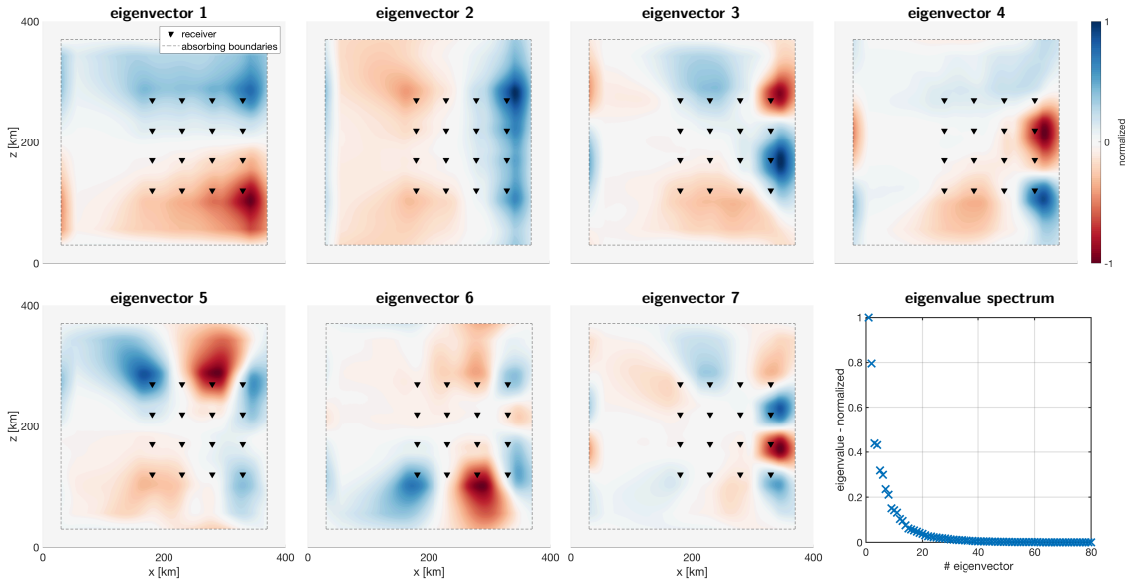

Figure 7.2: Same as figure 7.1, but for the asymmetry misfit function defined in equation (3.1).

.

(iv) A probabilistic inversion for the distribution of noise sources is rendered feasible. Due to data errors and the exponential decay of the eigenvalue spectrum, only a limited number of eigenvectors can be resolved in a realistic inverse problem. With a precomputed set of correlation functions for each eigenvector, which is possible since our forward problem is linear in the power-spectral density distribution, the computational costs remain easily manageable.

This novel approach to set up the source distribution opens the door to go beyond *Delaney et al.* (2017) and potentially to account for space- and time-dependent noise source distributions in finite domains.

7.3 Different ways to extract information from cross-correlations

The applications to real data only focus on Rayleigh wave signals so far and the rest of the correlation functions is discarded (chapter 6, *Ermert et al.*, 2017). This is a choice made at the current stage of the developments to reduce the complexity. For conventional approaches based on Green's function retrieval, however, this can be seen as a necessity enforced by the "imperfect" nature of ambient noise sources (see chapter 5). New ways to extract reliable information from cross-correlation functions is an important next step to exploit the potential of full waveform ambient noise inversion and to keep the promises made above. We present ideas and first attempts in the following.

7.3.1 Comparison relative to reference correlation

A common approach in coda wave interferometry is to compute reference correlation functions by stacking over a long time period, e.g. for temporal station deployments the entire time data was recorded, and then to compare averages computed for short time scales (typically on the order of few days) to the reference (*Obermann et al.*, 2013, 2014; *Hillers et al.*, 2015). This enables an extraction of information that would not be possible by studying short-term averages directly. For full waveform ambient noise inversion this translates to an inversion of a reference dataset for both a source and a structure model. Short-term averages can then be inverted relative to the reference dataset and model. This has the potential to facilitate the investigation of the time evolution of ambient noise sources and of structural changes.
Considering different averaging times raises questions about the minimum averaging length required for a meaningful extraction of information. Understanding correlation functions as a representation of a certain time period renders a criterion in terms of convergence redundant. Nevertheless, a certain averaging length is required to detect the coherency in the ambient noise field. For the current theoretical formulation with the assumption of spatially uncorrelated noise sources (see equation (2.5)), their cross-talk should have a small

contribution. A correlation between neighboring noise sources is incorporated implicitly, since it can be interpreted as a low-pass filter acting on the distribution of the ambient noise sources. A cross-talk between noise sources that are spatially separated and independent of each other is, however, difficult to capture and assumed to be reduced by increasing the averaging length. There are numerous studies investigating effects of the averaging length with respect to the retrieval of Green's functions (e.g. *Bensen et al.*, 2007), but full waveform ambient noise inversion opens news doors and requires different objectives (*Fichtner et al.*, 2017).

7.3.2 New misfit functionals

7.3.2.1 Time asymmetry measurement

Besides the asymmetry in amplitude used for the inversion for ambient noise sources in chapter 6, heterogeneous noise source distributions also introduce an asymmetry in time of the surface wave packages. Clock errors and changes in the phase response of a station have the same effect, but *Stehly et al.* (2007) showed that it is feasible to detect and correct for them. They hypothesize that the residual is due to heterogeneous noise sources. Although the asymmetry in time is small in magnitude, its measurement has the advantage that it does not rely on physically meaningful absolute amplitudes. In the following, we present the misfit function and derive the corresponding adjoint source time function.
We use the definition of traveltime shifts employed in the chapters above and measure time shifts on the causal and acausal surface wave packages. Since the sign convention is different for both branches (see figure 4.1), the misfit $\mathcal{X}$ is based on the sum of both measurements T_{caus} and T_{acaus} and we define it as

$$\mathcal{X} = \frac{1}{2}(T_{\text{caus}} + T_{\text{acaus}})^2, \tag{7.1}$$

where the subscripts here and in the following indicate the windowing of the arrivals of interest. The first-order change of the misfit for a variation in the correlation function δC is given by

$$\nabla_C \mathcal{X}\,\delta C = (T_{\text{caus}} + T_{\text{acaus}}) \cdot (\nabla_C T_{\text{caus}}\,\delta C_{\text{caus}} + \nabla_C T_{\text{acaus}}\,\delta C_{\text{acaus}}). \tag{7.2}$$

We follow the derivations in chapter 11 of *Fichtner* (2010) and write the variation of the traveltime shift due to δC as

$$\nabla_C T\,\delta C = \int\int \frac{1}{N}\,\partial_t C^o(\mathbf{x}, t-T)\,\delta C(\mathbf{x}, t)\,\delta(\mathbf{x}-\mathbf{x}_r)\,dt d\mathbf{x}, \tag{7.3}$$

where $C^o(\mathbf{x}, t-T)$ denotes the observed correlation function shifted in time by T and N is given by

$$N = \int \partial_{tt} C^o(\mathbf{x}_r, t-T)\, C(\mathbf{x}_r, t)\, dt. \tag{7.4}$$

Combining equations (7.2) and (7.3) with (2.14) and (2.24), the adjoint source time function f is given by

$$f(\mathbf{x}, t) = -(T_{\text{caus}} + T_{\text{acaus}}) \cdot \Big(\frac{\partial_t C^o_{\text{caus}}(\mathbf{x}, t-T)}{N_{\text{caus}}} + \frac{\partial_t C^o_{\text{acaus}}(\mathbf{x}, t-T)}{N_{\text{acaus}}} \Big)\, \delta(\mathbf{x} - \mathbf{x}_r). \tag{7.5}$$

Both the misfit and the adjoint source time function are implemented in the 2-D framework used in chapter 3. We use the same model setup, now with a homogeneous velocity model, consider two receivers 400 km apart and simulate synthetic observations for a homogeneous distribution of noise sources perturbed with a Gaussian anomaly behind one of the two stations. We then compute synthetics without the source perturbation and compare them to the observations in terms of three misfit functions: (i) amplitude asymmetry according to equation (3.1), (ii) time asymmetry and (iii) cross-correlation time shifts. The resulting source and structure kernels are presented in figure 7.3. Measurements exploiting asymmetries in correlation functions lead to a two-sided nature of the source sensitivity kernels. The ratios between source and structure kernels give an indication of the trade-off behavior of the measurements. For both asymmetry measurements, we observe a similar relative importance of the structure kernels, which is approximately one order of magnitude less compared to the misfit based on cross-correlation time shifts. In contrast to the amplitude asymmetry, the structure kernel for the time asymmetry shows a pronounced first Fresnel zone, which might lead to a more constructive build-up of structure anomalies. On the other hand, the first Fresnel zone of the respective source kernel is narrower, which may help to locate noise sources more precisely.
Further research is required to assess the full potential of time asymmetry measurements. In conclusion, it is, however, worth pointing out that apparent imperfections in the interpretation of noise correlation functions in terms of Green's functions contain valuable information and can be exploited with our approach.

7.3.2.2 Non-physical arrivals

In chapter 5 we reveal that signals before the surface wave, including "too-early-to-be-physical" arrivals, contain valuable information on the distribution of ambient noise sources and *Retailleau et al.* (2017) demonstrated their potential to improve the resolution of source inversions. Our hypothesis is that signals before the surface wave arrival are an indication of spatially localized sources. The final source model in chapter 6 is presumably too smooth for these signals to emerge. Including them in the inversion in terms of energy measurements has the flaw of including absolute amplitude information. Its interpretation is up for debate

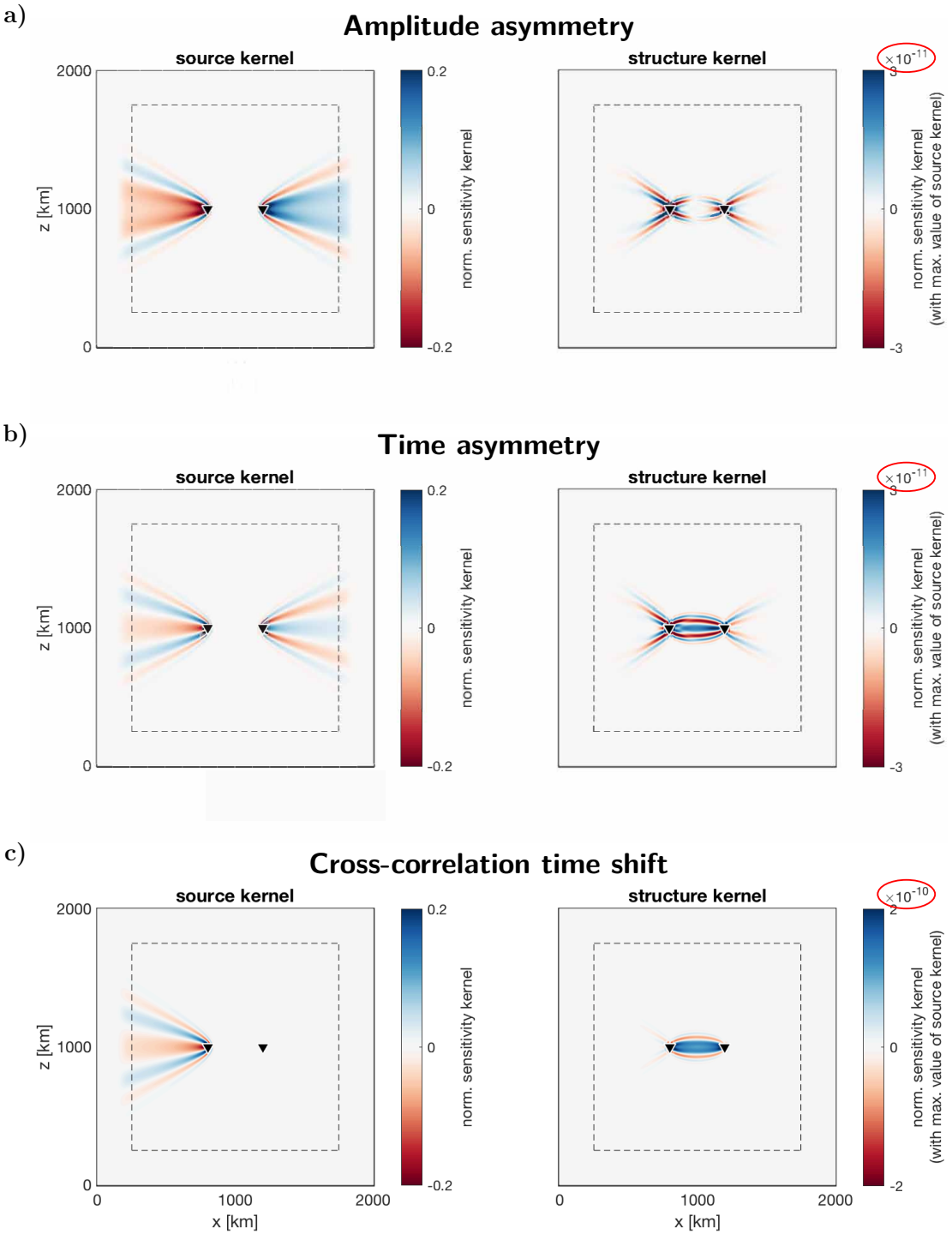

Figure 7.3: Sensitivity kernels in 2-D for source (left) and structure (right) for measurements based on the a) amplitude asymmetry, b) time asymmetry and c) cross-correlation time shifts. In order to allow for conclusions regarding trade-offs, we normalize the structure kernels with the maximum absolute value of the corresponding source kernel. Specifics of the model setup are described in chapter 3.

(*Prieto et al.*, 2011; *Tsai*, 2011; *Stehly and Boué*, 2017), but relative amplitudes of spurious arrivals compared to surface wave signals should have a physical meaning. Including these arrivals is a crucial next step to harness the possibilities full waveform ambient noise inversion provides.

7.4 Trade-off analysis in 3-D

The extension of the trade-off analysis presented in chapter 3 to 3-D is in our opinion essential to advance our understanding of the physics of the problem and to explore the limitations of full waveform ambient noise inversion. Studying how scatterers can be interpreted as sources and vice versa by means of trade-off kernels can provide new insights. In addition, second derivatives pave the way for resolution analysis. The discrepancies between our inversion result presented in chapter 6 and the model by *Ermert et al.* (2017), for instance, would benefit from quantitative resolution estimates.

7.5 Full correlation tensor and horizontally acting noise sources

For this thesis we limited ourselves to correlations between vertical recordings and only included vertically acting noise sources. Observations, however, require an extension of the framework to horizontally acting noise sources and the analysis typically involves the full correlation tensor, preferably in terms of radial, transverse and vertical components (*Xu et al.*, 2019). *Kurrle and Widmer-Schnidrig* (2008) reported a permanent excitation of toroidal modes, which was confirmed by *Nishida* (2014). Also in both primary and secondary microseisms Love and SH waves have been observed (*Rind and Down*, 1979; *Nishida et al.*, 2008; *Tanimoto et al.*, 2015; *Juretzek and Hadziioannou*, 2016; *Nishida and Takagi*, 2016). Different models for the excitation of microseim Love waves are discussed (*Fukao et al.*, 2010; *Saito*, 2010) and at least for the secondary micorseism, for instance, multiple scattering with wave conversions is not sufficient to explain observed Love to Rayleigh wave ratios (*Ziane and Hadziioannou*, 2019). The proposed extension of our framework could thus contribute to the understanding of the generation of ambient noise. It mostly requires a generalization of the developed framework and major complications are not expected.

7.6 Auto-correlation functions

Claerbout (1968) showed in his seminal paper that the reflection response can be retrieved by the auto-correlation of the transmission response. Quite recently, studies picked up on the topic again in the context of crustal imaging (*Tibuleac and von Seggern*, 2012; *Gorbatov et al.*, 2012; *Clayton*, 2018; *Romero and Schimmel*, 2018; *Viens et al.*, 2018). Auto-correlations are used to investigate reflectors and have the potential to also reveal changes in time due to the ubiquity of the ambient noise field. The energy at zero-time lag and the side lobes can mask reflections of interest and from our experience from cross-correlations we argue that heterogeneous noise source distributions may introduce spurious arrivals. Insight by studying the sensitivity to source and structure may be helpful for future studies. The developed framework for cross-correlations works out of the box also for auto-correlations. In figure 7.4 we consider a box domain with a homogeneous distribution of noise sources at the free surface, a reflecting boundary at the bottom and absorbing boundaries at the sides. We place a receiver at the top and simulate a synthetic auto-correlation for a maximum frequency of 4 Hz. We then measure the energy in a window defined around the expected P-wave reflection and compute the corresponding source and structure kernels. We observe sensitivity to sources in ring-shaped features with a dominant contribution at the receiver location. The ray-theoretical interpretation borrowed from chapter 5 suggests an interaction between P-/S-wave reflections with direct P-/S-waves and surface waves. The structure kernel is dominated by sources at the receiver and has the shape of a cone. Sensitivity to structure from cross-terms is small and mostly constrained to the surface. Further investigations are necessary before drawing definite conclusions. Removing the sources at the receiver location and increasing the complexity of the model by introducing more layers are obvious next steps.

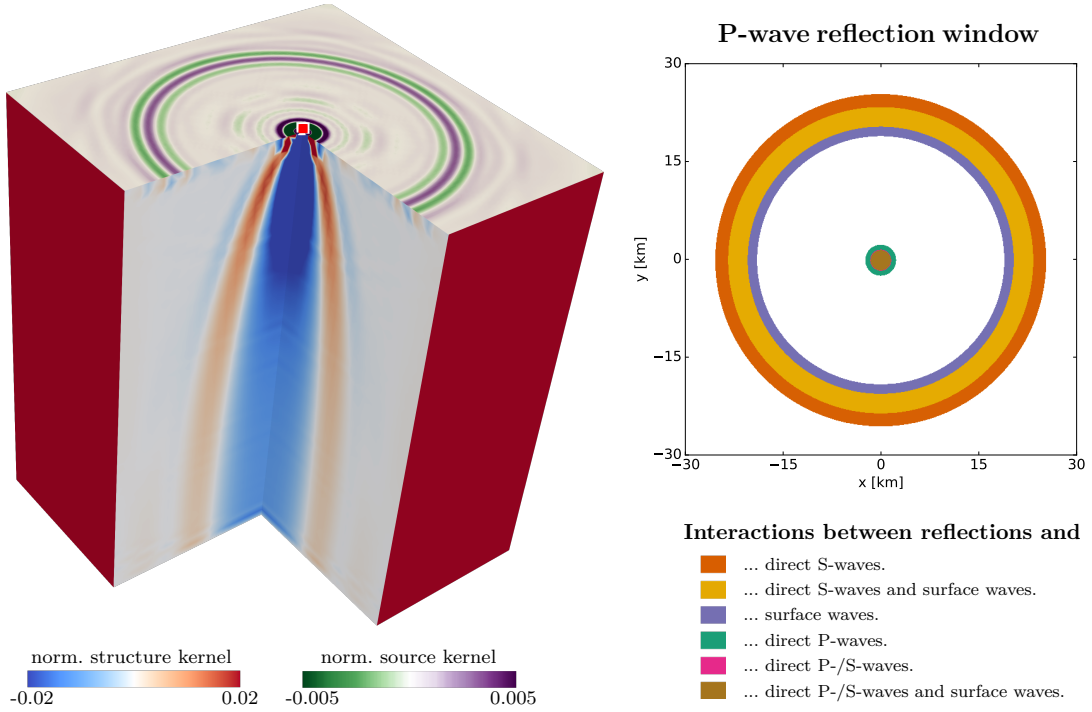

Figure 7.4: Source and structure kernel (left) for the P-wave reflection time defined on an auto-correlation function. The box domain is 30 km deep and the P- and S-wave velocities are set to 5.8 and 4.0 km/s. The receiver is located at the surface of the domain (red square). The ray-theoretical interpretation of the source kernel (right) reveals the interaction of different wave types.

7.7 Monitoring with Full Waveform Ambient Noise Inversion

Parts of this section were submitted as a proposal for an Early PostDoc.Mobility fellowship offered by the Swiss National Science Foundation. Having read the previous chapters, some background information is redundant, but it allows one to read this section independently and potentially helps the reader to understand the reasoning behind the project.
Monitoring is a challenging field of application, since a high resolution is essential not only in space, but also in time. We see it as a final enemy and its defeat probably requires a combination of the ideas presented above.

7.7.1 Motivation

Monitoring of time-variable systems, such as geothermal and hydrocarbon reservoirs, aquifers, active faults and volcanoes, is crucial for hazard and risk management and allows for decisions at an early stage that can save lives and prevent damage. In the context of deep geothermal reservoirs, for example, which recently attracted considerable attention as an alternative energy source (e.g. *International Energy Agency*, 2011), earthquakes can be induced by the injection of high-pressure fluids necessary for an efficient extraction of thermal energy stored in the Earth. The induced seismicity cannot only lead to significant damage, but also to the loss of support by the society (*Kraft et al.*, 2009). Two recent projects in Switzerland (Basel, 2006 and St. Gallen, 2013) had to be stopped. Continuous monitoring that is not based on already induced seismicity and that allows for a precise localization of (induced) subsurface changes in both space and time is indispensable to assess reservoir dynamics and to react as early as possible. The ambient seismic field, persistent in time and ubiquitous in space, is a promising candidate for such an endeavor, but current techniques are limited in temporal and spatial resolution or require a vast amount of seismic stations. An extension of full waveform ambient noise inversion to account for the time-variability of ambient noise sources has the potential to overcome these limitations. Given the same amount of data we will be able to extract more information, since our model with heterogeneous and time-variable noise sources captures the actual physics more accurately. We can thus achieve a higher temporal resolution compared to current techniques.

7.7.2 Seismic tomography with ambient noise

Recordings of the ambient noise field appear entirely random without any hope that useful information can be extracted. Nevertheless, the physics of wave propagation introduces a coherency that can be detected by computing the cross-correlation function between different recordings. For linear processes like seismic wave propagation, the correlation function of random output time series approximates the system response to an impulse,

i.e. the Green's function. The empirical confirmation that this concept can be applied to ambient field recordings to extract surface waves (*Shapiro and Campillo*, 2004; *Sabra et al.*, 2005a) prompted a large number of regional and also global tomographic studies relating cross-correlations with Green's functions (e.g. *Shapiro et al.*, 2005; *Sabra et al.*, 2005b; *Nishida et al.*, 2009). The transformation of receivers into virtual sources allows us to control and increase the illumination in tomographic studies, which was previously dictated by the sparse distribution of earthquakes. Correlations and Green's functions are, however, only identical under specific conditions, including wavefield diffusivity and equipartitioning (*Lobkis and Weaver*, 2001; *Weaver and Lobkis*, 2001) or, equivalently, the isotropic distribution of both monopolar and dipolar uncorrelated noise sources (*Wapenaar*, 2004; *Snieder*, 2007). Realizing the low probability to meet these conditions, subsequent studies focused on the nature of the ambient noise field and its impact on the accuracy of ambient noise tomography.

7.7.3 The nature of seismic noise - setting limits for noise tomography

The ambient seismic noise field is excited by a heterogeneous and non-stationary distribution of noise sources. As explained in the introduction, the primary and secondary microseism as well as the Earth's Hum originate in the oceans. Irrespective of the excitation type, the magnitude of ambient noise sources varies considerably in space and depends on the ocean state, atmospheric conditions, etc. which may vary over short timescales. The assumptions necessary for Green's function retrieval are consequently not met and the discrepancy between reality and theory unavoidably affects ambient noise tomography. Heterogeneous and non-stationary noise source distributions deteriorate the recovery of the Green's function and represent a source of uncertainty. Body waves and higher-mode surface waves are not excited correctly (*Halliday and Curtis*, 2008; *Kimman and Trampert*, 2010), spurious arrivals are introduced (*Snieder et al.*, 2006) and amplitudes as well as traveltimes are biased (*Weaver et al.*, 2009; *Yao and van der Hilst*, 2009; *Tsai*, 2009, 2011). Great progress has been made in the last decade based on Green's function retrieval. The discussed deficiencies are, however, a limiting factor and prohibit the application of modern tomographic techniques, which exploit details in waveforms for the benefit of an improved resolution (*Pratt*, 1999; *Chen et al.*, 2007b; *Fichtner et al.*, 2009; *Tape et al.*, 2009). Full waveform ambient noise inversion addresses this limitation and improves the resolution of tomographic images by modeling the full seismic wave propagation physics in 3-D heterogeneous and attenuating media, and by incorporating the distribution of noise sources in space and frequency. For tomographic purposes, correlation functions are averaged over time and it suffices to account for the effective noise source distribution. An extension of the method to also account for the time-variability of noise sources can pave the way for an improved temporal resolution in monitoring studies.

7.7.4 Monitoring with ambient noise

For monitoring purposes repeated sources are required. Since the ambient seismic noise field is present at all times, we can extract correlation functions repeatedly and thus image possible time-lapse changes. This idea has been applied to monitor volcanoes (*Brenguier et al.*, 2008a; *Obermann et al.*, 2013), active faults (*Brenguier et al.*, 2008b; *Obermann et al.*, 2014), geothermal reservoirs (*Hillers et al.*, 2015; *Obermann et al.*, 2015) and hydrocarbon reservoirs (*Bakulin and Calvert*, 2004; *de Ridder and Biondi*, 2013). Before the emergence of ambient noise tomography, such studies were limited to expensive 4-D seismic surveys or to the rare occurrence of earthquake doublets (*Sens-Schönfelder and Brenguier*, 2018). The estimated Green's functions are inevitably affected by the time-variant nature of the noise sources, which pollutes images of potential velocity changes. Apparent velocity variations of 0.25 percent within one day may be induced, which likely mask realistic subsurface changes (*Daskalakis et al.*, 2016; *Delaney et al.*, 2017). To reduce these artifacts, monitoring primarily focuses on multiply scattered waves in seismograms, referred to as coda waves, with the heuristic argument that they are affected less by heterogeneous and non-stationary noise sources (*Hadziioannou et al.*, 2009; *Colombi et al.*, 2014). Nevertheless, either heavy data processing and data selection (*Brenguier et al.*, 2008a; *Obermann et al.*, 2013, 2015; *Hillers et al.*, 2015) or long averaging intervals, typically between 30 and 60 days (*Brenguier et al.*, 2008b; *Meier et al.*, 2010; *Obermann et al.*, 2014) are necessary in order to obtain stable coda waves in correlation functions. While heavy processing changes not only the sensitivity to sources but also to structure (*Fichtner et al.*, 2017), relevant changes in a geothermal or hydrocarbon context are expected on timescales of few hours or days, which cannot be resolved with long averaging intervals. In addition, the localization of weak changes with coda wave interferometry is challenging and the spatial resolution is relatively low (*Kanu and Snieder*, 2015; *Obermann et al.*, 2016). The long and complex travel path of coda waves renders them on the one hand more sensitive to small medium changes compared to direct waves (*Larose and Hall*, 2009). On the other hand, it leads to a complicated averaging of the medium, which is hard to capture physically and difficult to use for localization purposes. Besides a low temporal and spatial resolution, coda wave interferometry is often not an option due to the lack of sufficiently strong scatterers or to high attenuation (e.g. *Mordret et al.*, 2014; *Lindner et al.*, 2018).

Wapenaar et al. (2008) introduced with multi-dimensional deconvolution a new approach to account for heterogeneous noise source distributions. The quality of the retrieved Green's function is improved by deconvolving the cross-correlation function with a so-called point-spread function that captures the illumination pattern of the sources (*Wapenaar and van der Neut*, 2010; *van der Neut et al.*, 2011; *Wapenaar et al.*, 2011a,b). The correction of phase inaccuracies caused by heterogeneous noise source distributions (*van Dalen et al.*, 2015; *Weemstra et al.*, 2017a) may potentially increase the temporal resolution for mon-

itoring purposes. In addition, virtual reflections can be introduced mimicking naturally occurring coda (*Weemstra et al.*, 2017b). However, a major drawback of multi-dimensional deconvolution is that the estimate of the point-spread function and the reflecting boundary condition require a dense receiver layout enclosing the medium of interest. Such a station geometry is hardly ever available or expensive to set up and, additionally, it increases the necessary number of stations substantially.

In summary, noise-based monitoring frequently relies on accurate reconstructions of surfaces waves, but they are significantly biased by the nature of the ambient noise sources. Consistently accounting for heterogeneous and non-stationary noise source distributions in combination with the extraction of waveform information has the potential to increase both temporal and spatial resolution in monitoring studies.

7.7.5 Challenges

A first goal would be to present a data-driven proof of concept for the monitoring based on full waveform ambient noise inversion with an improved temporal and spatial resolution. Incorporating time-variable noise source distributions and adapting the averaging length to the timescale of interest poses several challenges:

(i) There is an inherent trade-off between temporal and spatial resolution and a good balance has to be found. Decreasing the averaging length affects the quality of the data. Unavoidable errors in the inference of the noise source distribution are consequently larger, which in turn leak into tomographic images and vice versa. The quantification of this trade-off that is imposed by the physics of the problem is essential and determines the maximum temporal resolution. Current monitoring techniques that are based on ambient noise do not have the means to investigate this trade-off, since they deceptively render the distribution of noise sources unimportant. The physical model behind our method describes reality more accurately and we will be able to extract more information. Improving both the temporal and spatial resolution is thus feasible while properly accounting for physical limitations. This step is crucial and needs to be done carefully in order to reduce the risk of costly false alarms.

(ii) New ways to identify and extract reliable information have to be found. Averaging correlation functions over long-time intervals typically leads to a smooth average distribution of noise sources and thus to stable correlations that are similar to earthquake recordings. Reducing the averaging length changes the nature of correlations. Signals typically not known from Green's functions appear and vary for different time periods (see section 7.3).

(iii) An accurate way to incorporate the distribution of ambient noise sources for finite domains has to be found (see section 7.2).

(iv) The amount of data to be investigated increases significantly, which leads to scaling issues.

Conclusions 8

With full waveform ambient noise inversion, we developed and applied a novel approach for ambient noise tomography. It is the first interferometric technique that incorporates heterogeneous noise source distributions. A major benefit compared to traditional ambient noise tomography is that we capture the physics of the problem more accurately, not only regarding the distribution of ambient noise sources, but also in terms of seismic wave propagation. Treating correlation functions as self-consistent observables and dropping the principle of Green's function retrieval enables us to extract more information and to quantify inherent source-structure trade-offs.

We worked on various aspects to make full waveform ambient noise more tractable:

- A new formulation of the theory is introduced in chapter 2. It is valid for arbitrary distributions of noise sources in both space and frequency, and for any type of medium, including 3-D elastic, heterogeneous and attenuating media. The use of operators facilitates the application of adjoint techniques and we derive efficient expressions for the calculation of first and also second derivatives. Due to the latter, a resolution analysis that accounts for intra- and inter-parameter trade-offs is possible.

- In a synthetic study in 2-D presented in chapter 3, we investigate the prerequisites for the application of full waveform ambient noise inversion to real data. Based on a forward modeling study, we design and implement an inversion scheme, where the extraction of waveform information is successively increased. A joint inversion for the distribution of noise sources and structure has the potential to go beyond traditional ambient noise tomography and to improve the resolution of tomographic images.

- In chapter 4 we develop a framework for 3-D media with arbitrary distributions of the power-spectral density distribution. It is the indispensable basis for the following chapters and many studies that were previously impossible or tedious are rendered feasible with the new tool.

- For a first use case, we investigate in chapter 5 the emergence of signals in correlation functions in general and in particular of body waves. By studying the sensitivity to global noise sources, we confirm the robustness of traditional ambient noise tomography that is based on surface waves and shed light on the commonly experienced difficulty to observe body waves in correlation functions. We thus advance our understanding of the physics behind correlation functions.
- Designed as a proof of concept study, we invert in chapter 6 a global dataset focusing on the Earth's Hum for the distribution of the power-spectral density and for Earth structure. We validate the source model by *Ermert et al.* (2017) and recover tomographic features known from global Earth models. In addition, we use the new capabilities and update the Collaborative Seismic Earth Model.

Including all the studies that have been conducted following a similar approach and intention, full waveform ambient noise inversion is still in its infancy and further research is required to establish it as a standalone tomographic technique. Some of the challenges are summarized in chapter 7 and more will, for sure, arise on the way.

I hope we could reveal and demonstrate some of the potentials of full waveform ambient noise inversion and that more people will join and accelerate its development with creative ideas and solutions.

References

Afanasiev, M., D. Peter, K. Sager, S. Simutė, L. Ermert, L. Krischer, and A. Fichtner (**2016**), Foundations for a multiscale collaborative Earth model, *Geophys. J. Int.*, *204*(1), 39–58, doi: 10.1093/gji/ggv439.

Afanasiev, M., C. Boehm, M. van Driel, L. Krischer, M. Rietmann, D. A. May, M. G. Knepley, and A. Fichtner (**2019**), Modular and flexible spectral-element waveform modelling in two and three dimensions, *Geophys. J. Int.*, *216*(3), 1675–1692, doi: 10.1093/gji/ggy469.

Agnew, D. C., and J. Berger (**1978**), Vertical seismic noise at very low frequencies, *J. Geophys. Res. Solid Earth*, *83*(B11), 5420–5424, doi: 10.1029/JB083iB11p05420.

Aki, K. (**1957**), Space and time spectra of stationary stochastic waves with special reference to microtremors, *Bull. Earthquake Res. Inst.*, *35*, 415–456.

Aki, K., and P. Richards (**2002**), *Quantitative Seismology*, University Science Books.

Ardhuin, F., E. Stutzmann, M. Schimmel, and A. Mangeney (**2011**), Ocean wave sources of seismic noise, *J. Geophys. Res.: Ocean*, *116*(C9), doi: 10.1029/2011JC006952.

Ardhuin, F., L. Gualtieri, and E. Stutzmann (**2015**), How ocean waves rock the Earth: Two mechanisms explain microseisms with periods 3 to 300 s, *Geophys. Res. Lett.*, *42*(3), 765–772, doi: 10.1002/2014GL062782, 2014GL062782.

Auer, L., L. Boschi, T. W. Becker, T. Nissen-Meyer, and D. Giardini (**2014**), Savani: A variable resolution whole-mantle model of anisotropic shear velocity variations based on multiple data sets, *J. Geophys. Res.: Solid Earth*, *119*(4), 3006–3034, doi: 10.1002/2013JB010773.

Bakulin, A., and R. Calvert (**2004**), Virtual source: New method for imaging and 4D below complex overburden, *74th Annual International Meeting, SEG, Expanded Abstracts*, pp. 2477–2480, doi: 10.1190/1.1845233.

Basini, P., T. Nissen-Meyer, L. Boschi, E. Casarotti, J. Verbeke, O. Schenk, and D. Giardini (**2013**), The influence of nonuniform ambient noise on crustal tomography in Europe, *Geochem. Geophys. Geosys.*, *14*(5), 1471–1492, doi: 10.1002/ggge.20081.

Bassin, C., G. Laske, and G. Masters (**2000**), The current limits of resolution for surface wave tomography in North America, *EOS Trans. AGU*, *81*, F897.

Bensen, G. D., M. H. Ritzwoller, M. P. Barmin, A. L. Levshin, F. Lin, M. P. Moschetti, N. M. Shapiro, and Y. Yang (**2007**), Processing seismic ambient noise data to obtain reliable broad-band surface wave dispersion measurements, *Geophys. J. Int.*, *169*(3), 1239–1260, doi: 10.1111/j.1365-246X.2007.03374.x.

Boehm, C., and A. Fichtner (**2018**), Lazy wave propagation, *Geophys. J. Int.*, *216*(2), 984–990, doi: 10.1093/gji/ggy295.

Bormann, P. (**2012**), *New Manual of Seismological Observatory Practice (NMSOP-2)*, IASPEI, GFZ German Research Centre for Geosciences, Potsdam, doi: 10.2312/GFZ.NMSOP-2.

Boschi, L., B. Fry, G. Ekström, and D. Giardini (**2009**), The European upper mantle as seen by surface waves, *Surveys in Geophysics*, *30*(4), 463–501, doi: 10.1007/s10712-009-9066-2.

Boué, P., P. Poli, M. Campillo, H. Pedersen, X. Briand, and P. Roux (**2013**), Teleseismic correlations of ambient seismic noise for deep global imaging of the Earth, *Geophys. J. Int.*, *194*(2), 844–848, doi: 10.1093/gji/ggt160.

Boué, P., P. Poli, M. Campillo, and P. Roux (**2014**), Reverberations, coda waves and ambient noise: Correlations at the global scale and retrieval of the deep phases, *Earth Planet. Sci. Lett*, *391*, 137–145, doi: 10.1016/j.epsl.2014.01.047.

Bowden, D. C., V. C. Tsai, and F.-C. Lin (**2015**), Site amplification, attenuation, and scattering from noise correlation amplitudes across a dense array in Long Beach, CA, *Geophys. Res. Lett.*, *42*(5), 1360–1367, doi: 10.1002/2014GL062662, 2014GL062662.

Bowden, D. C., V. C. Tsai, and F.-C. Lin (**2017**), Amplification and attenuation across USArray using ambient noise wavefront tracking, *J. Geophys. Res.: Solid Earth*, *122*(12), 10,086–10,101, doi: 10.1002/2017JB014804, 2017JB014804.

Bozdağ, E., D. Peter, M. Lefebvre, J. Tromp, D. Komatitsch, D. Pugmire, J. Hill, and N. Podhorszki (**2016**), Global adjoint tomography: First-generation model, *Geophys. J. Int.*, *207*(3), 1739–1766, doi: 10.1093/gji/ggw356.

Brenguier, F., N. M. Shapiro, M. Campillo, V. Ferrazzini, Z. Duputel, O. Coutant, and A. Nercessian (**2008**a), Towards forecasting volcanic eruptions using seismic noise, *Nat. Geosci.*, *1*, 126–130, doi: 10.1038/ngeo104.

Brenguier, F., M. Campillo, C. Hazıioannou, N. M. Shapiro, R. M. Nadeau, and E. Larose (**2008**b), Postseismic relaxation along the San Andreas fault at Parkfield from continuous seismological observations, *Science*, *321*(5895), 1478–1481, doi: 10.1126/science.1160943.

Bromirski, P. D., and P. Gerstoft (**2009**), Dominant source regions of the Earth's "hum" are coastal, *Geophys. Res. Lett.*, *36*(13), doi: 10.1029/2009GL038903.

Campillo, M., and A. Paul (**2003**), Long-range correlations in the diffuse seismic coda, *Science*, *299*(5606), 547–549, doi: 10.1126/science.1078551.

Castellanos, J. C., R. W. Clayton, and X. Pérez-Campos (**2018**), Imaging the eastern Trans-Mexican Volcanic Belt with ambient seismic noise: Evidence for a slab tear, *J. Geophys. Res.: Solid Earth*, *123*(9), 7741–7759, doi: 10.1029/2018JB015783.

Chen, M., H. Huang, H. Yao, R. van der Hilst, and F. Niu (**2014**), Low wave speed zones in the crust beneath SE Tibet revealed by ambient noise adjoint tomography, *Geophys. Res. Lett.*, *41*(2), 334–340, doi: 10.1002/2013GL058476.

Chen, P., L. Zhao, and T. H. Jordan (**2007**a), Full 3D tomography for the crustal structure of the Los Angeles region., *Bull. Seismol. Soc. Am.*, *97*(4), 1094–1120, doi: 10.1785/0120060222.

Chen, P., T. H. Jordan, and L. Zhao (**2007**b), Full 3D waveform tomography: A comparison between the scattering-integral and adjoint-wavefield methods, *Geophys. J. Int.*, *170*(1), 175–181, doi: 10.1111/j.1365-246X.2007.03429.x.

Claerbout, J. F. (**1968**), Synthesis of a layered medium from its acoustic transmission response, *Geophysics*, *33*(2), 264–269, doi: 10.1190/1.1439927.

Clayton, R. W. (**2018**), Imaging the subsurface with ambient noise autocorrelations, *SEG Technical Program Expanded Abstracts*, pp. 4852–4856, doi: 10.1190/segam2018-2978420.1.

Colombi, A., J. Chaput, F. Brenguier, G. Hillers, P. Roux, and M. Campillo (**2014**), On the temporal stability of the coda of ambient noise correlations, *Comptes Rendus Geoscience*, *346*(11), 307–316, doi: 10.1016/j.crte.2014.10.002.

Coughlin, M., J. Harms, D. C. Bowden, P. Meyers, V. C. Tsai, V. Mandic, G. Pavlis, and T. Prestegard (**2019**), Coherence-based approaches for estimating the composition of the seismic wavefield, *J. Geophys. Res.: Solid Earth*, *124*(3), 2941–2956, doi: 10.1029/2018JB016608.

Cupillard, P., and Y. Capdeville (**2010**), On the amplitude of surface waves obtained by noise correlation and the capability to recover the attenuation: A numerical approach, *Geophys. J. Int.*, *181*(3), 1687–1700, doi: 10.1111/j.1365-246X.2010.04586.x.

Dahlen, F., S.-H. Hung, and G. Nolet (**2000**), Fréchet kernels for finite-frequency traveltimes – I. Theory, *Geophys. J. Int.*, *141*, 157–174, doi: 10.1046/j.1365-246X.2000.00070.x.

Dahlen, F. A., and F. A. Baig (**2002**), Fréchet kernels for body wave amplitudes, *Geophys. J. Int.*, *150*, 440–466, doi: 10.1046/j.1365-246X.2002.01718.x.

Dantas, O. A. B., A. F. do Nascimento, and M. Schimmel (**2018**), Retrieval of body-wave reflections using ambient noise interferometry using a small-scale experiment, *Pure and Applied Geophysics*, doi: 10.1007/s00024-018-1794-0.

Daskalakis, E., C. Evangelidis, J. Garnier, N. Melis, G. Papanicolaou, and C. Tsogka (**2016**), Robust seismic velocity change estimation using ambient noise recordings, *Geophys. J. Int.*, *205*(3), 1926–1936, doi: 10.1093/gji/ggw142.

de Ridder, S. A. L., and B. L. Biondi (**2013**), Daily reservoir-scale subsurface monitoring using ambient seismic noise, *Geophys. Res. Lett.*, *40*(12), 2969–2974, doi: 10.1002/grl.50594.

de Ridder, S. A. L., and J. R. Maddison (**2018**), Full wavefield inversion of ambient seismic noise, *Geophys. J. Int.*, *215*(2), 1215–1230, doi: 10.1093/gji/ggy328.

Deen, M., E. Stutzmann, and F. Ardhuin (**2018**), The Earth's Hum variations from a global model and seismic recordings around the Indian Ocean, *Geochem. Geophys. Geosys.*, *19*(10), 4006–4020, doi: 10.1029/2018GC007478.

Delaney, E., L. Ermert, K. Sager, A. Kritski, S. Bussat, and A. Fichtner (**2017**), Passive seismic monitoring with nonstationary noise sources, *Geophysics*, *82*(4), KS57–KS70, doi: 10.1190/geo2016-0330.1.

Díaz, J. (**2016**), On the origin of the signals observed across the seismic spectrum, *Earth-Science Reviews*, *161*, 224 – 232, doi: 10.1016/j.earscirev.2016.07.006.

Draganov, D., K. Wapenaar, W. Mulder, J. Singer, and A. Verdel (**2007**), Retrieval of reflections from seismic background-noise measurements, *Geophys. Res. Lett.*, *34*(4), doi: 10.1029/2006GL028735, l04305.

Draganov, D., X. Campman, J. Thorbecke, A. Verdel, and K. Wapenaar (**2009**), Reflection images from ambient seismic noise, *Geophysics*, *74*(5), A63–A67, doi: 10.1190/1.3193529.

Draganov, D., X. Campman, J. Thorbecke, A. Verdel, and K. Wapenaar (**2013**), Seismic exploration-scale velocities and structure from ambient seismic noise (> 1 Hz), *J. Geophys. Res.: Solid Earth*, *118*(8), 4345–4360, doi: 10.1002/jgrb.50339.

Dziewoński, A. M., and D. L. Anderson (**1981**), Preliminary reference Earth model, *Phys. Earth Planet. Inter.*, *25*(4), 297–356, doi: 10.1016/0031-9201(81)90046-7.

Einstein, A. (**1906**), Zur Theorie der Brownschen Bewegung, *Ann. der Phys.*, *4*(19), 371–381, doi: 10.1002/andp.19063240208.

Ermert, L., A. Villaseñor, and A. Fichtner (**2016**), Cross-correlation imaging of ambient noise sources, *Geophys. J. Int.*, *204*(1), 347, doi: 10.1093/gji/ggv460.

Ermert, L., K. Sager, M. Afanasiev, C. Boehm, and A. Fichtner (**2017**), Ambient seismic source inversion in a heterogeneous Earth: Theory and application to the Earth's Hum, *J. Geophys. Res.: Solid Earth*, *122*(11), 9184–9207, doi: 10.1002/2017JB014738, 2017JB014738.

Ermert, L., K. Sager, T. Nissen-Meyer, and A. Fichtner (**20xx**), Frequency-dependent ambient seismic source inversion, in preparation.

Farra, V., E. Stutzmann, L. Gualtieri, M. Schimmel, and F. Ardhuin (**2016**), Ray-theoretical modeling of secondary microseism P waves, *Geophys. J. Int.*, *206*(3), 1730–1739, doi: 10.1093/gji/ggw242.

Fichtner, A. (**2010**), *Full Seismic Waveform Modelling and Inversion.*, Springer, Heidelberg, doi: 10.1007/978-3-642-15807-0.

Fichtner, A. (**2014**), Source and processing effects on noise correlations, *Geophys. J. Int.*, *197*, 1527–1531, doi: 10.1093/gji/ggu093.

Fichtner, A. (**2015**), Source-structure trade-offs in ambient noise correlations, *Geophys. J. Int.*, *202*(1), 678, doi: 10.1093/gji/ggv182.

Fichtner, A., and J. Trampert (**2011**), Hessian kernels of seismic data functionals based upon adjoint techniques, *Geophys. J. Int.*, *185*(2), 775–798, doi: 10.1111/j.1365-246X.2011.04966.x.

Fichtner, A., and A. Villaseñor (**2015**), Crust and upper mantle of the western Mediterranean – Constraints from full-waveform inversion, *Earth Planet. Sci. Lett.*, *428*, 52–62, doi: 10.1016/j.epsl.2015.07.038.

Fichtner, A., H.-P. Bunge, and H. Igel (**2006**), The adjoint method in seismology - I. Theory, *Phys. Earth Planet. Inter.*, *157*, 86–104, doi: 10.1016/j.pepi.2006.03.016.

Fichtner, A., B. L. N. Kennett, H. Igel, and H.-P. Bunge (**2008**), Theoretical background for continental- and global-scale full-waveform inversion in the time-frequency domain., *Geophys. J. Int.*, *175*(2), 665–685, doi: 10.1111/j.1365-246X.2008.03923.x.

Fichtner, A., B. L. N. Kennett, H. Igel, and H.-P. Bunge (**2009**), Full seismic waveform tomography for upper-mantle structure in the Australasian region using adjoint methods., *Geophys. J. Int.*, *179*(3), 1703–1725, doi: 10.1111/j.1365-246X.2009.04368.x.

Fichtner, A., E. Saygin, T. Taymaz, P. Cupillard, Y. Capdeville, and J. Trampert (**2013**), The deep structure of the North Anatolian Fault Zone, *Earth Planet. Sci. Lett.*, *373*, 109–117, doi: 10.1016/j.epsl.2013.04.027.

Fichtner, A., L. Stehly, L. Ermert, and C. Boehm (**2017**), Generalized interferometry – I: Theory for interstation correlations, *Geophys. J. Int.*, *208*(2), 603, doi: 10.1093/gji/ggw420.

Fichtner, A., D.-P. van Herwaarden, M. Afanasiev, S. Simutė, L. Krischer, Y. Çubuk Sabuncu, T. Taymaz, L. Colli, E. Saygin, A. Villaseñor, J. Trampert, P. Cupillard, H.-P. Bunge, and H. Igel (**2018**), The Collaborative Seismic Earth Model: Generation 1, *Geophys. Res. Lett.*, *45*(9), 4007–4016, doi: 10.1029/2018GL077338.

Forghani, F., and R. Snieder (**2010**), Underestimation of body waves and feasibility of surface-wave reconstruction by seismic interferometry, *The Leading Edge*, *29*(7), 790–794, doi: 10.1190/1.3462779.

French, S. W., and B. A. Romanowicz (**2014**), Whole-mantle radially anisotropic shear velocity structure from spectral-element waveform tomography, *Geophys. J. Int.*, *199*(3), 1303–1327, doi: 10.1093/gji/ggu334.

Froment, B., M. Campillo, P. Roux, P. Gouédard, A. Verdel, and R. L. Weaver (**2010**), Estimation of the effect of nonisotropically distributed energy on the apparent arrival time in correlations, *Geophysics*, *75*(5), SA85–SA93, doi: 10.1190/1.3483102.

Fukao, Y., K. Nishida, and N. Kobayashi (**2010**), Seafloor topography, ocean infragravity waves, and background Love and Rayleigh waves, *J. Geophys. Res.: Solid Earth*, *115*(B4), doi: 10.1029/2009JB006678.

Gal, M., A. M. Reading, S. P. Ellingsen, L. Gualtieri, K. D. Koper, R. Burlacu, H. Tkalčić, and M. A. Hemer (**2015**), The frequency dependence and locations of short-period microseisms generated in the Southern Ocean and West Pacific, *J. Geophys. Res.: Solid Earth*, *120*(8), 5764–5781, doi: 10.1002/2015JB012210, 2015JB012210.

Gerstoft, P., M. C. Fehler, and K. G. Sabra (**2006**), When Katrina hit California, *Geophys. Res. Lett.*, *33*(17), doi: 10.1029/2006GL027270, L17308.

Gerstoft, P., P. M. Shearer, N. Harmon, and J. Zhang (**2008**), Global P, PP, and PKP wave microseisms observed from distant storms, *Geophys. Res. Lett.*, *35*(23), doi: 10.1029/2008GL036111, L23306.

Gizon, L., and A. C. Birch (**2002**), Time-distance helioseismology: The forward problem for random distributed sources, *Astrophys. J.*, *571*(2), 966, doi: 10.1086/340015.

Gorbatov, A., B. L. N. Kennett, and E. Saygin (**2012**), Crustal properties from seismic station autocorrelograms, *Geophys. J. Int.*, *192*(2), 861–870, doi: 10.1093/gji/ggs064.

Green, R. G., K. F. Priestley, and R. S. White (**2017**), Ambient noise tomography reveals upper crustal structure of Icelandic rifts, *Earth Planet. Sci. Lett*, *466*, 20–31, doi: 10.1016/j.epsl.2017.02.039.

Griewank, A. (**1992**), Achieving logarithmic growth of temporal and spatial complexity in reverse automatic differentiation, *Optimization Methods and Software*, *1*(1), 35–54, doi: 10.1080/10556789208805505.

Groos, J. C., S. Bussat, and J. R. R. Ritter (**2012**), Performance of different processing schemes in seismic noise cross-correlations, *Geophys. J. Int.*, *188*(2), 498–512, doi: 10.1111/j.1365-246X.2011.05288.x.

Gualtieri, L., E. Stutzmann, Y. Capdeville, F. Ardhuin, A. M. M. Schimmel, and A. Morelli (**2013**), Modeling secondary microseismic noise by normal mode summation, *Geophys. J. Int.*, *193*(3), 1732–1745, doi: 10.1093/gji/ggt090.

Gualtieri, L., E. Stutzmann, V. Farra, Y. Capdeville, M. Schimmel, F. Ardhuin, and A. Morelli (**2014**), Modelling the ocean site effect on seismic noise body waves, *Geophys. J. Int.*, *197*(2), 1096–1106, doi: 10.1093/gji/ggu042.

Hadziioannou, C., E. Larose, O. Coutant, P. Roux, and M. Campillo (**2009**), Stability of monitoring weak changes in multiply scattering media with ambient noise correlation: Laboratory experiments, *J. Acoust. Soc. Am.*, *125*(6), 3688–3695, doi: 10.1121/1.3125345.

Halliday, D., and A. Curtis (**2008**), Seismic interferometry, surface waves and source distribution, *Geophys. J. Int.*, *175*, 1067–1087, doi: 10.1111/j.1365-246X.2008.03918.x.

Hanasoge, S. M. (**2013**), The influence of noise sources on cross-correlation amplitudes, *Geophys. J. Int.*, *192*(1), 295–309, doi: 10.1093/gji/ggs015.

Hanasoge, S. M. (**2014**), Measurements and kernels for source-structure inversions in noise tomography, *Geophys. J. Int.*, *192*(2), 971–985, doi: 10.1093/gji/ggt411.

Hanasoge, S. M., A. Birch, L. Gizon, and J. Tromp (**2011**), The adjoint method applied to time-distance helioseismology, *Astrophys. J.*, *738*(1), 100, doi: 10.1088/0004-637x/738/1/100.

Haned, A., E. Stutzmann, M. Schimmel, S. Kiselev, A. Davaille, and A. Yelles-Chaouche (**2016**), Global tomography using seismic hum, *Geophys. J. Int.*, *204*(2), 1222, doi: 10.1093/gji/ggv516.

Hansen, P. C. (**1992**), Analysis of discrete ill-posed problems by means of the L-curve, *SIAM Review*, *34*(4), 561–580, doi: 10.1137/1034115.

Harmon, N., C. Rychert, and P. Gerstoft (**2010**), Distribution of noise sources for seismic interferometry, *Geophys. J. Int.*, *183*(3), 1470–1484, doi: 10.1111/j.1365-246X.2010.04802.x.

Hasselmann, K. (**1963**), A statistical analysis of the generation of microseisms, *Reviews of Geophysics*, *1*(2), 177–210, doi: 10.1029/RG001i002p00177.

Hillers, G., and Y. Ben-Zion (**2011**), Seasonal variations of observed noise amplitudes at 2–18 Hz in southern California, *Geophys. J. Int.*, *184*(2), 860–868, doi: 10.1111/j.1365-246X.2010.04886.x.

Hillers, G., S. Husen, A. Obermann, T. Planès, E. Larose, and M. Campillo (**2015**), Noise-based monitoring and imaging of aseismic transient deformation induced by the 2006 Basel reservoir stimulation, *Geophysics*, *80*(4), KS51, doi: 10.1190/geo2014-0455.1.

Hosseini, K., K. J. Matthews, K. Sigloch, G. E. Shephard, M. Domeier, and M. Tsekhmistrenko (**2018**), SubMachine: Web-Based tools for exploring seismic tomography and other models of Earth's deep interior, *Geochem. Geophys. Geosys.*, *19*(5), 1464–1483, doi: 10.1029/2018GC007431.

Igel, H., and O. Gudmundsson (**1997**), Frequency-dependent effects on travel times and waveforms of long-period S and SS waves, *Phys. Earth. Planet. Int.*, *104*(1), 229–246, doi: 10.1016/S0031-9201(97)00051-4.

International Energy Agency (**2011**), Technology roadmap: Geothermal heat and power, *Tech. rep.*, OECD/IEA, Paris Cedex, France.

Juretzek, C., and C. Hadziioannou (**2016**), Where do ocean microseisms come from? A study of Love-to-Rayleigh wave ratios, *J. Geophys. Res.: Solid Earth*, *121*(9), 6741–6756, doi: 10.1002/2016JB013017.

Kanu, C., and R. Snieder (**2015**), Time-lapse imaging of a localized weak change with multiply scattered waves using numerical-based sensitivity kernel, *J. Geophys. Res.: Solid Earth*, *120*(8), 5595–5605, doi: 10.1002/2015JB011871.

Kimman, W., and J. Trampert (**2010**), Approximations in seismic interferometry and their effects on surface waves, *Geophys. J. Int.*, *182*(1), 461–476, doi: 10.1111/j.1365-246X.2010.04632.x.

Komatitsch, D., and J. Tromp (**2002**a), Spectral-element simulations of global seismic wave propagation, Part I: Validation, *Geophys. J. Int.*, *149*(2), 390–412, doi: 10.1046/j.1365-246X.2002.01653.x.

Komatitsch, D., and J. Tromp (**2002**b), Spectral-element simulations of global seismic wave propagation, Part II: 3-D models, oceans, rotation, and gravity, *Geophys. J. Int.*, *150*(1), 303–318, doi: 10.1046/j.1365-246X.2002.01716.x.

Kraft, T., P. M. Mai, S. Wiemer, N. Deichmann, J. Ripperger, P. Kästli, C. Bachmann, D. Fäh, J. Wössner, and D. Giardini (**2009**), Enhanced geothermal systems: Mitigating risk in urban areas, *Eos, Transactions American Geophysical Union*, *90*(32), 273–274, doi: 10.1029/2009EO320001.

Krischer, L., T. Megies, R. Barsch, M. Beyreuther, T. Lecocq, C. Caudron, and J. Wassermann (**2015**), ObsPy: A bridge for seismology into the scientific Python ecosystem, *Computational Science & Discovery*, *8*(1), 014003, doi: 10.1088/1749-4699/8/1/014003.

Krischer, L., A. Fichtner, C. Boehm, and H. Igel (**2018**), Automated large-scale full seismic waveform inversion for North America and the North Atlantic, *J. Geophys. Res.: Solid Earth*, *123*(7), 5902–5928, doi: 10.1029/2017JB015289.

Kurrle, D., and R. Widmer-Schnidrig (**2008**), The horizontal hum of the Earth: A global background of spheroidal and toroidal modes, *Geophysical Research Letters*, *35*(6), doi: 10.1029/2007GL033125.

Landès, M., F. Hubans, N. M. Shapiro, A. Paul, and M. Campillo (**2010**), Origin of deep ocean microseisms by using teleseismic body waves, *J. Geophys. Res.: Solid Earth*, *115*(B5), doi: 10.1029/2009JB006918, B05302.

Larose, E., and S. Hall (**2009**), Monitoring stress related velocity variation in concrete with a 2x10-5 relative resolution using diffuse ultrasound, *J. Acoust. Soc. Am.*, *125*(4), 1853–1856, doi: 10.1121/1.3079771.

Laske, G., G. Masters, Z. Ma, and M. Pasyanos (**2013**), Update on CRUST1.0 - A 1-degree global model of Earth's crust, in *EGU General Assembly Conference Abstracts*, *EGU General Assembly Conference Abstracts*, vol. 15, pp. EGU2013–2658.

Lebedev, S., and A. J. Schaeffer (**2013**), Global shear speed structure of the upper mantle and transition zone, *Geophys. J. Int.*, *194*(1), 417–449, doi: 10.1093/gji/ggt095.

Lin, F.-C., and V. C. Tsai (**2013**), Seismic interferometry with antipodal station pairs, *Geophys. Res. Lett.*, *40*(17), 4609–4613, doi: 10.1002/grl.50907.

Lin, F.-C., V. C. Tsai, and M. H. Ritzwoller (**2012**), The local amplification of surface waves: A new observable to constrain elastic velocities, density, and anelastic attenuation, *J. Geophys. Res.: Solid Earth*, *117*(B6), doi: 10.1029/2012JB009208, b06302.

Lin, F.-C., V. C. Tsai, B. Schmandt, Z. Duputel, and Z. Zhan (**2013**), Extracting seismic core phases with array interferometry, *Geophys. Res. Lett.*, *40*(6), 1049–1053, doi: 10.1002/grl.50237.

Lindner, F., C. Weemstra, F. Walter, and C. Hadziioannou (**2018**), Towards monitoring the englacial fracture state using virtual-reflector seismology, *Geophys. J. Int.*, *214*(2), 825–844, doi: 10.1093/gji/ggy156.

Liu, Q., K. D. Koper, R. Burlacu, S. Ni, F. Wang, C. Zou, Y. Wei, M. Gal, and A. M. Reading (**2016**), Source locations of teleseismic P, SV, and SH waves observed in microseisms recorded by a large aperture seismic array in China, *Earth Planet. Sci. Lett*, *449*, 39–47, doi: 10.1016/j.epsl.2016.05.035.

Lobkis, O. I., and R. L. Weaver (**2001**), On the emergence of the Green's function in the correlations of a diffuse field, *J. Acoust. Soc. Am.*, *110*(6), 3011–3017, doi: 10.1121/1.1417528.

Longuet-Higgins, M. S. (**1950**), A theory of the origin of microseisms, *Phil. Trans. Roy. Soc. Lon.*, *243*(857), 1–35, doi: 10.1098/rsta.1950.0012.

Lu, Y., L. Stehly, A. Paul, and A. W. Group (**2018**), High-resolution surface wave tomography of the European crust and uppermost mantle from ambient seismic noise, *Geophys. J. Int.*, *214*(2), 1136–1150, doi: 10.1093/gji/ggy188.

Luo, Y., and G. T. Schuster (**1991**), Wave-equation traveltime inversion., *Geophysics*, *56*(5), 645–653, doi: 10.1190/1.1443081.

Meier, U., N. M. Shapiro, and F. Brenguier (**2010**), Detecting seasonal variations in seismic velocities within Los Angeles basin from correlations of ambient seismic noise, *Geophys. J. Int.*, *181*(2), 985–996, doi: 10.1111/j.1365-246X.2010.04550.x.

Mordret, A., S. N. M., and S. Singh (**2014**), Seismic noise-based time-lapse monitoring of the Valhall overburden, *Geophys. Res. Lett.*, *41*(14), 4945–4952, doi: 10.1002/2014GL060602.

Mordret, A., D. Rivet, M. Landès, and N. M. Shapiro (**2015**), Three-dimensional shear velocity anisotropic model of Piton de la Fournaise Volcano (La Réunion Island) from ambient seismic noise, *J. Geophys. Res.: Solid Earth*, *120*(1), 406–427, doi: 10.1002/2014JB011654.

Nakata, N., J. P. Chang, J. F. Lawrence, and P. Boué (**2015**), Body wave extraction and tomography at Long Beach, California, with ambient-noise interferometry, *J. Geophys. Res.: Solid Earth*, *120*(2), 1159–1173, doi: 10.1002/2015JB011870, 2015JB011870.

Nishida, K. (**2013**), Global propagation of body waves revealed by cross-correlation analysis of seismic hum, *Geophys. Res. Lett.*, *40*(9), 1691–1696, doi: 10.1002/grl.50269.

Nishida, K. (**2014**), Source spectra of seismic hum, *Geophys. J. Int.*, *199*(1), 416–429, doi: 10.1093/gji/ggu272.

Nishida, K., and N. Kobayashi (**1999**), Statistical features of Earth's continuous free oscillations, *J. Geophys. Res. Solid Earth*, *104*(B12), 28741–28750, doi: 10.1029/1999JB900286.

Nishida, K., and R. Takagi (**2016**), Teleseismic S wave microseisms, *Science*, *353*(6302), 919–921, doi: 10.1126/science.aaf7573.

Nishida, K., N. Kobayashi, and Y. Fukao (**2000**), Resonant oscillations between the solid Earth and the atmosphere, *Science*, *287*(5461), 2244–2246, doi: 10.1126/science.287.5461.2244.

Nishida, K., H. Kawakatsu, Y. Fukao, and K. Obara (**2008**), Background Love and Rayleigh waves simultaneously generated at the Pacific Ocean floors, *Geophys. Res. Lett.*, *35*(16), doi: 10.1029/2008GL034753.

Nishida, K., J.-P. Montagner, and H. Kawakatsu (**2009**), Global surface wave tomography using seismic hum, *Science*, *326*(5949), 112, doi: 10.1126/science.1176389.

Nocedal, J., and S. Wright (**2006**), *Numerical Optimization*, Springer Science & Business Media, doi: 10.1007/978-0-387-40065-5.

Obermann, A., T. Planès, E. Larose, and M. Campillo (**2013**), Imaging preeruptive and coeruptive structural and mechanical changes of a volcano with ambient seismic noise, *J. Geophys. Res.: Solid Earth*, *118*(12), 6285–6294, doi: 10.1002/2013JB010399.

Obermann, A., B. Froment, M. Campillo, E. Larose, T. Planès, B. Valette, J. H. Chen, and Q. Y. Liu (**2014**), Seismic noise correlations to image structural and mechanical changes associated with the Mw 7.9 2008 Wenchuan earthquake, *J. Geophys. Res.: Solid Earth*, *119*(4), 3155–3168, doi: 10.1002/2013JB010932.

Obermann, A., T. Kraft, E. Larose, and S. Wiemer (**2015**), Potential of ambient seismic noise techniques to monitor the St. Gallen geothermal site (Switzerland), *J. Geophys. Res.: Solid Earth*, *120*(6), 4301–4316, doi: 10.1002/2014JB011817.

Obermann, A., T. Planès, C. Hadziioannou, and M. Campillo (**2016**), Lapse-time-dependent coda-wave depth sensitivity to local velocity perturbations in 3-D heterogeneous elastic media, *Geophys. J. Int.*, *207*(1), 59–66, doi: 10.1093/gji/ggw264.

Olivier, G., F. Brenguier, M. Campillo, R. Lynch, and P. Roux (**2015**), Body-wave reconstruction from ambient seismic noise correlations in an underground mine, *Geophysics*, *80*(3), KS11–KS25, doi: 10.1190/geo2014-0299.1.

Panea, I., D. Draganov, C. A. Vidal, and V. Mocanu (**2014**), Retrieval of reflections from ambient noise recorded in the Mizil area, Romania, *Geophysics*, *79*(3), Q31–Q42, doi: 10.1190/geo2013-0292.1.

Pederson, J. (**1993**), Observations and modeling of seismic background noise, *USGS Open-File Report*, pp. 93–322, doi: 10.3133/ofr93322.

Peter, D., C. Tape, L. Boschi, and J. H. Woodhouse (**2007**), Surface wave tomography: Global membrane waves and adjoint methods, *Geophys. J. Int.*, *171*(3), 1098, doi: 10.1111/j.1365-246X.2007.03554.x.

Peter, D., D. Komatitsch, Y. Luo, R. Martin, N. Le Goff, E. Casarotti, P. Le Loher, F. Magnoni, Q. Liu, C. Blitz, T. Nissen-Meyer, P. Basini, and J. Tromp (**2011**), Forward and adjoint simulations of seismic wave propagation on fully unstructured hexahedral meshes, *Geophys. J. Int.*, *186*(2), 721–739, doi: 10.1111/j.1365-246X.2011.05044.x.

Plessix, R.-E. (**2006**), A review of the adjoint-state method for computing the gradient of a functional with geophysical applications, *Geophys. J. Int.*, *167*, 495–503, doi: 10.1111/j.1365-246X.2006.02978.x.

Poli, P., H. A. Pedersen, and M. Campillo (**2012**a), Emergence of body waves from cross-correlation of short period seismic noise, *Geophys. J. Int.*, *188*(2), 549–558, doi: 10.1111/j.1365-246X.2011.05271.x.

Poli, P., M. Campillo, and H. Pedersen (**2012**b), Body-wave imaging of Earth's mantle discontinuities from ambient seismic noise, *Science*, *338*(6110), 1063–1065, doi: 10.1126/science.1228194.

Poli, P., M. Campillo, and M. de Hoop (**2017**), Analysis of intermediate period correlations of coda from deep earthquakes, *Earth Planet. Sci. Lett*, *477*, 147 – 155, doi: 10.1016/j.epsl.2017.08.026.

Pratt, R. G. (**1999**), Seismic waveform inversion in the frequency domain, part 1: Theory and verification in a physical scale model., *Geophysics*, *64*(3), 888–901, doi: 10.1190/1.1444597.

Prieto, G. A., M. Denolle, J. F. Lawrence, and G. C. Beroza (**2011**), On amplitude information carried by the ambient seismic field, *Comptes Rendus Geoscience*, *343*(8–9), 600 – 614, doi: 10.1016/j.crte.2011.03.006.

Retailleau, L., P. Boué, L. Stehly, and M. Campillo (**2017**), Locating microseism sources using spurious arrivals in intercontinental noise correlations, *J. Geophys. Res.: Solid Earth*, *122*(10), 8107–8120, doi: 10.1002/2017JB014593.

Retailleau, L., M. Landès, L. Gualtieri, N. M. Shapiro, M. Campillo, P. Roux, and J. Guilbert (**2018**), Detection and analysis of a transient energy burst with beamforming of multiple teleseismic phases, *Geophys. J. Int.*, *212*(1), 14–24, doi: 10.1093/gji/ggx410.

Rhie, J., and B. Romanowicz (**2004**), Excitation of Earth's continuous free oscillations by atmosphere–ocean–seafloor coupling, *Nature*, *431*(7008), 552–556, doi: 10.1038/nature02942.

Rhie, J., and B. Romanowicz (**2006**), A study of the relation between ocean storms and the Earth's hum, *Geochem. Geophys. Geosys.*, *7*(10), doi: 10.1029/2006GC001274.

Rind, D., and W. L. Down (**1979**), Microseisms at Palisades: 2. Rayleigh wave and Love wave characteristics and the geologic control of propagation, *J. Geophys. Res.: Solid Earth*, *84*(B10), 5632–5642, doi: 10.1029/JB084iB10p05632.

Ritsema, J., and H. J. van Heijst (**2002**), Constraints on the correlation of P- and S-wave velocity heterogeneity in the mantle from P, PP, PPP and PKPab traveltimes, *Geophys. J. Int.*, *149*(2), 482–489, doi: 10.1046/j.1365-246X.2002.01631.x.

Ritsema, J., H. J. van Heijst, and J. H. Woodhouse (**1999**), Complex shear wave velocity structure imaged beneath Africa and Iceland, *Science*, *286*(5446), 1925–1928, doi: 10.1126/science.286.5446.1925.

Ritsema, J., A. Deuss, H. J. van Heijst, and J. H. Woodhouse (**2011**), S40RTS: A degree-40 shear-velocity model for the mantle from new Rayleigh wave dispersion, teleseismic traveltime and normal-mode splitting function measurements, *Geophys. J. Int.*, *184*(3), 1223–1236, doi: 10.1111/j.1365-246X.2010.04884.x.

Romero, P., and M. Schimmel (**2018**), Mapping the basement of the Ebro Basin in Spain with seismic ambient noise autocorrelations, *J. Geophys. Res.: Solid Earth*, *123*(6), 5052–5067, doi: 10.1029/2018JB015498.

Rost, S., and C. Thomas (**2002**), Array seismology: Methods and applications, *Reviews of Geophysics*, *40*(3), 2–1–2–27, doi: 10.1029/2000RG000100.

Roux, P., K. G. Sabra, P. Gerstoft, W. A. Kuperman, and M. C. Fehler (**2005**a), P-waves from cross-correlation of seismic noise, *Geophys. Res. Lett.*, *32*(19), doi: 10.1029/2005GL023803, l19303.

Roux, P., K. G. Sabra, W. A. Kuperman, and A. Roux (**2005**b), Ambient noise cross correlation in free space: Theoretical approach, *J. Acoust. Soc. Am.*, *117*(1), 79–84, doi: 10.1121/1.1830673.

Ruigrok, E., D. Draganov, and K. Wapenaar (**2008**), Global-scale seismic interferometry: Theory and numerical examples, *Geophysical Prospecting*, *56*(3), 395–417, doi: 10.1111/j.1365-2478.2008.00697.x.

Ruigrok, E., X. Campman, and K. Wapenaar (**2011**), Extraction of P-wave reflections from microseisms, *Comptes Rendus Geoscience*, *343*(8), 512 – 525, doi: 10.1016/j.crte.2011.02.006.

Sabra, K. G., P. Gerstoft, P. Roux, W. A. Kuperman, and M. C. Fehler (**2005**a), Extracting time-domain Green's function estimates from ambient seismic noise, *Geophys. Res. Lett.*, *32*(3), doi: 10.1029/2004GL021862, l03310.

Sabra, K. G., P. Gerstoft, P. Roux, W. A. Kuperman, and M. C. Fehler (**2005**b), Surface wave tomography from microseisms in Southern California, *Geophys. Res. Lett.*, *32*(14), doi: 10.1029/2005GL023155.

Sadeghisorkhani, H., O. Gudmundsson, R. Roberts, and A. Tryggvason (**2017**), Velocity-measurement bias of the ambient noise method due to source directivity: A case study for the Swedish National Seismic Network, *Geophys. J. Int.*, *209*(3), 1648–1659, doi: 10.1093/gji/ggx115.

Saito, T. (**2010**), Love-wave excitation due to the interaction between a propagating ocean wave and the sea-bottom topography, *Geophys. J. Int.*, *182*(3), 1515–1523, doi: 10.1111/j.1365-246X.2010.04695.x.

Sánchez-Sesma, F. J., and M. Campillo (**2006**), Retrieval of the Green's function from cross correlation: The canonical elastic problem, *Bull. Seis. Soc. Am.*, *96*(3), 1182–1191, doi: 10.1785/0120050181.

Schimmel, M., E. Stutzmann, and J. Gallart (**2011**), Using instantaneous phase coherence for signal extraction from ambient noise data at a local to a global scale, *Geophys. J. Int.*, *184*(1), 494–506, doi: 10.1111/j.1365-246X.2010.04861.x.

Schulte-Pelkum, V., P. S. Earle, and F. L. Vernon (**2004**), Strong directivity of ocean-generated seismic noise, *Geochem. Geophys. Geosys.*, *5*(3), doi: 10.1029/2003GC000520, q03004.

Sens-Schönfelder, C., and F. Brenguier (**2018**), Noise-based monitoring, in *Seismic Ambient Noise*, edited by N. Nakata, L. Gualtieri, and A. Fichtner, p. 267–301, Cambridge University Press, Cambridge, UK, doi: 10.1017/9781108264808.011.

Shapiro, N. M., and M. Campillo (**2004**), Emergence of broadband Rayleigh waves from correlations of the ambient seismic noise, *Geophys. Res. Lett.*, *31*(7), doi: 10.1029/2004GL019491, L07614.

Shapiro, N. M., M. Campillo, L. Stehly, and M. Ritzwoller (**2005**), High resolution surface wave tomography from ambient seismic noise, *Science*, *307*(5715), 1615–1618, doi: 10.1126/science.1108339.

Sheng, Y., N. Nakata, and G. C. Beroza (**2018**), On the nature of higher-order ambient seismic field correlations, *J. Geophys. Res.: Solid Earth*, *123*(9), 7969–7982, doi: 10.1029/2018JB015937.

Simmons, N. A., A. M. Forte, L. Boschi, and S. P. Grand (**2010**), GyPSuM: A joint tomographic model of mantle density and seismic wave speeds, *J. Geophys. Res.: Solid Earth*, *115*(B12), doi: 10.1029/2010JB007631.

Simutė, S., H. Steptoe, L. Cobden, A. Gokhberg, and A. Fichtner (**2016**), Full-waveform inversion of the Japanese Islands region, *J. Geophys. Res.: Solid Earth*, *121*(5), 3722–3741, doi: 10.1002/2016JB012802, 2016JB012802.

Snieder, R. (**2004**), Extracting the Green's function from the correlation of coda waves: A derivation based on stationary phase, *Phys. Rev. E*, *69*, 046610, doi: 10.1103/PhysRevE.69.046610.

Snieder, R. (**2007**), Extracting the Green's function of attenuating heterogeneous acoustic media from uncorrelated waves, *J. Acoust. Soc. Am.*, *121*(5), 2637–2643, doi: 10.1121/1.2713673.

Snieder, R., and E. Şafak (**2006**), Extracting the building response using seismic interferometry: Theory and application to the Millikan Library in Pasadena, California, *Bull. Seis. Soc. Am.*, *96*(2), 586–598, doi: 10.1785/0120050109.

Snieder, R., and E. Larose (**2013**), Extracting Earth's elastic wave response from noise measurements, *Annual Review of Earth and Planetary Sciences*, *41*(1), 183–206, doi: 10.1146/annurev-earth-050212-123936.

Snieder, R., K. Wapenaar, and K. Larner (**2006**), Spurious multiples in seismic interferometry of primaries, *Geophysics*, *71*(4), SI111–SI124, doi: 10.1190/1.2211507.

Snieder, R., K. Wapenaar, and U. Wegler (**2007**), Unified Green's function retrieval by cross-correlation; connection with energy principles, *Phys. Rev. E*, *75*, 036103, doi: 10.1103/PhysRevE.75.036103.

Snieder, R., Y. Fan, E. Slob, and K. Wapenaar (**2010**), Equipartitioning is not sufficient for Green's function extraction, *Earthq. Sci.*, *23*(5), 403–415, doi: 10.1007/s11589-010-0739-1.

Spica, Z., A. Iglesias, D. Legrand, M. Calò, M. Perton, and F. Córdoba-Montiel (**2016**), 3-D shear wave velocity model of Mexico and South US: Bridging seismic networks with ambient noise cross-correlations (C1) and correlation of coda of correlations (C3), *Geophys. J. Int.*, *206*(3), 1795–1813, doi: 10.1093/gji/ggw240.

Stehly, L., and P. Boué (**2017**), On the interpretation of the amplitude decay of noise correlations computed along a line of receivers, *Geophys. J. Int.*, *209*(1), 358, doi: 10.1093/gji/ggx021.

Stehly, L., M. Campillo, and N. M. Shapiro (**2006**), A study of the seismic noise from its long-range correlation properties, *J. Geophys. Res.: Solid Earth*, *111*(B10), doi: 10.1029/2005JB004237, b10306.

Stehly, L., M. Campillo, and N. M. Shapiro (**2007**), Traveltime measurements from noise correlation: Stability and detection of instrumental time-shifts, *Geophys. J. Int.*, *171*(1), 223–230, doi: 10.1111/j.1365-246X.2007.03492.x.

Stehly, L., M. Campillo, B. Froment, and R. L. Weaver (**2008**), Reconstructing Green's function by correlation of the coda of the correlation (C3) of ambient seismic noise, *J. Geophys. Res.: Solid Earth*, *113*(B11), doi: 10.1029/2008JB005693.

Stehly, L., B. Fry, M. Campillo, N. Shapiro, J. Guilbert, L. Boschi, and D. Giardini (**2009**), Tomography of the Alpine region from observations of seismic ambient noise, *Geophys. J. Int.*, *178*(1), 338–350, doi: 10.1111/j.1365-246X.2009.04132.x.

Stutzmann, E., F. Ardhuin, M. Schimmel, A. Mangeney, and G. Patau (**2012**), Modelling long-term seismic noise in various environments, *Geophys. J. Int.*, *191*(2), 707–722, doi: 10.1111/j.1365-246X.2012.05638.x.

Tanimoto, T. (**1990**), Modelling curved surface wave paths: Membrane surface wave synthetics, *Geophys. J. Int.*, *102*(1), 89, doi: 10.1111/j.1365-246X.1990.tb00532.x.

Tanimoto, T., and J. Um (**1999**), Cause of continuous oscillations of the Earth, *J. Geophys. Res. Solid Earth*, *104*(B12), 28723–28739, doi: 10.1029/1999JB900252.

Tanimoto, T., C. Hadziioannou, H. Igel, J. Wasserman, U. Schreiber, and A. Gebauer (**2015**), Estimate of Rayleigh-to-Love wave ratio in the secondary microseism by colocated ring laser and seismograph, *Geophys. Res. Lett.*, *42*(8), 2650–2655, doi: 10.1002/2015GL063637.

Tape, C., Q. Liu, and J. Tromp (**2007**), Finite-frequency tomography using adjoint methods - Methodology and examples using membrane surface waves., *Geophys. J. Int.*, *168*(3), 1105–1129, doi: 10.1111/j.1365-246X.2006.03191.x.

Tape, C., Q. Liu, A. Maggi, and J. Tromp (**2009**), Adjoint tomography of the southern California crust., *Science*, *325*(5943), 988–992, doi: 10.1126/science.1175298.

Tarantola, A. (**1988**), Theoretical background for the inversion of seismic waveforms, including elasticity and attenuation, *Pure Appl. Geophys.*, *128*, 365–399, doi: 10.1007/978-3-0348-7722-0_19.

Tarantola, A. (**2005**), *Inverse Problem Theory and Methods for Model Parameter Estimation*, 2nd ed., Society for Industrial and Applied Mathematics, doi: 10.1137/1.9780898717921.

Tian, Y., and M. H. Ritzwoller (**2015**), Directionality of ambient noise on the Juan de Fuca plate: Implications for source locations of the primary and secondary microseisms, *Geophys. J. Int.*, *201*(1), 429, doi: 10.1093/gji/ggv024.

Tibuleac, I. M., and D. von Seggern (**2012**), Crust-mantle boundary reflectors in Nevada from ambient seismic noise autocorrelations, *Geophys. J. Int.*, *189*(1), 493–500, doi: 10.1111/j.1365-246X.2011.05336.x.

Tikhonov, A. (**1963**), Solution of incorrectly formulated problems and the regularization method, in *Soviet Math. Dokl.*, vol. 5, pp. 1035–1038.

Traer, J., and P. Gerstoft (**2014**), A unified theory of microseisms and hum, *J. Geophys. Res.: Solid Earth*, *119*(4), 3317–3339, doi: 10.1002/2013JB010504.

Tromp, J., C. Tape, and Q. Liu (**2005**), Seismic tomography, adjoint methods, time reversal and banana-doughnut kernels, *Geophys. J. Int.*, *160*(1), 195–216, doi: 10.1111/j.1365-246X.2004.02453.x.

Tromp, J., Y. Luo, S. Hanasoge, and D. Peter (**2010**), Noise cross-correlation sensitivity kernels, *Geophys. J. Int.*, *183*(2), 791–819, doi: 10.1111/j.1365-246X.2010.04721.x.

Tsai, V. C. (**2009**), On establishing the accuracy of noise tomography traveltime measurements in a realistic medium, *Geophys. J. Int.*, *178*(3), 1555–1564, doi: 10.1111/j.1365-246X.2009.04239.x.

Tsai, V. C. (**2011**), Understanding the amplitudes of noise correlation measurements, *J. Geophys. Res.*, *116*(B9), doi: 10.1029/2011JB008483.

Valentine, A. P., and J. H. Woodhouse (**2010**), Reducing errors in seismic tomography: Combined inversion for sources and structure, *Geophys. J. Int.*, *180*(2), 847, doi: 10.1111/j.1365-246X.2009.04452.x.

van Dalen, K. N., T. D. Mikesell, E. N. Ruigrok, and K. Wapenaar (**2015**), Retrieving surface waves from ambient seismic noise using seismic interferometry by multidimensional deconvolution, *J. Geophys. Res.: Solid Earth*, *120*(2), 944–961, doi: 10.1002/2014JB011262.

van der Neut, J., J. Thorbecke, K. Mehta, E. Slob, and K. Wapenaar (**2011**), Controlled-source interferometric redatuming by crosscorrelation and multidimensional deconvolution in elastic media, *Geophysics*, *76*(4), SA63–SA76, doi: 10.1190/1.3580633.

van Driel, M., L. Krischer, S. C. Stähler, K. Hosseini, and T. Nissen-Meyer (**2015**), Instaseis: Instant global seismograms based on a broadband waveform database, *Solid Earth*, *6*(2), 701–717, doi: 10.5194/se-6-701-2015.

Vasconcelos, I., and R. Snieder (**2008**a), Interferometry by deconvolution, Part 1 – Theory for acoustic waves and numerical examples, *Geophysics*, *73*(3), S129–S141, doi: 10.1190/1.2904554.

Vasconcelos, I., and R. Snieder (**2008**b), Interferometry by deconvolution, Part 2 – Theory for elastic waves and application to drill-bit seismic imaging, *Geophysics*, *73*(3), S129–S141, doi: 10.1190/1.2904985.

Viens, L., M. A. Denolle, N. Hirata, and S. Nakagawa (**2018**), Complex near-surface rheology inferred from the response of Greater Tokyo to strong ground motions, *J. Geophys. Res.: Solid Earth*, *123*(7), 5710–5729, doi: 10.1029/2018JB015697.

Wapenaar, K. (**2004**), Retrieving the elastodynamic Green's function of an arbitrary inhomogeneous medium by cross correlation, *Phys. Rev. Lett.*, *93*, 254301, doi: 10.1103/PhysRevLett.93.254301.

Wapenaar, K., and J. Fokkema (**2006**), Green's function representations for seismic interferometry, *Geophysics*, *71*(4), S133–S146, doi: 10.1190/1.2213955.

Wapenaar, K., and J. van der Neut (**2010**), A representation for Green's function retrieval by multidimensional deconvolution, *J. Acoust. Soc. Am.*, *128*(6), EL366–EL371, doi: 10.1121/1.3509797.

Wapenaar, K., J. van der Neut, and E. Ruigrok (**2008**), Passive seismic interferometry by multidimensional deconvolution, *Geophysics*, *73*(6), A51–A56, doi: 10.1190/1.2976118.

Wapenaar, K., D. Draganov, R. Snieder, X. Campman, and A. Verdel (**2010**), Tutorial on seismic interferometry: Part 1 — Basic principles and applications, *Geophysics*, *75*(5), 195–209, doi: 10.1190/1.3457445.

Wapenaar, K., E. Ruigrok, J. van der Neut, and D. Draganov (**2011**a), Improved surface-wave retrieval from ambient seismic noise by multi-dimensional deconvolution, *Geophys. Res. Lett.*, *38*(1), doi: 10.1029/2010GL045523.

Wapenaar, K., J. van der Neut, E. Ruigrok, D. Draganov, J. Hunziker, E. Slob, J. Thorbecke, and R. Snieder (**2011**b), Seismic interferometry by crosscorrelation and by multidimensional deconvolution: A systematic comparison, *Geophys. J. Int.*, *185*(3), 1335–1364, doi: 10.1111/j.1365-246X.2011.05007.x.

Weaver, R., B. Froment, and M. Campillo (**2009**), On the correlation of non-isotropically distributed ballistic scalar diffuse waves, *J. Acoust. Soc. Am.*, *126*(4), 1817–1826, doi: 10.1121/1.3203359.

Weaver, R. L., and O. I. Lobkis (**2001**), Ultrasonics without a source: Thermal fluctuation correlations at MHz frequencies, *Phys. Rev. Lett.*, *87*, 134301, doi: 10.1103/PhysRevLett.87.134301.

Weaver, R. L., and O. I. Lobkis (**2004**), Diffuse fields in open systems and the emergence of Green's function, *J. Acoust. Soc. Am.*, *116*(5), 2731–2734, doi: 10.1121/1.1810232.

Webb, S. C. (**2007**), The Earth's 'hum' is driven by ocean waves over the continental shelves, *Nature*, *445*(7129), 754–756, doi: 10.1038/nature05536.

Weemstra, C., D. Draganov, E. N. Ruigrok, J. Hunziker, M. Gomez, and K. Wapenaar (**2017**a), Application of seismic interferometry by multidimensional deconvolution to ambient seismic noise recorded in Malargüe, Argentina, *Geophys. J. Int.*, *208*(2), 693–714, doi: 10.1093/gji/ggw425.

Weemstra, C., K. Wapenaar, and K. N. van Dalen (**2017**b), Reflecting boundary conditions for interferometry by multidimensional deconvolution, *J. Acoust. Soc. Am.*, *142*(4), 2242–2257, doi: 10.1121/1.5007833.

Wieczorek, M. A., M. Meschede, E. S. de Andrade, I. Oshchepkov, B. Xu, and A. Walker (**2017**), SHTOOLS: Version 4.2, doi: 10.5281/zenodo.592762.

Woodard, M. F. (**1997**), Implications of localized, acoustic absorption for heliotomographic analysis of sunspots, *Astrophys. J.*, *485*(2), 890–894.

Wright, M. C. M. (**2006**), Green function or green's function?, *Nature Physics*, *2*, 646, doi: 10.1038/nphys411.

Xu, Z., T. D. Mikesell, G. Gribler, and A. Mordret (**2019**), Rayleigh-wave multicomponent crosscorrelation-based source strength distribution inversion. Part 1: Theory and numerical examples, *Geophys. J. Int.*, doi: 10.1093/gji/ggz261.

Yang, Y., and M. H. Ritzwoller (**2008**), Characteristics of ambient seismic noise as a source for surface wave tomography, *Geochem. Geophys. Geosys.*, *9*(2), doi: 10.1029/2007GC001814, q02008.

Yang, Y., M. H. Ritzwoller, F.-C. Lin, M. P. Moschetti, and N. M. Shapiro (**2008**), Structure of the crust and uppermost mantle beneath the western United States revealed by ambient noise and earthquake tomography, *J. Geophys. Res. Solid Earth*, *113*(B12), doi: 10.1029/2008JB005833.

Yao, H., and R. D. van der Hilst (**2009**), Analysis of ambient noise energy distribution and phase velocity bias in ambient noise tomography, with application to SE Tibet, *Geophys. J. Int.*, *179*(2), 1113–1132, doi: 10.1111/j.1365-246X.2009.04329.x.

Zhan, Z., S. Ni, D. V. Helmberger, and R. W. Clayton (**2010**), Retrieval of Moho-reflected shear wave arrivals from ambient seismic noise, *Geophys. J. Int.*, *182*(1), 408–420, doi: 10.1111/j.1365-246X.2010.04625.x.

Zhan, Z., V. C. Tsai, and R. W. Clayton (**2013**), Spurious velocity changes caused by temporal variations in ambient noise frequency content, *Geophys. J. Int.*, *194*(3), 1574, doi: 10.1093/gji/ggt170.

Zhou, L., J. Xie, W. Shen, Y. Zheng, Y. Yang, H. Shi, and M. H. Ritzwoller (**2012**), The structure of the crust and uppermost mantle beneath South China from ambient noise and earthquake tomography, *Geophys. J. Int.*, *189*(3), 1565–1583, doi: 10.1111/j.1365-246X.2012.05423.x.

Zhou, Y., F. A. Dahlen, and G. Nolet (**2004**), Three-dimensional sensitivity kernels for surface wave observables, *Geophys. J. Int.*, *158*(1), 142–168, doi: 10.1111/j.1365-246X.2004.02324.x.

Ziane, D., and C. Hadziioannou (**2019**), The contribution of multiple scattering to Love wave generation in the secondary microseism, *Geophys. J. Int.*, doi: 10.1093/gji/ggz056.

Acknowledgments

This part of the thesis is usually read the most, but the least time is spent on writing it. There are a lot of people who contributed to my thesis and to my PhD life. I will give my best to list and thank you all, but please forgive me if I forgot to mention you.

Andreas for your never-ending support, generosity and scientific guidance. I consider myself very fortunate that I could join your group at an early stage and to be part of its evolution. The spirit and the dynamics have always been remarkable, which made it to the most interesting place to study seismology. We also got to know each other quite well and I hope you can look past my recurring lack of sunshine ;)
Christian for being Christian. I have no idea what this thesis would look like without you. You had an immense imprint on my work, shaped it at the most crucial points and you made so many things possible. Thank you for taking everyone to a higher level. And more importantly, you care a lot for everyone's well-being and try to help wherever possible. I'm looking forward to all the hiking trips to come.
Laura, my fellow sufferer in the project of ambient noise inversion, for countless discussions both scientifically and non-scientifically, brainstorming sessions and your support. Without you on the project, it would have been a lot harder to have the endurance necessary for the project and for dealing with persistent prepossessions. I hope we can push the project further in the future.
The Salvus team, Mike, Christian, Martin and Lion, for implementing various specific features and dealing at times with the weird MPI configuration on my laptop. I honestly don't know, how chapters 4 to 6 would have been possible without you and Salvus. Your collaboration and work ethic are impressive and inspired me quite often to try harder.
Victor Tsai and Laurent Stehly for hosting me at Caltech and ISTerre, respectively. Our discussions helped me a lot to get a new perspective on various aspects of the project and on science in general. I drew a lot of motivation and inspiration from my time abroad.

My house and office mate and personal trainer Lion for all the good times and laughs, work-outs, scientific discussions, and for never getting tired of pointing out how to improve a figure (figure 5.2 is for you). At times, you've been the person I've seen the most for days. I don't know many people with whom that would be possible and so much fun.
Naiara for countless coffee breaks and discussions, support in difficult times, opening up new perspectives, and your spirit to help and change things that don't go well.
Saulė for sharing the same path for such a long time. We took nonverbal communication

to a new level and you always reminded me of what is important in life. Since you left Zurich, it's also time for me and I hope that our paths will cross again soon.
My spiritual guide and mentor Friedemann for being a really good friend and for making sure that we have lunch on time and choose the best option.
My friend and scientific mentor Benjamin for inspiration, discussions, your advice and for always reminding me of the physics of the problem.
My house mate Fabian M. for bearing up with me for the whole time I've been living in Zurich and for making sure that my head also spins around other things than work.

My fellow and former group and office mates for all the discussions, ideas, coffee breaks and good times here and abroad: Alexey, Christian, Cyrill, Daniel, Dirk-Philip, Evan, Fang, Iris, Lars, Laura, Lion, Ludwig, Maria, Marie, Max, Mike, Naiara, Neda, Patrick, Paula, Percy, Robert, Sabine, Saulė, Sölvi and Václav.
My friends at ETH who made my everyday life, not just at the university, a lot more enjoyable: Anne+, Alan, Ben, Friedemann, Irene, Julia, Moritz and Uli.
My friends on Hönggerberg Lukas and Fabian L. for the good times in Zurich and at conferences, for drinks and burgers, various sport activities and, of course, for the helicopter ride. Chopper talk!
I spare you all with details and anecdotes and I will express my gratitude and appreciation in person.

Last, but definitely not least, my family and Johanna for all the love and support over years.